

## DISSERTATION

# SURFACE SCIENCE INVESTIGATIONS ON SINGLE-CRYSTALLINE RUTHENATES

Ausgeführt zum Zwecke der Erlangung des akademischen Grades eines  
Doktors der technischen Wissenschaften unter der Leitung von

UNIV.PROF. DR.TECHN. ULRIKE DIEBOLD

und

AO.UNIV.PROF. DR.TECHN. MICHAEL SCHMID

INSTITUT FÜR ANGEWANDTE PHYSIK E134

eingereicht an der Technischen Universität Wien  
Fakultät für Physik

von

DIPL.-ING. DANIEL HALWIDL

e0726755

Obere Donaustraße 63/2/13

1020 Wien

Wien, Juni 2018



## **Acknowledgement**

First, I am grateful to my supervisor Ulrike Diebold for giving me the opportunity to carry out this PhD study and for setting up a research group that made work very enjoyable.

I thank Michael Schmid for all the advice given over the years. Many thanks to Bernhard Stöger who introduced me to the work with ruthenates and Martin Setvin for sharing his wisdom on atomic force microscopy. I thank our collaborators Wernfried Mayr-Schmölzer, Florian Mittendorfer and Josef Redinger for the DFT calculations that helped interpreting experimental results.

I thank my parents Maria and Martin, my sister Veronika and my girlfriend Regina for their support during my studies.

Finally, I would like to express my gratitude to the Austrian Science Fund (FWF) project F45-07 (FOXSI) and the European Research Council (ERC) Advanced Grant “OxideSurfaces” for financial support.



## Abstract

Perovskite oxides are increasingly considered as materials for applications related to the conversion of energy such as solid oxide fuel cells. The basis of these applications are electrocatalytic reactions. These include water splitting or the oxygen reduction reaction that take place at the solid-gas and/or solid-liquid interface. Therefore a detailed knowledge of the surface chemistry of perovskite oxides is highly desirable.

This thesis focuses on the surface reactivity of  $\text{Ca}_3\text{Ru}_2\text{O}_7$ , a layered-perovskite oxide of the Ruddlesden-Popper series of calcium ruthenates. Well-defined CaO-terminated (001) surfaces were prepared by cleaving single-crystals *in situ*, *i.e.*, inside an ultrahigh vacuum (UHV) surface science apparatus. The as-cleaved surface was exposed to  $\text{H}_2\text{O}$ , CO and  $\text{O}_2$  at low temperatures between 5.5 K and 120 K. Results were obtained by low temperature (4.8 K and 78 K) Scanning Tunneling Microscopy (STM) and non-contact Atomic Force Microscopy (nc-AFM), and X-ray Photoelectron Spectroscopy (XPS). CO was found to adsorb as a strongly bound Ru-COO species, which is similar to CO adsorption on the related strontium ruthenates.

Water adsorbs exclusively dissociatively on  $\text{Ca}_3\text{Ru}_2\text{O}_7(001)$  and forms different OH-overlayers until hydroxyls cover the complete surface. The OH-overlayers show a pronounced ordering related to the rotation and tilt of the  $\text{RuO}_6$  octahedra of the  $\text{Ca}_3\text{Ru}_2\text{O}_7$  structure. This and the comparison to water adsorption on the related, but more symmetric  $\text{Sr}_2\text{RuO}_4(001)$  surface show that the surface reactivity of perovskites can be tuned by engineering rotation and tilt of the octahedra that constitute the perovskite-type lattice

Molecular oxygen adsorbs as superoxo species ( $\text{O}_2^-$ ) on  $\text{Ca}_3\text{Ru}_2\text{O}_7(001)$ . The negative charge state of the molecules was measured by Kelvin Probe Force Microscopy (KPFM) and XPS. A full monolayer of  $\text{O}_2^-$  is formed when the surface is exposed to higher doses of  $\text{O}_2$ . In contrast to other oxides, no dopants, defects, or low-coordinated sites are necessary to facilitate the activation of  $\text{O}_2$  on  $\text{Ca}_3\text{Ru}_2\text{O}_7(001)$ .

Unexpectedly, unusual thin lines in tunneling current images and random telegraph noise signals were observed on the as-cleaved and  $\text{O}_2^-$ -covered surface, respectively. These intriguing electronic effects are tentatively attributed to the highly correlated and exotic electronic structure of  $\text{Ca}_3\text{Ru}_2\text{O}_7$ .



## Kurzfassung

Oxide mit Perowskit-Struktur werden zunehmend als Materialien für Anwendungen im Bereich der Energieumwandlung wie Festoxidbrennstoffzellen in Betracht gezogen. Die Grundlage dieser Anwendungen sind elektrokatalytische Reaktionen. Diese umfassen die Wasserspaltung oder die Sauerstoffreduktionsreaktion, die an der Grenzfläche Festkörper-Gas und/oder Festkörper-Flüssigkeit ablaufen. Eine detaillierte Kenntnis der Oberflächenchemie dieser Oxide ist daher sehr wünschenswert.

Diese Arbeit konzentriert sich auf die Oberflächenreaktivität von  $\text{Ca}_3\text{Ru}_2\text{O}_7$ , einem geschichteten Perowskitoxid aus der Ruddlesden-Popper-Reihe der Kalziumruthenate. Geordnete CaO-terminierte (001) Oberflächen wurden durch Spalten von Einkristallen *in situ*, d.h. in einer Ultrahochvakuum-Oberflächenuntersuchungskammer, hergestellt. Die gespaltene Oberfläche wurde  $\text{H}_2\text{O}$ , CO und  $\text{O}_2$  bei Temperaturen zwischen 5.5 K und 120 K ausgesetzt. Die Messungen erfolgten mittels Rastertunnelmikroskopie und Rasterkraftmikroskopie bei tiefen Temperaturen (4.8 K und 78 K), sowie Röntgenphotoelektronenspektroskopie. Es zeigte sich, dass CO als eine stark gebundene Ru-COO-Spezies adsorbiert, ähnlich zur CO-Adsorption auf den verwandten Strontiumruthenaten.

Wasser adsorbiert ausschließlich dissoziativ auf  $\text{Ca}_3\text{Ru}_2\text{O}_7(001)$  und bildet unterschiedliche OH-Überstrukturen, bis Hydroxyle die gesamte Oberfläche bedecken. Die OH-Überstrukturen zeigen eine ausgeprägte Ordnung, die durch die Rotation und Neigung der  $\text{RuO}_6$  Oktaeder der  $\text{Ca}_3\text{Ru}_2\text{O}_7$  Struktur hervorgerufen wird. Dies und der Vergleich mit Wasseradsorption auf der symmetrischeren  $\text{Sr}_2\text{RuO}_4(001)$  Oberfläche zeigen, dass die Oberflächenreaktivität von Perowskiten durch gezielte Rotation und Neigung der Oktaeder, die das Perowskitgitter bilden, beeinflusst werden kann.

Molekularer Sauerstoff adsorbiert als Superoxo-Spezies ( $\text{O}_2^-$ ) auf  $\text{Ca}_3\text{Ru}_2\text{O}_7(001)$ . Der negative Ladungszustand der Moleküle wurde durch Kelvinsondenkraftmikroskopie und Röntgenphotoelektronenspektroskopie verifiziert. Eine vollständige  $\text{O}_2^-$ -Monolage bildet sich, wenn die Oberfläche höheren Dosen von  $\text{O}_2$  ausgesetzt wird. Im Gegensatz zu anderen Oxiden sind keine Dotierung mit Fremdatomen, Defekte oder Plätze mit niedriger Koordinationszahl für die Aktivierung von  $\text{O}_2$  auf  $\text{Ca}_3\text{Ru}_2\text{O}_7(001)$  notwendig.

Unerwarteterweise wurden ungewöhnliche, dünne Linien in Tunnelstrombildern und „Random Telegraph Noise“-Signale auf der sauberen und der  $\text{O}_2^-$ -bedeckten Oberfläche beobachtet. Diese faszinierenden elektronischen Effekte werden vorläufig der hochkorrelierten und exotischen elektronischen Struktur von  $\text{Ca}_3\text{Ru}_2\text{O}_7$  zugeschrieben.





# Contents

<b>1</b>	<b>Introduction</b>	<b>1</b>
1.1	Perovskite oxides	2
1.2	$\text{Ca}_3\text{Ru}_2\text{O}_7$	4
1.2.1	Ti-doped $\text{Ca}_3\text{Ru}_2\text{O}_7$	7
1.3	The CaO(001) Surface	8
<b>2</b>	<b>Experimental Setup and Methods</b>	<b>11</b>
2.1	Ultra-high Vacuum Systems	11
2.1.1	Low-temperature STM	11
2.1.2	QPlus	12
2.1.3	Machine for Reactivity Studies	13
2.2	Sample Preparation	13
2.2.1	Crystal growth	13
2.2.2	Gluing and cleaving procedure	14
2.3	Scanning Tunneling Microscopy	15
2.3.1	Tersoff-Hamann Model	16
2.4	Non-contact Atomic Force Microscopy	17
2.4.1	Frequency modulation detection	19
2.4.2	Kelvin Probe Force Microscopy	20
2.5	X-ray Photoelectron Spectroscopy	21
2.6	Density Functional Theory	22
<b>3</b>	<b>The Cleaved Surface of <math>\text{Ca}_3\text{Ru}_2\text{O}_7</math></b>	<b>23</b>
3.1	The CaO-terminated surface	23
3.1.1	Point defects	25
3.1.2	Line and area defects	27
3.2	Unsuccessful cleaving	28

---

3.3	Summary . . . . .	29
<b>4</b>	<b>H<sub>2</sub>O Adsorption on Ca<sub>3</sub>Ru<sub>2</sub>O<sub>7</sub></b>	<b>31</b>
4.1	Introduction . . . . .	31
4.2	Results . . . . .	32
4.2.1	The monomer and the low-coverage overlayer . . . . .	32
4.2.2	The high-coverage overlayers . . . . .	37
4.2.3	X-ray photoelectron spectroscopy . . . . .	42
4.2.4	Oxygen vacancies . . . . .	43
4.3	Discussion . . . . .	45
4.4	Summary . . . . .	49
<b>5</b>	<b>H<sub>2</sub>O Adsorption on Sr<sub>2</sub>RuO<sub>4</sub></b>	<b>51</b>
5.1	Introduction . . . . .	51
5.2	Results . . . . .	53
5.2.1	Activation energy measurement of the (OH) <sub>ads</sub> hopping . . . . .	53
5.2.2	Water dimer . . . . .	57
5.2.3	Higher coverage and XPS . . . . .	58
5.3	Discussion . . . . .	59
5.4	Summary . . . . .	61
<b>6</b>	<b>CO Adsorption on Ca<sub>3</sub>Ru<sub>2</sub>O<sub>7</sub></b>	<b>63</b>
6.1	Introduction . . . . .	63
6.2	Results . . . . .	63
6.2.1	Initial adsorption . . . . .	63
6.2.2	Chemisorption . . . . .	65
6.2.3	DFT . . . . .	67
6.3	Discussion . . . . .	68
6.4	Summary . . . . .	69
<b>7</b>	<b>O<sub>2</sub> Adsorption on Ca<sub>3</sub>Ru<sub>2</sub>O<sub>7</sub></b>	<b>71</b>
7.1	Introduction . . . . .	71
7.2	Results . . . . .	72
7.2.1	Low coverage . . . . .	72
7.2.2	High coverage . . . . .	75

7.2.3	Kelvin probe force microscopy . . . . .	79
7.2.4	X-ray photoelectron spectroscopy . . . . .	80
7.2.5	Charge transfer . . . . .	82
7.3	Discussion . . . . .	83
7.4	Summary . . . . .	86
<b>8</b>	<b>Electronic Effects on <math>\text{Ca}_3\text{Ru}_2\text{O}_7</math></b>	<b>87</b>
8.1	Introduction . . . . .	87
8.2	Results . . . . .	87
8.2.1	Thin lines . . . . .	87
8.2.2	Random telegraph noise . . . . .	93
8.3	Discussion . . . . .	97
8.4	Summary . . . . .	99
<b>9</b>	<b>Conclusion</b>	<b>101</b>
	<b>Appendix</b>	<b>103</b>
<b>A</b>	<b>Supplement</b>	<b>103</b>
A.1	Supplementary Figures . . . . .	103
A.2	Supplementary Tables . . . . .	108
A.3	Electronic Supplement . . . . .	110
<b>B</b>	<b>List of all STM/AFM files</b>	<b>111</b>
	<b>List of Figures</b>	<b>114</b>
	<b>List of Tables</b>	<b>116</b>
	<b>References</b>	<b>119</b>



# Chapter 1

## Introduction

Perovskite oxides, ternary compounds with the general formula  $ABO_3$  (where A stands for an alkali, alkaline-earth, or rare-earth metal, while B refers to a transition metal), and variations of this structure, such as double perovskites,  $A'A''B_2O_{5+\delta}$  or the Ruddlesden-Popper series  $A_{n+1}B_nO_{3n+1}$  show a fascinating variety of physical and chemical properties that render them interesting for both fundamental and applied research.<sup>1,2</sup> Ferroelectricity, ferromagnetism, superconductivity, large thermal conductivity and metal-insulator transition are just a selection of their interesting fundamental-physics properties. On the applied side, perovskite oxides are of interest for a wide variety of energy-conversion devices: they are used as air electrode in solid oxide fuel cells<sup>2-5</sup> and solid oxide electrolysis cells;<sup>6</sup> as catalysts in solar and thermochemical  $H_2$  and CO production, and in air batteries.<sup>7,8</sup> The basis of these applications are electrocatalytic reactions such as water splitting<sup>9</sup> or the oxygen reduction reaction (ORR)<sup>8</sup> that take place at the solid-gas and/or solid-liquid interface. Specifically, molecular oxygen in its triplet ground state is an inert species and requires activation to undergo catalytic reactions or dissociation into atomic oxygen.<sup>10</sup> The  $O_2$  activation is a crucial step in the ORR<sup>11</sup> that is potentially a major rate limiting factor for applications.<sup>12</sup> Therefore detailed knowledge of how molecules such as  $O_2$ , water or CO interact with perovskite oxide surfaces is highly desirable; the molecules are either directly part of the desired chemical reactions or present in the ambient atmosphere. A microscopic understanding of the surface chemistry is therefore sorely needed for progress in this area.

Surface science investigations on well-defined single-crystal surfaces can deliver insights on the surface reactivity of perovskite oxides at the atomic level. This was shown for the strontium ruthenates,  $Sr_2RuO_4$  and  $Sr_3Ru_2O_7$ , in the thesis of Bernhard

Stöger.<sup>13</sup> The SrO-terminated (001) surface was found to be highly reactive towards CO, H<sub>2</sub>O and CO<sub>2</sub>. The main objective of the present thesis was to investigate the surface reactivity of the related calcium ruthenate Ca<sub>3</sub>Ru<sub>2</sub>O<sub>7</sub>. One of the differences between strontium and calcium ruthenate lies in their structure: the RuO<sub>6</sub> octahedra in Ca<sub>3</sub>Ru<sub>2</sub>O<sub>7</sub> are tilted with respect to the *c*-axis while they are not in the strontium ruthenates. This is relevant as the rotation and tilting of the BO<sub>6</sub> octahedra in perovskites have been shown to influence ferroelectricity, magnetism and electronic structure.<sup>14–17</sup> There are indications that this concept influences the structure/property relationship in solid-state chemistry as well - for example in the context of fuel cell materials, octahedral tilting and distortion was found to facilitate inter-octahedral proton transfer<sup>18</sup> and O diffusion,<sup>19</sup> respectively, in the bulk. As motion of the octahedra renders inter-atomic distances inequivalent, this should result in different adsorption geometries and strengths of adsorbed molecules, and thus also be a decisive factor in surface chemistry.

## 1.1 Perovskite oxides

The ideal perovskite<sup>i</sup> oxide structure consists of a cube with the A ions at the corners, the B ion in the center and the O ions on the faces of the cube, see Figure 1.1. The A ion is typically an alkaline earth or rare earth element and the B ion is a transition metal. The perovskite structure was first described by V. M. Goldschmidt<sup>21</sup> in 1926, who recognized that the radius of the ions is fundamental to the formed structure. The so-called tolerance factor

$$t = \frac{r_A + r_O}{\sqrt{2}(r_B + r_O)} \quad (1.1)$$

lies between 0.8 and 1.0 for the perovskite structure; when *t* becomes smaller or larger, different structures are formed. Goldschmidt noted that elements can be partially or fully substituted by a different element as long as the resulting ionic radius and polarizability are not too different to the original ion; this makes the synthesis of an almost unlimited number of chemical compositions and tuning of the physical and chemical properties by doping possible.

---

<sup>i</sup>Perovskite is the name for the structural family as well as for the particular mineral CaTiO<sub>3</sub>.<sup>20</sup>

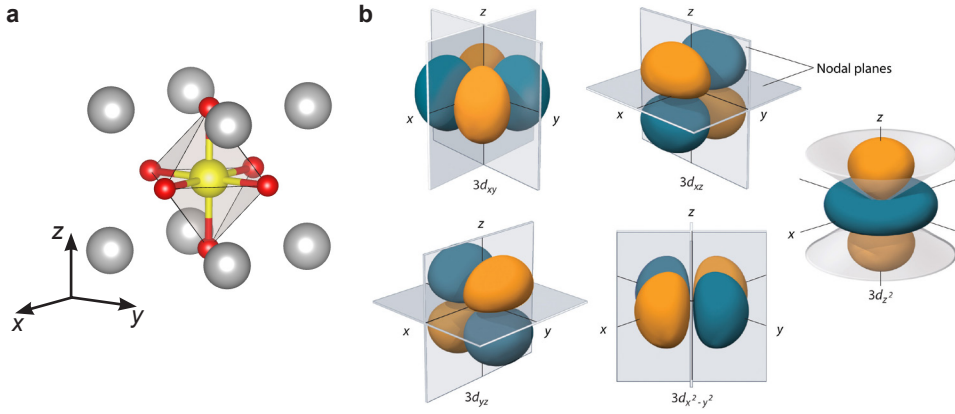


**Figure 1.1 | The ideal perovskite oxide structure and the d orbitals.** a) The B cation is octahedrally coordinated to six O anions. A cations – grey, B cations – yellow, O anions – red. b) Orientation and shape of the 3d orbitals. (4d orbitals are larger and similar in shape.) Reprinted from [22] under the Creative Commons Attribution-Noncommercial-Share Alike 3.0 United States License.

## Electron configuration and the Hubbard model

The octahedral coordination of the transition metal ion to the six surrounding oxygen anions leads to a splitting of the d orbitals due to the crystal field potential. The  $e_g$  orbitals ( $d_{x^2-y^2}$  and  $d_{3z^2-r^2}$ ) that point toward the oxygen anions have higher energy than the  $t_{2g}$  orbitals ( $d_{xy}$ ,  $d_{yz}$  and  $d_{zx}$ ) that point between them, see Figure 1.1b.<sup>23</sup> The energy difference between  $t_{2g}$  and  $e_g$  is labeled  $\Delta_{\text{Oct}}$ . The ratio between  $\Delta_{\text{Oct}}$  and the energy penalty for putting two electrons in the same orbital (Hund's rule) determines the order of filling the  $t_{2g}$  and  $e_g$  orbitals with electrons. This determines the spin state of the transition metal ion that takes on a low-spin state for large  $\Delta_{\text{Oct}}$  and a high-spin state for small  $\Delta_{\text{Oct}}$  (*i.e.*, obeying Hund's rule). The twofold and threefold degeneracy of the  $e_g$  and  $t_{2g}$  orbitals, respectively, may be lifted by Jahn-Teller distortions, for example when the  $\text{BO}_6$  octahedra are compressed or stretched along the  $z$ -axis.<sup>24</sup>

Some transition metal oxides show metal-insulator transitions that can not be explained by a simple band-filling model of non-interacting electrons. Instead, the electron-electron correlation has to be taken into account. The simplest model is the Hubbard model with its Hamiltonian<sup>25</sup>

$$H = - \sum_{i,j,\sigma} t_{ij} c_{i\sigma}^\dagger c_{j\sigma} + U \sum_i n_{i\uparrow} n_{i\downarrow}, \quad (1.2)$$

where  $c_{i\sigma}^{(\dagger)}$  annihilates (creates) an electron at site  $i$  with spin  $\sigma$ ; the first term describes the hopping of an electron from site  $i$  to  $j$  with the hopping amplitude  $t_{ij}$ ; the second term describes the Coulomb repulsion between electrons that occupy the same orbital at site  $i$ . The hopping amplitude (*i.e.*, the bandwidth  $W$ ) depends on the orbital overlap between sites  $i$  and  $j$ . When  $U$  is sufficiently greater than  $W$ , the band splits into a lower and upper band (relative to the Fermi energy) with a charge gap in between, which is the description for the so-called Mott-Hubbard insulator.

In case of perovskite oxides, the overlap of two d orbitals on two adjacent transition metal ions is determined by indirect transfer through the p orbitals of the oxygen anions.<sup>25</sup> Thus rotation/tilt and/or distortion of the  $\text{BO}_6$  octahedra may severely influence the physical properties.

### Perovskite oxide surfaces

The preparation of well defined, flat and unreconstructed perovskite oxide surfaces is challenging. Sputtering ternary compounds such as  $\text{ABO}_3$  usually leads to a stoichiometry change due to different sputter yields for different elements. For example, the  $\text{SrTiO}_3(110)$  surface prepared by  $\text{Ar}^+$  sputtering and subsequent annealing exhibits a variety of surface reconstructions the formation of which can be controlled by depositing Sr or Ti before annealing.<sup>26</sup> Surface preparation by cleaving or fracturing<sup>27</sup>  $\text{ABO}_3$  compounds is difficult due to the lack of natural cleavage planes. Moreover, bulk-terminated surfaces are usually polar resulting in compensating surface reconstructions. Atomically resolved images of surfaces of  $\text{ABO}_3$  perovskites prepared by cleaving have only recently been reported for  $\text{K}\text{TaO}_3$ <sup>28</sup> and  $\text{SrTiO}_3$ .<sup>29</sup>

In the present thesis surfaces are prepared by cleaving layered perovskites that exhibit a natural cleavage plane. The cleaving procedure requires little effort and the resulting surfaces are bulk-terminated and atomically resolvable.<sup>30</sup>

## 1.2 $\text{Ca}_3\text{Ru}_2\text{O}_7$

$\text{Ca}_3\text{Ru}_2\text{O}_7$  is a layered perovskite material and a member of the Ruddlesden-Popper series  $\text{A}_{n+1}\text{B}_n\text{O}_{3n+1}$ . The series is named after S. N. Ruddlesden and P. Popper, who reported three new compounds of  $\text{K}_2\text{NiF}_4$  type ( $\text{Sr}_2\text{TiO}_4$ ,  $\text{Ca}_2\text{MnO}_4$ ,  $\text{SrLaAlO}_4$ ) in 1957;<sup>31</sup> numerous compounds have been found or predicted since then.<sup>32</sup> The layered structure of the Ruddlesden-Popper perovskites is shown in Figure 1.2. Depending



on the series index  $n$ , the Ruddlesden-Popper materials consists of stacks of  $n$  layers of the perovskite structure (ABO<sub>3</sub>) along [001], separated by double AO-layers. The perovskite stacks are shifted by half a lattice constant in [100] and [010] direction across the double AO-layer. The BO<sub>6</sub> octahedra are not necessarily oriented and aligned to each other as shown in Figure 1.2, but can be rotated/tilted and/or distorted.

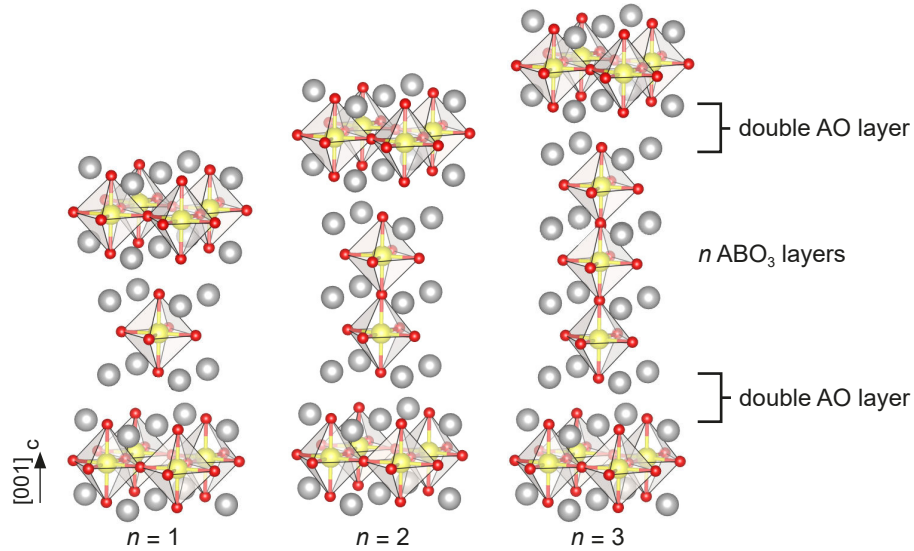


**Figure 1.2 | The layered structure of Ruddlesden-Popper compounds.** Stacks of  $n$  layers of the perovskite structure (ABO<sub>3</sub>) along [001] are separated by double AO-layers.

Ca<sub>3</sub>Ru<sub>2</sub>O<sub>7</sub> is the  $n = 2$  member of the Ruddlesden-Popper series Ca <sub>$n+1$</sub> Ru <sub>$n$</sub> O <sub>$3n+1$</sub>  and therefore consists of two perovskite-like CaRuO<sub>3</sub> layers (also referred to as *bilayer* in the following) separated by double CaO layers along the [001] direction, see Figure 1.3. The lattice constants of the orthorhombic unit cell at 60 K are  $a = 5.363 \text{ \AA}$ ,  $b = 5.531 \text{ \AA}$ ,  $c = 19.541 \text{ \AA}$ .<sup>33</sup> The  $a$ ,  $b$  and  $c$  axes correspond to the [100], [010] and [001] directions, respectively. The RuO<sub>6</sub> octahedra are tilted and alternately rotated in the  $ab$ -plane. Between 8 K and 292 K the Ru-O-Ru bond angle along the  $c$ -axis varies between 152° and 153°; this translates into a tilt of approximately 13.8° with respect to the  $c$ -axis that is primarily projected onto the  $ac$ -plane.<sup>34</sup> Within the  $ab$ -plane the Ru-O-Ru bond angle is approximately 150°. Additionally to the described tilt and rotation, the individual RuO<sub>6</sub> octahedra is slightly distorted; the O-Ru-O bond angle along the  $c$ -axis is 177°, but only slightly smaller than 180° in the  $ab$ -plane; the six Ru-O bond lengths are all different and vary by up to 1.3%.<sup>34</sup>

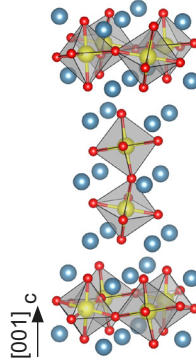


**Figure 1.3 | The structure of  $\text{Ca}_3\text{Ru}_2\text{O}_7$ .** Ca – blue, Ru – yellow, O – red. The  $\text{RuO}_6$  octahedra are alternately tilted with respect to the  $c$  axis and rotated in the  $ab$  plane.

The tetravalent  $\text{Ru}^{4+}$  ion has four electrons in the  $4d$  shell ( $4d^4$ ). Due to the crystal field splitting the electrons occupy only the  $t_{2g}$  orbitals, where one orbital is doubly occupied and two orbitals are singly occupied.<sup>35</sup> Therefore the  $\text{Ru}^{4+}$  is in a  $S = 1$  spin state, as has been confirmed by magnetization measurements.<sup>36</sup>

$\text{Ca}_3\text{Ru}_2\text{O}_7$  is paramagnetic at room temperature and was characterized as “bad metal” due to its unusually high metallic resistivity ( $\rho = 1.5 \text{ m}\Omega \text{ cm}$ ) and the linear dependence of resistivity on temperature for  $T > 56 \text{ K}$ .<sup>37</sup> With decreasing temperature it undergoes an antiferromagnetic transition at  $T_N = 56 \text{ K}$  (Neel temperature) and a Mott transition (metal to insulator transition) at  $T_{\text{MI}} = 48 \text{ K}$ .<sup>36</sup> In the antiferromagnetic phase below  $T_N$  the magnetic moments couple ferromagnetically within the bilayer, but the bilayers couple antiferromagnetically to each other; for  $T_{\text{MI}} < T < T_N$  the magnetic moments are aligned along the  $a$ -axis (AFM- $a$  phase); for  $T < T_{\text{MI}}$  the moments are aligned along the  $b$ -axis (AFM- $b$  phase),<sup>38</sup> see Figure 1.4.

At the Mott transition at  $T_{\text{MI}} = 48 \text{ K}$  the  $c$ -axis resistivity  $\rho_c$  increases rapidly by as much as a factor of 18.<sup>36,39</sup> The in-plane resistivity  $\rho_{ab}$  increases as well but not as dramatic as  $\rho_c$ . The results in refs. [36, 39] were obtained from single crystals grown by a flux method; results from single crystals grown by a floating zone method, which is generally expected to produce purer crystals, show that  $\rho_c$  levels off below  $10 \text{ K}$ ;<sup>40</sup> The in-plane resistivity increases between  $T_{\text{MI}}$  and  $30 \text{ K}$ , where a metallic transport appears again. The anisotropy ratio  $\rho_c/\rho_a$  is 1500 at  $0.2 \text{ K}$ , indicating a quasi-two-dimensional metallic ground state.<sup>40</sup>

The Mott transition at  $T_{\text{MI}} = 48 \text{ K}$  is accompanied by a sudden decrease of the lattice constant  $c$  by approximately  $0.1 \%$ , while both  $a$  and  $b$  lengthen by approxim-

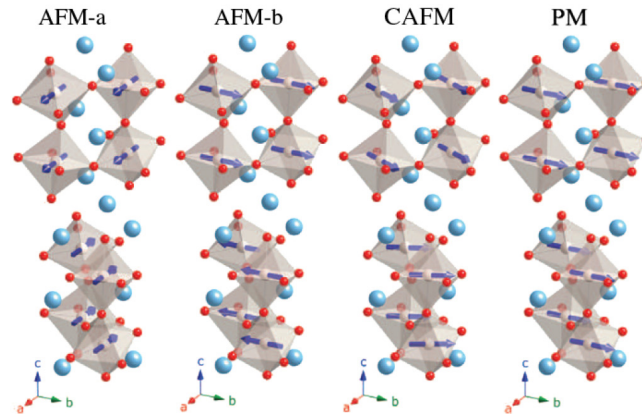


**Figure 1.4 | Magnetic phases of Ca<sub>3</sub>Ru<sub>2</sub>O<sub>7</sub>.** Ca – blue, Ru – grey, O – red. Magnetic structures in the AFM-a and AFM-b phase. In the PM phase all magnetic moments are aligned by the applied magnetic field. Reprinted figure with permission from Bao, W., Mao, Z. Q., Qu, Z. & Lynn, J. W. *Physical Review Letters* 100, 247203 (2008). Copyright (2018) by the American Physical Society.

ately 0.07%.<sup>33</sup> This compresses the RuO<sub>6</sub> octahedra along the *c*-axis and thus lowers the energy of the *d<sub>xy</sub>* orbitals relative to the *d<sub>yz</sub>* and *d<sub>zx</sub>* orbitals; therefore two electrons occupy the *d<sub>xy</sub>* orbital and one electron occupies each of the nearly degenerate *d<sub>yz</sub>* and *d<sub>zx</sub>* orbital, which is a state of orbital order.<sup>41</sup> Raman-scattering<sup>42,43</sup> and tunneling spectroscopy<sup>44</sup> experiments show the opening of a charge gap of approximately 0.1 eV, fitting to the poor conduction below *T<sub>MI</sub>*.

Band structure calculations<sup>45</sup> including spin-orbit coupling and Coulomb repulsion reproduce the observed metallic a-AFM phase between *T<sub>MI</sub>* < *T* < *T<sub>N</sub>* and the insulating b-AFM phase below *T<sub>MI</sub>*.

Moreover, Ca<sub>3</sub>Ru<sub>2</sub>O<sub>7</sub> shows a number of exotic phenomena:<sup>35</sup> unconventional colossal magnetoresistance, bulk spin valve effect, quantum oscillations and magnetoresistance oscillations. The discussion of these phenomena would go beyond the scope of this introduction, but underline the strongly correlated and exotic nature of this material.

### 1.2.1 Ti-doped Ca<sub>3</sub>Ru<sub>2</sub>O<sub>7</sub>

Substituting a small concentration of Ru with Ti substantially changes the magnetic and electronic properties of Ca<sub>3</sub>Ru<sub>2</sub>O<sub>7</sub>.<sup>46</sup> At a Ti concentration of 3% (*x* = 0.03 in Ca<sub>3</sub>(Ru<sub>1-x</sub>Ti<sub>x</sub>)<sub>2</sub>O<sub>7</sub>) the in-plane resistivity  $\rho_{ab}$  exhibits insulating behaviour below *T<sub>MI</sub>* (48 K) which is in contrast to the metallic ground state observed in the pristine

material; for higher concentrations of 5 % and 10 % the in-plane resistivity below  $T_{\text{MI}}$  increases dramatically by 8 orders of magnitude. The anisotropy ratio  $\rho_c/\rho_{ab}$  for  $x = 0.03$  increases to  $10^7$  at  $T_{\text{MI}}$  and increases further to  $10^9$  below 30 K.<sup>47</sup> The change of the lattice constants at  $T_{\text{MI}}$  is similar to  $\text{Ca}_3\text{Ru}_2\text{O}_7$  but much larger for the  $b$  and  $c$  constants.

The magnetic ground state changes from AFM-b (see previous section) to a nearest-neighbour AFM state (G-AFM)<sup>47</sup> for  $x > 0.04$ ; for concentrations between 2 and 4 % a mixture of the two states is observed.

According to calculations<sup>46,48</sup> Ti occurs as  $\text{Ti}^{4+}$  independent of magnetic order with the d bands approximately 1 to 2 eV above the Fermi energy. Further, very little contribution of Ti to the density of states at the Fermi level was found. This leads to a disruption of the hopping in the Ru-O network and thus narrows the bands and modifies the moments on the neighbouring atoms. Therefore Ti acts as a strong scatterer for the weakly coherent electronic states that are responsible for the metallic behaviour in  $\text{Ca}_3\text{Ru}_2\text{O}_7$ .

### 1.3 The CaO(001) Surface

Since the cleaving of  $\text{Ca}_3\text{Ru}_2\text{O}_7$  leads to a CaO-terminated surface (see Chapter 3), the reactivity of the binary alkaline-earth CaO(001) surface towards selected molecules is briefly summarized. CaO crystallizes in the rock-salt structure with a lattice constant of 4.81 Å,<sup>49</sup> resulting in a Ca-Ca distance of 3.4 Å. It is electrically insulating with a band gap of 3.8 eV.<sup>50</sup>

The dissociation of water on CaO(001) was predicted by DFT with adsorption energies around 0.9 eV;<sup>51,52</sup> the lattice constant was identified as key factor for the adsorption energy and stability of the adsorption mode.<sup>51</sup> On vacuum-cleaved CaO(001) exposure to low pressures of water ( $\approx 10^{-10}$  mbar) resulted in surface hydroxyls detected by XPS;<sup>53</sup> hydroxylation of the bulk was suspected for exposure to higher pressures ( $\approx 10^{-4}$  mbar). A combined STM, Infrared Reflection Absorption Spectroscopy (IRAS) and DFT study on well-defined CaO films grown on Mo(001) found chains of mixed dissociated and molecular water for low dosages at room temperature.<sup>54</sup> At increased coverage ( $\approx 0.5$  ML) a transformation into a disordered state with partially solvated  $\text{Ca}^{2+}$  ions was reported<sup>55</sup> and predicted;<sup>56</sup> a partial hydroxylation of sub-surface layers was observed during exposure to water in the sub-millibar pressure

range.

Molecular oxygen was predicted to only weakly physisorb on pristine CaO(001).<sup>57</sup> The formation of charged (*i.e.*, chemisorbed) oxygen species was observed only after introducing defects by ultraviolet or gamma irradiation, thermal activation, or doping with transition metal ions.<sup>58</sup> A combined STM and DFT study on CaO films showed that Mo dopants enable the chemisorption of O<sub>2</sub>; the Mo ion donates charge that is transferred to the adsorbate, resulting in the formation of O<sub>2</sub><sup>-</sup>.<sup>59</sup>

The adsorption of CO<sub>2</sub> on CaO films at room temperature was investigated by DFT and IRAS.<sup>60</sup> CO<sub>2</sub> adsorbs as a monodentate surface carbonate species where the C binds to a surface oxygen ion (O<sub>surf</sub>); the oxygens of the CO<sub>2</sub> point towards Ca ions adjacent to the O<sub>surf</sub>.

A thorough search of the literature yielded no study of CO adsorption on a well-defined single-crystalline CaO(001) surface. On a polycrystalline CaO film grown on Si(100) the formation of a carbonate species was observed by UPS and Metastable Impact Electron Spectroscopy (MIES) at room temperature.<sup>61</sup> However, the film was contaminated by OH groups and relatively large amounts of CO (> 5 L) were dosed; the underlying mechanism of the carbonate formation could not be explained.



# Chapter 2

## Experimental Setup and Methods

### 2.1 Ultra-high Vacuum Systems

#### 2.1.1 Low-temperature STM

The *LT-STM* is an ultra-high vacuum (UHV) system that consists of an analysis chamber, a preparation chamber, and a load lock. The analysis chamber is equipped with a commercial Omicron low-temperature STM (LT-STM), which can be operated at 6 K, 78 K or room temperature. The analysis chamber is pumped with an ion pump and a titanium sublimation pump to achieve a base pressure of  $5 \times 10^{-12}$  mbar. The preparation chamber is equipped with a raster sputter gun (SPECS<sup>TM</sup> IQE 12/38) and a heating stage that can be used for preparing samples (not used for the samples in this work - see below) and STM tips. In addition, samples can be bombarded with electrons and irradiated by photons using a raster electron gun (SPECS<sup>TM</sup> EQ22/35) and an X-ray source (SPECS<sup>TM</sup> XR50), respectively. A hemispherical electron energy analyzer (SPECS<sup>TM</sup> Phoibos 100) is available for Auger Electron Spectroscopy, X-ray Photoelectron Spectroscopy (XPS) and Ion Scattering Spectroscopy. The surface properties can also be investigated with Low Energy Electron Diffraction (LEED). The preparation chamber is pumped with an ion pump, a titanium sublimation pump and a turbomolecular pump. Usually, the gate valve between the preparation chamber and the turbomolecular pump is closed to lower the pressure of the preparation chamber from  $2 \times 10^{-10}$  mbar to a base pressure of  $5 \times 10^{-11}$  mbar. The composition of the residual gas can be checked with a mass spectrometer (BALZERS QMG 125). A manipulator is used to transfer samples between preparation and analysis chamber.

The load lock is separated from the preparation chamber by a manually operated

gate valve. Before transferring new samples or tips to the preparation chamber, the load lock has to be baked for at least 5 hours and cooled down for 2 hours to preserve low pressure in the preparation chamber during the transfer. A magnetically coupled manipulator with linear and rotary motion is used for transfer between load lock and preparation chamber. For the bake-out the magnet of the manipulator has to be either removed or a bakeable magnet used in the first place. The latter is recommended for samples sensitive to vibration or shock as replacing the magnet after the bake-out occasionally causes the manipulator to jolt (most probably caused by an initial misalignment of the magnets outside and inside the manipulator). That jolt can lead to unintentional cleaving of the samples that were used in this work (see below) in the load lock.

The chambers are equipped with several leak valves to dose controlled amounts of CO, CO<sub>2</sub>, H<sub>2</sub>O and O<sub>2</sub>. For adsorbing gases that do not stick at room temperature the manipulator can be cooled down to 100 K by flowing cooled, gaseous N<sub>2</sub> through it. The temperature of the manipulator can be stabilized between 100 K and room temperature by counter-heating. Dosing gases directly into the STM head is possible after rotating the cryostat doors to the proper position.

### 2.1.2 QPlus

Combined low-temperature STM and non-contact Atomic Force Microscopy (nc-AFM) measurements were performed at 4.8 K and 78 K in the *QPlus* system, an UHV system consisting of a preparation chamber, an analysis chamber and a load lock. The chambers are pumped by ion pumps achieving base pressures below  $2 \times 10^{-11}$  mbar. O<sub>2</sub> was either dosed directly into the cryostat in the analysis chamber at 5.5 K or in the preparation chamber while keeping the sample at 123 K.

The analysis chamber is equipped with a commercial Omicron q-Plus LT head. Tuning fork-based AFM sensors with a separate wire for the tunnelling current were used.<sup>62,63</sup> Typical parameters of the sensors were  $k = 1900$  N/m,  $f_0 = 31\,500$  Hz, and  $Q \approx 30,000$ . Electrochemically etched W-tips were glued to the tuning fork and cleaned *in situ* by field emission and self-sputtering in  $10^{-6}$  mbar Ar.<sup>64</sup> The sensor oscillation is excited by adding an ac voltage to the *z*-piezo voltage. The frequency shift is detected by a phase locked loop (PLL).

All nc-AFM images in this thesis show the frequency shift  $\Delta f$  and were recorded



in constant-height mode, where darker color means higher attractive force.

### 2.1.3 Machine for Reactivity Studies

The *Machine for Reactivity Studies* (MRS) is an UHV system that provides analysis techniques such as Low Energy Electron Diffraction, Low Energy Ion Scattering, Temperature Programmed Desorption, Ultraviolet Photoelectron Spectroscopy and XPS to investigate adsorption and surface chemistry at oxide surfaces.<sup>65</sup> Sample temperatures between 30 K and 1200 K can be reached by a continuous-flow liquid-He cryostat and resistive heating of the sample holder. The chamber is pumped by a turbomolecular pump and the cryostat, which acts as a cryogenic pump when cooled, resulting in a base pressure of  $1.0 \times 10^{-10}$  mbar or lower.

For XPS measurements of H<sub>2</sub>O on Sr<sub>2</sub>RuO<sub>4</sub> a monochromatic Al K $\alpha$  X-ray source and a hemispherical electron analyzer (SPECS<sup>TM</sup> Phoibos 150) at normal emission with a pass energy of 16 eV were used. The samples were mounted on Ta plates that were screwed to the sides of the half circle-shaped and gold-plated chromium copper pieces at the end of the cryostat using the screws of the heating wires. De-ionized water (Millipore water, purified in-house) was further cleaned by several freeze-pump-thaw cycles and was dosed to the chamber while keeping the sample at 140 K.

## 2.2 Sample Preparation

### 2.2.1 Crystal growth

All calcium and strontium ruthenate samples that were investigated in this thesis were grown by our collaborator Prof. Zhiqiang Mao and his students at Tulane University, New Orleans, LA. A two-mirror optical floating-zone furnace was used to grow high-quality perovskite single crystals. The technique is explained in detail for the growth of Sr<sub>2</sub>RuO<sub>4</sub> in ref. [66], a summary is available in ref. [13]. The starting material for the growth of Ca<sub>3</sub>Ru<sub>2</sub>O<sub>7</sub> has a 55 to 60 % excess of Ru; except for the growth speed and gap speed the parameters are similar to the growth of Sr<sub>2</sub>RuO<sub>4</sub>.

## 2.2.2 Gluing and cleaving procedure

The strontium and calcium ruthenates investigated in the present thesis cleave easily along the (001) plane within the AO double layer, see Section 1.2. The following description applies to both strontium and calcium ruthenate. The as-grown crystal rod was broken into smaller pieces of varying size by use of pliers and tweezers; the pieces usually exhibit two parallel, shiny and flat surfaces that are easily identified as the (001) surfaces. The lateral size (in [100] and [010] direction) is typically a few mm; the height (in [001] direction) is typically from a few tenths of a millimeter to 2 mm.

One of the (001) surfaces of the sample is glued to a stainless sample plate; a small stainless steel stub is glued to the other side that is then later used as handle to cleave the sample in UHV, see Figure 2.1. Between sample and sample plate an electrically conducting, silver-containing epoxy glue is used (EPO-TEK H21D); between sample and stub a non-conducting epoxy glue is used (EPO-TEK H77). The assembly of sample plate, sample and stub is annealed at 150 °C for 1.5 h to harden the epoxy glue. A detailed description of the gluing procedure and the used gluing gadget is available in ref. [13]. Another gadget was built for gluing samples on Prevac sample holders.

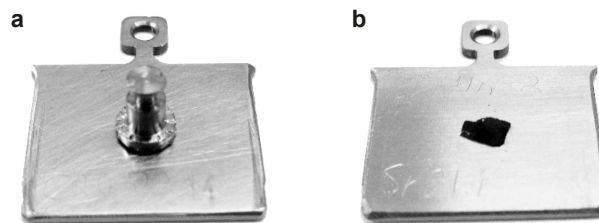


**Figure 2.1 | The sample assembly.** a) Sample plate, sample (under the stub, not visible), stub. b) The cleaved sample. The sample plate is 1.8 cm in width.

The samples were cleaved in UHV at temperatures between 100 to 120 K by applying lateral force to the stub. In the LT-STM and the QPlus system the sample was facing downward and gentle force was applied by a wobble stick until the sample cleaved. In the MRS the samples were mounted sideways so that the stub (and the [001] direction of the sample) was horizontal; lateral force was applied by a stainless steel tube mounted on a manual linear motion mechanism.

In total roughly 55  $\text{Ca}_3\text{Ru}_2\text{O}_7$  samples from three sample batches were cleaved over the course of this thesis. See Chapter 3 for a comment on unsuccessful cleaving

of samples.

## 2.3 Scanning Tunneling Microscopy

Scanning tunneling microscopy (STM) was introduced by Gerd Binnig and Heinrich Rohrer<sup>67</sup> in 1982 as an advancement of the then classical tunneling technique of using metal-insulator-metal sandwich structures with a solid-state insulator as tunneling barrier. By using a sharp metal tip as scanning electrode and vacuum as the tunneling barrier, STM provided unprecedented spatial resolution of the surface as well as access to the surface after the tunneling experiment for further treatment or other investigations techniques.

The basic experimental setup is shown in Figure 2.2. A bias voltage in the range from a few mV to several V is applied between the sample and a sharp metallic tip. Using a piezo drive, the tip approaches the sample to a typical distance of a few Å at which a tunneling current flows. The tip is mounted on a piezoelectric tube that allows rastering the tip across the surface. In constant-current mode the tunneling current is held constant by the STM control unit by adjusting the tip-sample distance accordingly; the distance is recorded as topographic image of the surface. In constant-height mode the tip-sample distance is not adjusted and the varying tunneling current is recorded as image.

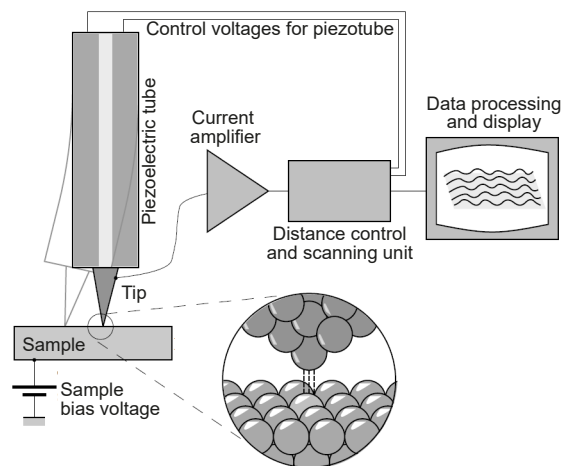


**Figure 2.2 | The concept of Scanning Tunneling Microscopy.** Schematic of the experimental setup of STM. Adapted and reprinted with kind permission from Michael Schmid.

A simple model for the tunneling current is the time-independent, 1-dimensional

Schrödinger equation

$$\left(-\frac{\hbar^2}{2m}\nabla^2 + V\right)\psi(z) = E\psi(z), \quad (2.1)$$

where the potential  $V$  between tip and sample is assumed to be a rectangular barrier of height  $\phi$  (work function).<sup>68</sup> The solution for  $\psi(z)$  inside the barrier is a decaying wave function according to

$$\psi(z) \propto \exp(-\kappa z) \quad \text{with} \quad \kappa = \sqrt{\frac{2m\phi}{\hbar^2}}. \quad (2.2)$$

The tunneling current is proportional to the transmission  $T$  that in turn is proportional to  $|\psi(z)|^2$ . For a barrier of tip-sample distance  $d$  the tunneling current is therefore

$$I \propto T \propto |\psi(d)|^2 \propto \exp(-2\kappa d). \quad (2.3)$$

The exponential dependence of the tunneling current on the tip-sample distance and typical values for  $\phi$  give a change of approximately one order of magnitude for every 1 Å change in distance; this enables  $z$ -resolution in the pm range.

### 2.3.1 Tersoff-Hamann Model

One year after the introduction of STM (see above) Jerry Tersoff and Donald R. Hamann presented a theory for tunneling between a real surface and a model probe tip, taking into account the local density of states of the surface and the tip geometry.<sup>69,70</sup> From first-order perturbation theory the tunneling current is given by

$$I = \frac{2\pi e}{\hbar} \sum_{\mu,\nu} f(E_\mu)[1 - f(E_\nu + eV)]|M_{\mu\nu}|^2\delta(E_\mu - E_\nu), \quad (2.4)$$

where  $f(E)$  is the Fermi function and  $V$  is the bias voltage;  $M_{\mu\nu}$  is the tunneling matrix element between states of the probe  $\psi_\mu$  and the surface  $\psi_\nu$  and given by<sup>71</sup>

$$|M_{\mu\nu}|^2 = \frac{\hbar^2}{2m} \int d\vec{S} (\psi_\mu^* \nabla \psi_\nu - \psi_\nu \nabla \psi_\mu^*), \quad (2.5)$$

where the integral is over any surface lying entirely within the vacuum region separating tip and sample; the quantity in parentheses is simply the current operator. To evaluate  $M_{\mu\nu}$  the surface wave function is described by 2-dimensional Bloch waves

and a  $s$  wave function for the tip is assumed.

For small bias voltages the tunneling current is proportional to the local density of states (DOS) close to the Fermi energy:

$$I \propto \int_{E_F}^{E_F+U} \rho_t(E - eU) \rho_s(E) T(E, U) dE, \quad (2.6)$$

where  $\rho_s$  and  $\rho_t$  is the DOS of sample and tip, respectively, and  $T(E, U)$  is the transmission probability. When the tunneling current is kept constant, the tip follows contours of constant local density of states. When a constant  $\rho_t$  and  $T(E, U)$  are assumed, the surface DOS at  $E + eU$  is proportional to  $dI/dU$ .

## 2.4 Non-contact Atomic Force Microscopy

The Atomic Force Microscope was proposed by G. Binnig, C. F. Quate and Ch. Gerber in 1986.<sup>72</sup> While different modes of operation are available, this section concentrates on the mode used in this thesis, nc-AFM.

### Forces between tip and sample

Non-contact atomic force microscopy (nc-AFM) relies on the force experienced by a sharp tip when brought close to a sample. The overall force between tip and sample ( $F_{ts}$ ) consists of three major components:<sup>73</sup>

$$F_{ts} = F_{el} + F_{vdW} + F_{chem}, \quad (2.7)$$

where  $F_{el}$  is electrostatic force,  $F_{vdW}$  is van der Waals force and  $F_{chem}$  is chemical interaction force.

The long-range electrostatic force is described by modelling the tip and the sample as the two plates of a capacitor, see Section 2.4.2. The van der Waals force describes the interaction between two induced dipoles and can be calculated for specific tip shapes.<sup>74</sup> When the tip-sample distance becomes small enough and a suitable atom or molecule is located at the apex of the tip (*i.e.*, the tip is functionalized), chemical bonds can be formed between the tip and sample; the resulting chemical interaction can be modelled by a Lennard-Jones<sup>75</sup> or a Morse<sup>76</sup> potential.  $F_{ts}$  is usually attractive unless the tip-sample distance is decreased below the chemical bond length leading

to Pauli repulsion.

$F_{ts}$  varies with the tip-sample distance  $d$  (where  $d = 0$  at the sample surface, and  $d > 0$  for increasing tip-sample distance) and therefore the gradient of  $F_{ts}$  in  $z$ -direction (the normal to the sample surface) will be non-zero:

$$\nabla F_{ts}(z) \neq 0. \quad (2.8)$$

### Resonance frequency shift

The gradient of  $F_{ts}$  is measured by a sharp tip mounted on an oscillating cantilever (the actual implementation depends on the sensor type) that can be modelled as a perturbed harmonic oscillator. At a large enough distance from the sample so that  $F_{ts} = 0$ , the sensor is oscillating with resonance frequency  $f_0$  and amplitude  $A$ . For small perturbations by a non-constant external force with stiffness  $k_{\text{ext}}$  the resonance frequency  $f_{\text{res}}$  of an oscillator with stiffness  $k$  changes according to

$$\frac{\Delta f}{f_{\text{res}}} = \frac{1}{2k} k_{\text{ext}}. \quad (2.9)$$

The above expression is independent of  $z$  and gives a constant  $\Delta f$  since the stiffness does not vary with  $z$ . However, in a physical system the gradient of  $F_{ts}$  varies with  $z$  and the general expression for the  $z$ -dependent frequency shift becomes (see [73, p. 200])

$$\Delta f(z) = -\frac{f_0}{\pi k A} \int_{-1}^1 F_{ts}(z + A(1 + u)) \left( \frac{u}{\sqrt{1 - u^2}} \right) du. \quad (2.10)$$

From this equation an approximation for  $F_{ts}(z)$  can be derived.<sup>77</sup>

### Q factor

A characteristic quantity of an AFM sensor is the quality factor  $Q$ ; it is defined as the ratio between the resonance frequency and the full width half maximum of the resonance peak:

$$Q = \frac{f_0}{\Delta f_{\text{FWHM}}}. \quad (2.11)$$

Another definition for  $Q$  is the ratio of energy stored in the oscillator to energy dissipated per cycle/ $2\pi$  by damping. In practical terms, this means the higher the  $Q$  the sharper the resonance peak and the more underdamped the oscillator.

### 2.4.1 Frequency modulation detection

In frequency modulation (FM) detection a constant oscillation amplitude  $A$  is maintained when the resonance frequency of the sensor changes due to  $\nabla F_{ts}(z)$ ; the frequency change is detected in the deflection signal of the sensor and the driving output is continuously adjusted to maintain the oscillation with  $A$  at the new resonance frequency. The FM approach was introduced by Albrecht *et al.*<sup>78</sup> who showed the advantages of the FM detection that are high sensitivity (high  $Q$ ) without placing restrictions on bandwidth.<sup>i</sup>

In topographic mode the detected  $\Delta f$  is used as feedback to control the distance of the scanning tip to achieve constant  $\Delta f$ , recording the resulting  $z$ -coordinate as image (analogous to constant-current mode in STM). In constant-height mode the tip is scanning at a fixed  $z$ -coordinate and the measured  $\Delta f$  is recorded as image. The (constant)  $z$ -drift and slope have to be compensated in constant-height mode.

#### Amplitude

The oscillation amplitude influences both the contribution of short and long range forces to the frequency shift, as well as the frequency noise ([79, p. 125]). Short-range forces (characteristic interaction range  $\lambda$ ) dominate at  $A \leq 3\lambda$  while long-range forces dominate at larger amplitudes. Thus, using a small amplitude might help in achieving atomic resolution but at the same time frequency noise is proportional to  $1/A$ , see below.

#### Thermal and detector noise

The minimum detectable force gradient, *i.e.* the resolution of FM nc-AFM, is limited by the thermal noise of the sensor  $\delta f_T$  and the detector noise  $\delta f_{\text{det}}$ . The thermal noise can be written as<sup>78</sup>

$$\delta f_T \propto \sqrt{\frac{T}{k A^2 Q}}. \quad (2.12)$$

When operating at low temperature and using stiff sensors (typical values:  $T = 5 \text{ K}$ ,  $k \approx 2000 \text{ N/m}$ ,  $Q \approx 20000$ )  $\delta f_T$  is usually smaller than the detector noise.  $\delta f_{\text{det}}$  is

---

<sup>i</sup>Albrecht *et al.*<sup>78</sup> made the comparison to the older slope detection mode (*i.e.*, amplitude modulation detection) where the sensor is driven with a constant frequency close to the resonance frequency; a change of the resonance frequency causes a change in the amplitude that is then detected.

given by (see [79, p. 127])

$$\delta f_{\text{det}} = \frac{n_{q'}}{\pi A f_0} B^{3/2}, \quad (2.13)$$

where  $B$  is the bandwidth and  $n_{q'}$  is the deflection noise density of the frequency detector, making  $n_{q'}$  the limiting factor.<sup>80</sup>

### Image Contrast

Pioneering works on oxide surfaces show that the AFM contrast is governed by the electric charge of the tip apex.<sup>81,82</sup> “Positively terminated” tips interact attractively with anions, and repulsively with cations. “Negative tips” show the opposite behaviour.

### The qPlus sensor<sup>ii</sup>

The qPlus sensor was invented by Franz J. Giessibl<sup>62</sup> and is based on a quartz tuning fork<sup>83,84</sup>, see Figure 2.3a. One of the prongs of the tuning fork is fixed to a substrate while the other prong has a sharp tip attached to its end and is free to oscillate. The oscillation of the sensor is excited by adding a voltage (mV range) to the  $z$ -piezo voltage of the scanner. When oscillating, the prong is bent upwards and downwards; electrodes collect the surface charges that emerge due to the piezoelectric effect resulting in a deflection current,  $I_{\text{def}}$ , in the pA range.  $I_{\text{def}}$  is fed to a preamplifier<sup>80</sup> that converts the current to a voltage used as sensor deflection signal in the AFM control unit. A separate wire or electrode contacts the tip for the detection of the tunneling current when the sample is biased. Different build types of the qPlus sensor are available;<sup>85</sup> the sensors used in the present thesis had a resonance frequency of approximately 31 kHz and a separate electrode for contacting the tip, see Figure 2.3b.

## 2.4.2 Kelvin Probe Force Microscopy

Kelvin Probe Force Microscopy (KPFM) is a method to determine the work function difference between tip and sample. When two metals of different work function are electrically connected, a current flows until the Fermi levels are aligned; the electrostatic contact potential difference (CPD) between the two metals is then equal to

<sup>ii</sup>While there are different sensor builds for AFM available, only the qPlus sensor that is used in the present thesis will be discussed.



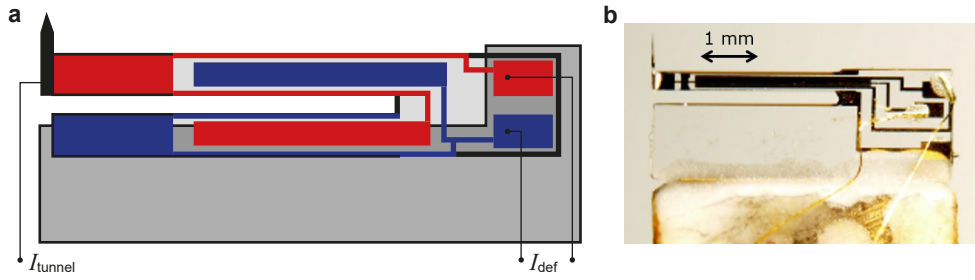


**Figure 2.3 | The qPlus sensor.** **a)** Schematic of the sensor. The bottom prong is fixed to the substrate, the top prong with its attached tip is free to oscillate. Electrodes (red and blue) collect the deflection current, the tip is separately contacted for the tunneling current. After ref. [85]. **b)** Photo of the qPlus sensor-type used in the present thesis. A separate electrode on the upper prong connects the tip to the contact in the back, where a wire is attached. Photo by Martin Setvin.

the work function difference of the metals. If the tip is calibrated against a sample of known work function, the work function of an unknown sample can be determined.

The local CPD (LCPD) is measured by recording the frequency shift while varying the sample bias voltage,  $V_s$ . The tip and sample can be modelled as the two plates of a capacitor; the electrostatic force between the plates is ([73, p. 201])

$$F_{\text{el}} = \frac{1}{2} \frac{dC}{dz} \Delta V^2, \quad (2.14)$$

where  $C$  is the capacitance of the tip-sample capacitor, and  $\Delta V = V_s - V_{\text{LCPD}}$  is the potential difference. Since  $C$  is proportional to  $1/d$ , the gradient of  $F_{\text{el}}$  is non-zero. The resulting frequency shift describes a parabola with respect to the sample bias voltage  $V_s$ . When the frequency shift is minimal (the vertex of the parabola), the sample bias voltage is equal to the work function difference of tip and sample ( $V_s = V_{\text{LCPD}}$ ). This method can be used to determine the charge state of adatoms.<sup>86</sup>

## 2.5 X-ray Photoelectron Spectroscopy

X-ray photoelectron spectroscopy (XPS) relies on the ejection of a core-level electron by an X-ray photon of energy  $h\nu$ , where  $\nu$  is the frequency of the photon. The kinetic energy  $E_K$  of the ejected electron is measured by an electron energy analyzer; the binding energy of the electron  $E_B$  is then given by

$$E_B = h\nu - E_K - \phi_A, \quad (2.15)$$

where  $e\phi_A$  is the work function of the analyzer, see Figure 2.4. The recorded XPS spectrum (count of electrons against  $E_B$ ) allows identification of the elements as well as the chemical environment due to core level shifts (*i.e.*, chemical shift).

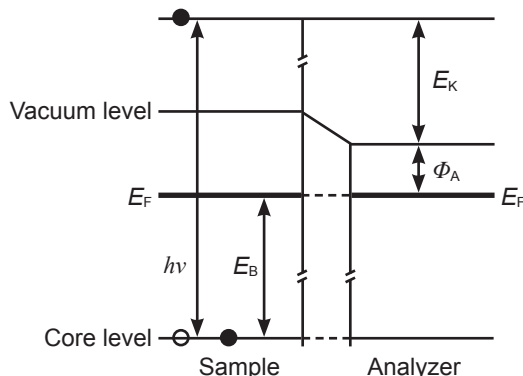


Figure 2.4 | Energy diagram of X-ray Photoelectron Spectroscopy.

## 2.6 Density Functional Theory

All DFT calculations were performed at the Center for Computational Materials Science by our close collaborators Wernfried Mayr-Schmölzer, Florian Mittendorfer and Josef Redinger.<sup>87</sup> Results of their work that were essential for interpreting certain experimental findings were included in this thesis and are clearly referenced. Computational details are available in the PhD thesis of Wernfried Mayr-Schmölzer<sup>88</sup> and in our jointly published articles.<sup>89–91</sup>

# Chapter 3

## The Cleaved Surface of $\text{Ca}_3\text{Ru}_2\text{O}_7$

The (001) surface of  $\text{Ca}_3\text{Ru}_2\text{O}_7$  was prepared by cleaving, a technique successfully applied to other Ruddlesden-Popper compounds such as  $\text{Sr}_2\text{RuO}_4$  and  $\text{Sr}_3\text{Ru}_2\text{O}_7$  (see ref. [13] and references therein),  $\text{Sr}_3\text{Ir}_2\text{O}_7$ <sup>92</sup> and  $\text{La}_{1.4}\text{Sr}_{1.6}\text{Mn}_2\text{O}_7$ .<sup>93</sup> For details on the sample preparation leading up to the cleaving see Section 2.2.2. This chapter describes the pristine surface and the observed surface defects.

### 3.1 The CaO-terminated surface

As mentioned in Chapter 1, the  $n = 2$  member of the Ruddlesden-Popper series consists of stacks of two perovskite-like  $\text{CaRuO}_3$  units separated by a double CaO layer along [001], see Figure 3.1a. The lattice constants of the orthorhombic unit cell are  $a = 5.365 \text{ \AA}$ ,  $b = 5.562 \text{ \AA}$ ,  $c = 19.525 \text{ \AA}$ .<sup>87</sup> According to DFT calculations<sup>87</sup> the plane between the double CaO layer has the lowest cleaving energy of 3.62 eV per unit cell, or 0.91 eV per Ca-O bond. The two other potential cleaving planes, that are located between the outer CaO and the  $\text{RuO}_2$  layer underneath, and this  $\text{RuO}_2$  and the central CaO layer, have significantly higher cleaving energies of 6.23 eV and 5.28 eV per unit cell, respectively.

Figure 3.1b shows the structure of the CaO-terminated surface expected after cleaving. The Ca form an almost perfect square sublattice, the O sublattice is distorted due to the alternate tilt and rotation of the  $\text{RuO}_6$  octahedra. The tilt of approximately  $13^\circ$  is most pronounced in the  $ac$  plane. The structure has a  $b$  glide plane that results in a mirrored appearance of features that are shifted by a half-integer number of lattice constants in [010] direction. In the STM simulation<sup>87</sup> (Tersoff-Hamann approximation<sup>70</sup>) the dark (bright) lines along [010] correspond to areas where the

apical oxygen atoms of the  $\text{RuO}_6$  octahedra are tilted toward (away from) each other, see Figure 3.1c. Here only an STM simulation is shown as the simulation of atomically-resolved nc-AFM is more involved, since the tip has to be taken into account explicitly.

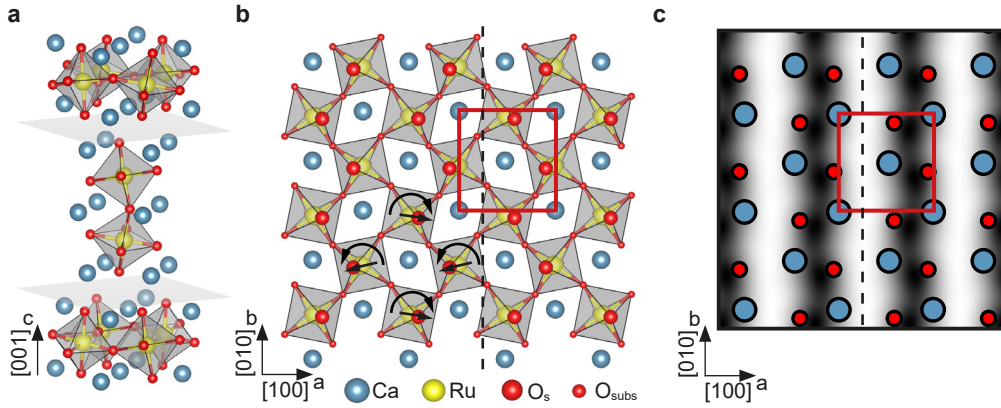


**Figure 3.1 | DFT model<sup>87</sup> of the cleaved  $\text{Ca}_3\text{Ru}_2\text{O}_7(001)$  surface.** a) Unit cell of  $\text{Ca}_3\text{Ru}_2\text{O}_7$ . The crystal cleaves easily between neighboring CaO layers (marked by *grey planes*). b) Top view of the CaO-terminated (001) surface. The octahedra are alternately tilted and rotated as indicated by the *straight and curved arrows*, respectively. The *red box* marks the orthorhombic unit cell ( $a = 5.365 \text{ \AA}$ ,  $b = 5.562 \text{ \AA}$ ). The *dashed line* marks the glide plane. c) STM simulation,  $V_s = +0.8 \text{ V}$ .

Typical STM and AFM images of the pristine surface are shown in Figure 3.2. The STM image shows wide bright and narrow dark lines along [010] in accordance with the STM simulation (Figure 3.1). The bright lines exhibit weak undulations the visibility of which depends on the quality of the particular STM tip. The bright-dark contrast of the lines is same for filled and empty states but empty state images usually yielded better resolution. The constant-height AFM image in Figure 3.2b shows bright dots arranged in zigzag lines; by comparison with simultaneously recorded STM images, the bright dots are attributed to the O atoms that interact more repulsively (less attractively) and thus are shown bright (less negative  $\Delta f$ ). As mentioned previously, pioneering works on oxide surfaces showed that the AFM contrast is governed by the electric charge of the tip apex.<sup>81,82</sup> “Positively terminated” tips interact attractively with anions, and repulsively with cations. “Negative tips” show the opposite behaviour. The contrast in Figure 3.2b corresponds to the negative termination. Terraces are typically at least a few hundred nm in size.

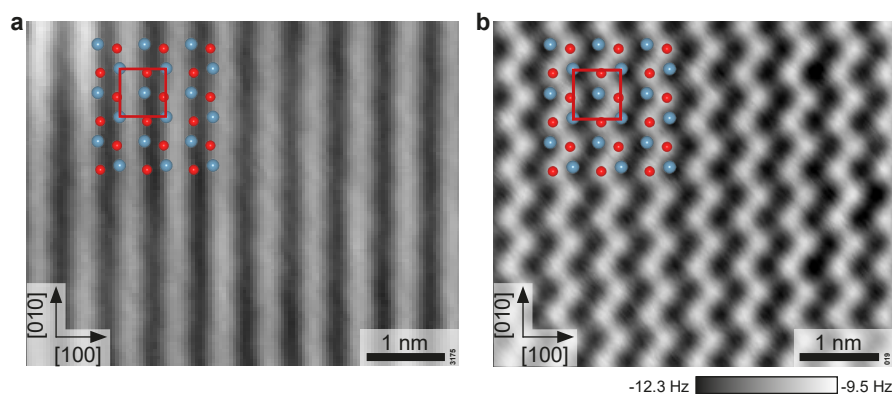


**Figure 3.2 | STM and AFM image of the pristine  $\text{Ca}_3\text{Ru}_2\text{O}_7(001)$  surface.** The overlay shows the surface atoms; Ca – blue, O – red. **a)** Constant-current STM image. The bright and dark lines along  $[010]$  are in agreement with STM simulations. STM parameters:  $V_s = +0.8$  V,  $I_t = 0.1$  nA,  $T_s = 78$  K **b)** Constant-height AFM image. The surface O atoms are shown as bright dots arranged in zigzag lines along  $[010]$ . AFM parameters:  $A = 100$  pm,  $V_s = +0.25$  V,  $T_s = 4.8$  K

### 3.1.1 Point defects

The majority of the as-cleaved surfaces showed approximately 0.6 % ML (monolayer, with respect to Ca surface atoms) of point defects; the highest concentration ever observed was 1.6 % ML. The large-area STM image in Figure 3.3a shows 0.7 % ML of the typically observed point defects. The majority of defects is surrounded by a bright halo; more weakly appearing features of same size and shape are seen as well. The appearance of the defects depends on the tip condition and on the sample bias voltage; the surrounding halo is usually more pronounced at sample bias voltages lower than +0.5 V. The detailed STM image in Figure 3.3b shows that the defects appear as a “normal” and a mirrored version, where the  $b$ -axis ( $[010]$ ) is the mirror axis. This is explained by the glide plane along the  $b$ -axis (see Figure 3.1c); defects that are mirrored to each other are shifted by a half-integer number of lattice constants along  $[010]$ .

The cause for the point defects could be bulk impurities, adsorbates from the residual gas, or defects created during cleaving. According to DFT calculations<sup>87</sup> the formation energy per Ca and O vacancy is 5.3 eV and 3.9 eV, respectively, and thus significantly higher than the cleaving energy per broken Ca-O bond of 0.92 eV. Additionally, the presence of O vacancies can be ruled out since their appearance in STM is known from intentionally-created O vacancies (see Section 4.2.4).

The main constituents of the residual gas in the UHV systems were  $\text{H}_2$ , CO,  $\text{CO}_2$

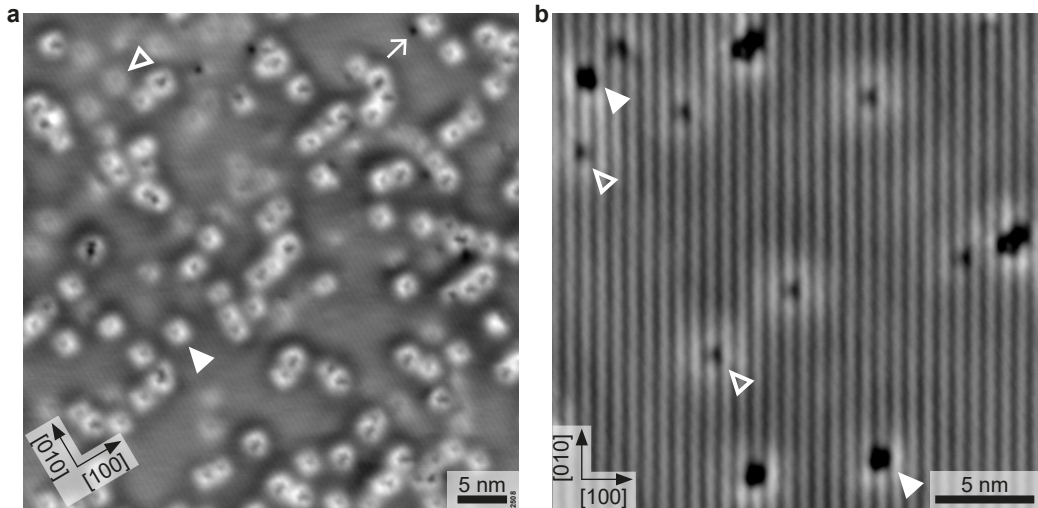


**Figure 3.3 | Point defects of the as-cleaved surface.** **a)** The majority of defects appear as dark dots surrounded by a bright halo; the defects appear with a strong (*full triangle*) and weak (*open triangle*) contrast. A few defects of different type without halo were observed as well (*arrow*). STM parameters:  $V_s = +0.4$  V,  $I_t = 0.1$  nA,  $T_s = 78$  K **b)** Different sample, tip and sample bias voltage than in panel **a**. The *triangles* mark the same kind of defects as in panel **a**. Defects appear mirrored across the *b*-axis ([010]). STM parameters:  $V_s = +0.8$  V,  $I_t = 0.1$  nA,  $T_s = 78$  K

and  $\text{H}_2\text{O}$  with partial pressures in the low  $10^{-11}$  mbar range. However, the observed point defect concentration is too high to be explained by exposure to the residual gas in the time between cleaving and measurement. Also the surface was intentionally exposed to  $\text{H}_2\text{O}$  and CO (see Chapters 4 and 6), that were shown to appear and/or interact differently than the point defects.

This leaves bulk impurities as source of the defects. The composition of two samples was analyzed by Laser Ablation Inductively Coupled Plasma Mass Spectrometry (LA-ICP-MS). Table 3.1 shows that the main impurities are Ti, Sr and Mg. Ti was found to be the main impurity with 0.06 %  $c_{\text{Ti}}/c_{\text{Ru}}$  followed by Sr with 0.013 %  $c_{\text{Sr}}/c_{\text{Ca}}$  and Mg with 0.009 %  $c_{\text{Mg}}/c_{\text{Ca}}$ ; the concentrations are virtually the same for the two investigated samples. The total impurity concentration of 0.08 % ML measured by LA-ICP-MS is by a factor of eight smaller than the point defect concentration observed in STM images. That might be explained by an inhomogeneous distribution of the impurities in the grown single crystal and a preferred cleaving along planes of increased defect concentration. A similar discrepancy (by a factor of four) was found for  $\text{Sr}_3\text{Ru}_2\text{O}_7$ .<sup>13</sup>

Sr and Mg are expected to substitute Ca; Ti is expected to substitute Ru. Therefore

Sample	Mg [ppm]	c_Mg/c_Ca [%]	Sr [ppm]	c_Sr/c_Ca [%]	Ti [ppm]	c_Ti/c_Ru [%]
CRO-17	13	0.008	80	0.013	136	0.06
CRO-22	15	0.009	80	0.013	135	0.06

**Table 3.1 | Impurity concentrations measured by LA-ICP-MS.** The concentrations were measured in weight ppm and converted to relative concentrations depending on whether Ca or Ru would be replaced by the impurity. Measurement by Prof. Andreas Limbeck, Institute of Chemical Technologies and Analytics, TU Wien.

the point defects should appear either at a Ca or  $O_{\text{surf}}$  (since Ru is located beneath  $O_{\text{surf}}$ ) lattice site. However, the exact position of Ca and  $O_{\text{surf}}$  can not be deduced from STM images because the contrast of bright and dark lines is not related to a specific lattice site, see Figure 3.1c. Also mirrored versions of the defects are expected for both, the Ca and  $O_{\text{surf}}$ /Ru lattice site due to the glide plane.

Based on the fact that Ti is the main impurity according to the LA-ICP-MS analysis, the majority of the observed point defects is assumed to be Ti substituting Ru. The strong and weak contrast in STM (Figure 3.3) is attributed to substitution in the first and second  $\text{RuO}_2$  subsurface layer, respectively. The less frequently observed defects (without halo in Figure 3.3a) are tentatively assigned to Mg or Sr substituting Ca.

### 3.1.2 Line and area defects

Line and area defects were observed on the surface of roughly half of the investigated samples, see Figure 3.4. Line defects run most frequently along the [010] direction with occasional kinks of a few unit cells in the [100] direction. On  $\text{Sr}_3\text{Ru}_2\text{O}_7$  line defects were found to be domain boundaries regarding the rotation of the octahedra;<sup>13</sup> an analogous conclusion could not be drawn for  $\text{Ca}_3\text{Ru}_2\text{O}_7$ .

Area defects appear as elongated pits along the [010] direction and are roughly 240 pm deep. This value is close to the inter-layer distance of the CaO and  $\text{RuO}_2$  sheets of roughly 200 pm. Therefore it may be speculated that the pits are  $\text{RuO}_2$ -terminated, but no atomically-resolved images inside the pits could be obtained.

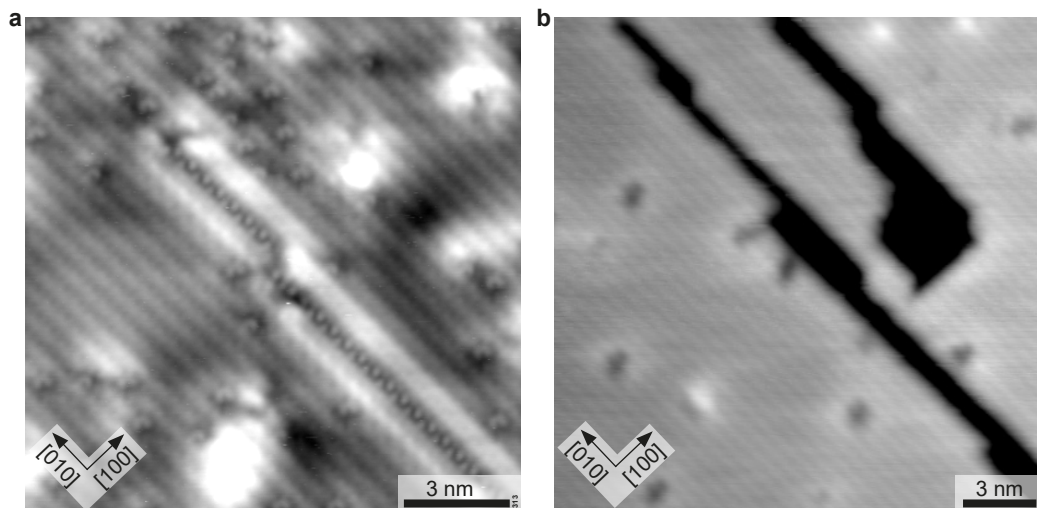


**Figure 3.4 | Line and area defect.** **a)** Unidentified line defect along the  $[010]$  direction. (The other features are physisorbed CO molecules imaged with an unusual tip state, see Chapter 6.) STM parameters:  $V_s = +0.4 \text{ V}$ ,  $I_t = 0.1 \text{ nA}$ ,  $T_s = 78 \text{ K}$  **b)** The pits are approximately 250 pm deep. STM parameters:  $V_s = +0.8 \text{ V}$ ,  $I_t = 0.1 \text{ nA}$ ,  $T_s = 78 \text{ K}$

## 3.2 Unsuccessful cleaving

The sample cleaving was not always successful with regard to producing a surface that could be investigated by STM and AFM. The success rates were approximately 70 and 50 % for new and old samples, respectively; new and old referring to storage times of approximately 1 and 4 years, respectively. Unsuccessful cleaving resulted in either roughness on the nm-scale; a high density of line and area defects often connected with unidentified nm-high hills (“dirt”); or samples that were not electrically conducting enough for STM. Two examples are shown in Figure 3.5.

The cause for the unsuccessful cleaving may be a combination of sample degradation during storage (humidity), varying impurity contents and cleaving along areas of aggregated impurities. Furthermore, the samples may have already developed unnoticed cracks along such areas while handling the ready-to-cleave assembly (sample plate, sample, metal stud) in the ambient, although care was taken not to expose the samples to vibrational shock.



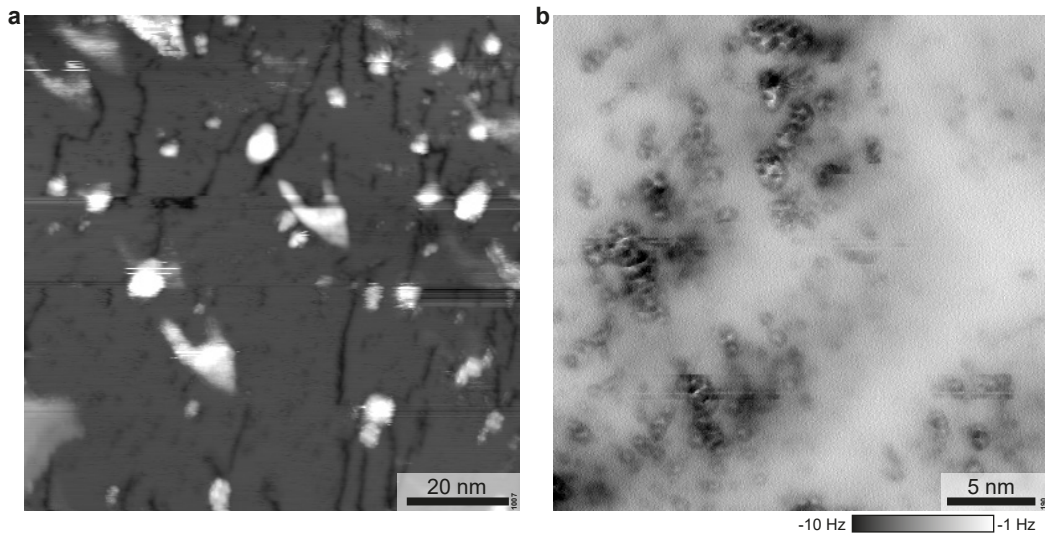


**Figure 3.5 | Surfaces of unsuccessful cleavings.** **a)** STM image of a surface with a network of line and area defects and hills up to 1 nm in height. STM parameters:  $V_s = +1.0$  V,  $I_t = 0.05$  nA,  $T_s = 78$  K **b)** Constant-height AFM image of a non-conductive sample. The otherwise flat surface shows patches with a high density of point defects. AFM parameters:  $A = 300$  pm,  $V_s = 0$  V,  $T_s = 4.8$  K

### 3.3 Summary

Cleaving of  $\text{Ca}_3\text{Ru}_2\text{O}_7$  in UHV produces flat, CaO-terminated terraces that are typically at least a few hundred nm in size. The STM contrast of bright and dark lines along [010] corresponds to areas where the apical oxygen atoms of the  $\text{RuO}_6$  octahedra are tilted toward (away from) each other. In AFM the  $\text{O}_{\text{surf}}$  appear as bright dots (less attractive interaction) arranged in zigzag lines along [010]. The point defects are attributed to impurities from the growth process; based on a LA-ICP-MS measurement the majority of point defects is assumed to be subsurface Ti substituting Ru. Line and area defects, and unsuccessful cleaving were encountered more often than with the related strontium ruthenates,  $\text{Sr}_2\text{RuO}_4$  and  $\text{Sr}_3\text{Ru}_2\text{O}_7$ .<sup>13</sup>



# Chapter 4

## H<sub>2</sub>O Adsorption on Ca<sub>3</sub>Ru<sub>2</sub>O<sub>7</sub>

This chapter is based on an article published in *Nature Communications* **8**, 23 (2017), Ref. [90]. However, this chapter contains additional information not available in the published article.

### 4.1 Introduction

Surface science can deliver microscopic insight into the interaction of water with metal<sup>94</sup> and metal-oxide surfaces<sup>95</sup> on the atomic-level. The very first and fundamental question is whether a molecule in direct contact with the surface will adsorb as an intact entity or dissociate. This is governed by the subtle energy differences between interaction of water with the surface-cation on the one side and H bonding to surface O atoms on the other, and was addressed for several binary transition metal oxides. Molecular adsorption was found for water on anatase TiO<sub>2</sub>(101)<sup>96,97</sup> and on FeO(111)<sup>98</sup>. On defect-free rutile TiO<sub>2</sub>(110)<sup>99,100</sup> and RuO<sub>2</sub>(110)/Ru(0001)<sup>101,102</sup> water adsorbs molecularly as well, but an equilibrium between molecular and short-lived dissociated states is under debate.<sup>102</sup> Mixed molecular and dissociative adsorption of water was observed on Fe<sub>3</sub>O<sub>4</sub>(001),<sup>103</sup> Fe<sub>3</sub>O<sub>4</sub>(111)<sup>103</sup> and ZnO(10 $\bar{1}$ 0).<sup>104</sup> Water was found to exclusively dissociate on the (1 × 1) and (2 × 1) surfaces of  $\alpha$ -Fe<sub>2</sub>O<sub>3</sub>(012),<sup>105</sup> as well as  $\alpha$ -Fe<sub>2</sub>O<sub>3</sub>(0001)<sup>103</sup> and In<sub>2</sub>O<sub>3</sub>(111).<sup>106</sup>

The AO-terminated surfaces of perovskites are closely related to the (001) surfaces of the binary alkaline earth oxides. On MgO(001) water partially dissociates and forms two stable structures with c(4 × 2) or p(3 × 2) symmetry, depending on temperature.<sup>107</sup> As already mentioned in Chapter 1, on CaO(001) mixed dissociative and molecular adsorption were experimentally observed at very low coverages.<sup>54</sup> In a

density functional theory study Hu *et al.*<sup>51</sup> derived two key factors that facilitate the dissociation of water on alkaline earth oxides: (i) an increase in the lattice constant, which enhances hydrogen bonding with the substrate, and (ii) the flexibility of the substrate. On the SrO-terminated (001) surfaces of the layered perovskites Sr<sub>3</sub>Ru<sub>2</sub>O<sub>7</sub> and Sr<sub>2</sub>RuO<sub>4</sub> it was shown that the water monomer adsorption also follows these key factors.<sup>89</sup> Water dissociates into a (OH)<sub>ads</sub>, adsorbed on a cation-cation bridge site, and a proton that forms a surface hydroxyl with a surface oxygen atom. The (OH)<sub>ads</sub> stays trapped by the surface hydroxyl, circling it by jumping between the four adjacent Sr-Sr bridge positions (see Chapter 5). The dynamic behaviour of these ion pairs was predicted by theory.<sup>52</sup>

The RuO<sub>6</sub> octahedra of Ca<sub>3</sub>Ru<sub>2</sub>O<sub>7</sub> are rotated in the ab plane and tilted with respect to the c axis (see Chapter 3). This affects the position of the surface O atom with respect to the four surrounding Ca-Ca bridge positions on the CaO-terminated surface, rendering these sites inequivalent for water adsorption. It is shown that the distance between a bridge site and its neighbouring surface oxygen atoms is a pivotal factor for the water adsorption. Distinct ordering of the dissociated water is observed, which can be fully rationalized with the surface geometry formed by the underlying octahedra. Based on accompanying DFT calculations,<sup>87</sup> detailed structural models for the (2 × 1), (1 × 3) and (1 × 1) OH overlayers are presented.

## 4.2 Results

### 4.2.1 The monomer and the low-coverage overlayer

After exposing the Ca<sub>3</sub>Ru<sub>2</sub>O<sub>7</sub>(001) surface to a water dose of 0.3 Langmuir (L, where 1 L equals an exposure to  $1.0 \times 10^{-8}$  mbar for 133 s) at 105 K, STM images show single, bright spots, see Figure 4.1a. These spots are separated by at least one lattice constant and sit exclusively on top of the bright substrate lines. Additionally, a few larger, bright features are observed. Annealing the sample for 1 hour at room temperature (RT) leads to a single-spot coverage increase from 0.13 ML to 0.34 ML, see Figure 4.1b. One ML is defined as two H<sub>2</sub>O per unit cell. This substantial increase suggests that the larger features (observed before annealing) contained several H<sub>2</sub>O molecules that became mobile and dispersed across the surface. In a locally more densely covered area, six neighbouring substrate lines are occupied, see Figure 4.1b.

This results in a local  $(2 \times 1)$  symmetry. The spots along the same substrate line are spaced one lattice constant apart from each other. On the neighbouring line the spots are shifted by half a lattice constant along  $[010]$ . Alternating narrow and wide gaps separate the spots in  $[100]$  direction. Occasionally, spots separated by only half a lattice constant along  $[010]$  are observed. This new feature is named bright-dark feature as one of the spots is darker than the other.

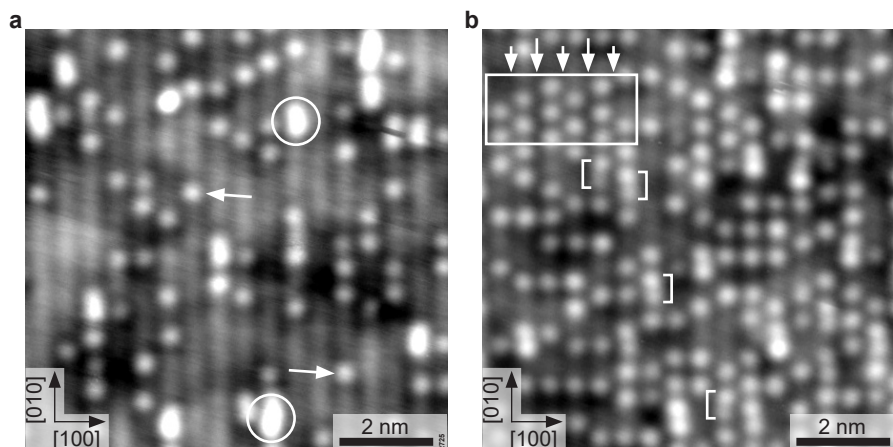


**Figure 4.1 | Low dose of  $\text{H}_2\text{O}$  on  $\text{Ca}_3\text{Ru}_2\text{O}_7(001)$ .** **a)** STM image of 0.3 L  $\text{H}_2\text{O}$  dosed at 105 K. Single, bright spots (*arrows*, 0.13 ML) sit on the bright substrate lines and are at least one lattice constant spaced apart. The larger, brighter features (*circles*) probably contain several  $\text{H}_2\text{O}$  molecules. **b)** The sample in panel **a** after annealing for 1 hour at RT. The *box* marks a more densely covered area with local  $(2 \times 1)$  symmetry. Alternating narrow and wide gaps separate the spots in  $[100]$  direction, marked by *short and long arrows*, respectively. The *brackets* mark spots separated by half a lattice constant along  $[010]$ , named bright-dark feature. STM parameters:  $V_s = -0.8 \text{ V}$ ,  $I_t = 0.1 \text{ nA}$ ,  $T_s = 78 \text{ K}$ ; fast scan direction is  $18^\circ$  clockwise from horizontal.

### The monomer configuration

A unit cell model of the pristine surface is shown in Figure 4.2a. The unit cell has inequivalent adsorption sites labelled as surface oxygen atoms ( $\text{O}_{\text{surf}}$ ) O1 and O2, and Ca-Ca bridge sites B1 to B4. The inequivalence is caused by the rotation and tilting of the  $\text{RuO}_6$  octahedra, leading to different distances between the  $\text{O}_{\text{surf}}$  and the bridge sites, see Table 4.1. DFT calculations<sup>87</sup> predict that a single water molecule dissociates without a barrier, forming an  $(\text{OH})_{\text{ads}}$  group adsorbed on a bridge site, with the split-off H transferred to a neighboring  $\text{O}_{\text{surf}}$ . The adsorption energy depends on which bridge site the  $(\text{OH})_{\text{ads}}$  fragment is placed with respect to the  $\text{O}_{\text{surf}}$ . If the split-off H is adsorbed on O1, the  $(\text{OH})_{\text{ads}}$  is clearly preferred to sit on B1 (named

B1O1 configuration) with an overall adsorption energy of  $E_{\text{ads\_B1O1}} = 1.64$  eV, see Figure 4.2c,d. Compared to the pristine surface the tilt angle of the hydroxylated RuO<sub>6</sub> octahedron increases from 12.9° to 16.3°.

Bridge-O1	Distance [Å]	Bridge-O2	Distance [Å]
B1	2.56	B1	1.98
B2	1.98	B2	2.56
B3	1.29	B3	1.90
B4	1.90	B4	1.29

**Table 4.1 | Bridge site to surface oxygen distances.** The distances are constructed according to the sketch in Figure 4.2a.

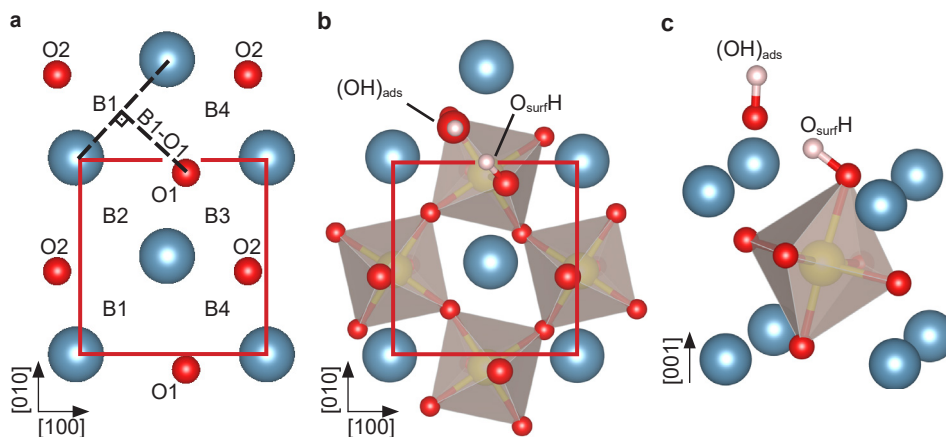


**Figure 4.2 | DFT model for water adsorption on Ca<sub>3</sub>Ru<sub>2</sub>O<sub>7</sub>(001).** **a)** Top view DFT model<sup>87</sup> of the pristine surface; Ca – blue, Ru – yellow, O – red, H – white. The unit cell is marked by the *rectangle*. The distance B1-O1 is shown as an example, other distances are constructed analogously. **b)** Top view and **c)** perspective view of the most preferred configuration B1O1 for one dissociated water monomer with  $E_{\text{ads\_B1O1}} = 1.64$  eV. The (OH)<sub>ads</sub> adsorbs on the Ca-Ca bridge site B1, the split-off H is transferred to the neighbouring surface oxygen atom O1. The energetically equivalent configuration B2O2 is not shown. (Only the first subsurface layer of RuO<sub>6</sub> octahedra is shown.)

In the optimum adsorption position B1O1, the calculated<sup>87</sup> adsorption energy of the dissociated molecule (1.64 eV) is significantly higher than for the intact water molecule (0.78 eV). The Ca-O distance of the (OH)<sub>ads</sub> fragment is 2.39 Å. The OH bond length of 0.97 Å for the (OH)<sub>ads</sub> fragment is slightly smaller than the value of 1.03 Å found for the O<sub>surf</sub>H bond. The latter bond is tilted which allows the formation of an additional hydrogen bond (O-O distance 2.57 Å, classified as strong hydrogen bond<sup>94</sup>) to the (OH)<sub>ads</sub> fragment, with an H-(OH)<sub>ads</sub> distance of 1.55 Å. The (OH)<sub>ads</sub> does not sit centred on the bridge site but slightly closer to its respective O<sub>surf</sub>H.

The STM simulation in Figure 4.4a shows the  $(\text{OH})_{\text{ads}}$  as a bright spot on the bright substrate line, see Figure 4.4a. The single, bright spots in the STM images (Figure 4.1) are thus interpreted as the  $(\text{OH})_{\text{ads}}$  of the dissociated water monomers.

The calculated<sup>87</sup> adsorption energy, the O-Ru-O bond angle along the octahedron's  $c$  axis and O-O distances between the  $(\text{OH})_{\text{ads}}$  and the  $\text{O}_{\text{surf}}$  for all monomer configurations are listed in Table 4.2. The adsorption energy decreases with increasing distortion of the hydroxylated octahedron, reflected in the decreasing O-Ru-O bond angle. The O-O distance between the  $(\text{OH})_{\text{ads}}$  and the  $\text{O}_{\text{surf}}$  is similar for all configurations. The adsorption geometries B2O1 and B3O1 are shown in Figure 4.3. The configuration B4O1 is not stable, resulting in diffusion of the  $(\text{OH})_{\text{ads}}$  to the most preferred B1 site. If the split-off H is adsorbed on O2, the preferred bridge site is B2 as the same calculation applies, but for symmetry reasons the roles of B1 and B3 switch with B2 and B4, respectively.

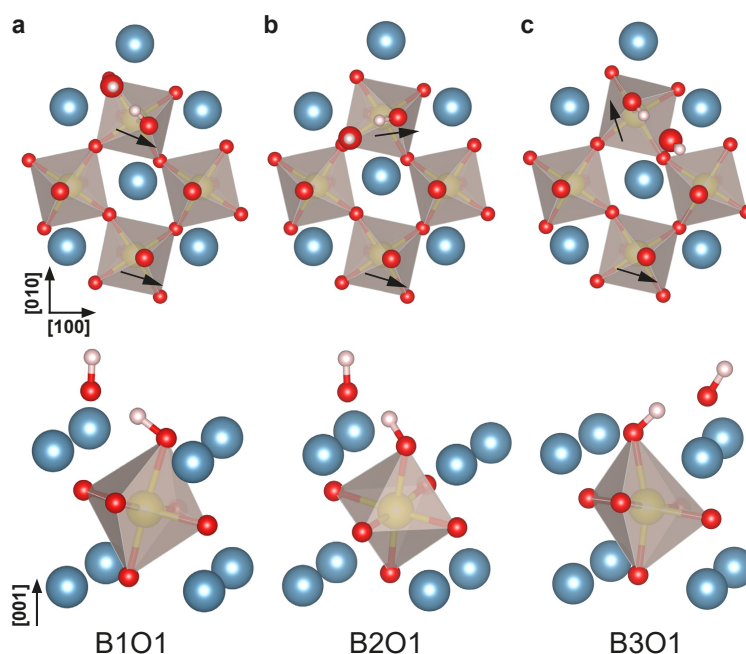


**Figure 4.3 | Top and side view DFT models<sup>87</sup> of the different monomer adsorption configurations.** Ca – blue, Ru – yellow, O – red, H – white. The *arrows* mark the tilt direction of the apical oxygen of the hydroxylated and regular octahedra. The decreasing adsorption energy ( $\text{B1O1} > \text{B2O1} > \text{B3O1}$ ) follows the increasingly deviating tilt direction and the decreasing O-Ru-O bond angle (see Table 4.2)

Configuration	$E_{\text{ads}}$ [eV]	O-Ru-O [ $^\circ$ ]	$(\text{OH})_{\text{ads}}\text{-O1}$ [ $\text{\AA}$ ]	$(\text{OH})_{\text{ads}}\text{-O2}$ [ $\text{\AA}$ ]
B1O1	1.64	177.6	2.56	3.0
B2O1	1.44	176.2	2.52	3.18
B3O1	0.78	161.9	2.5	2.81

**Table 4.2 | Adsorption energies and geometry details of the monomer configurations.**<sup>87</sup> The O-Ru-O bond angle of the hydroxylated octahedron is given.

### The $(2 \times 1)$ overlayer

The locally observed  $(2 \times 1)$  symmetry in the STM image in Figure 4.1b is explained by the  $(2 \times 1)$  overlayer model in Figure 4.4b. Monomers along  $[010]$  are spaced one lattice constant apart. In a monomer line along  $[010]$  only the most favourable configurations are occupied, *i.e.*, B1O1 in one line and the symmetrically equivalent B2O2 in the adjacent lines. The narrow and wide gaps between the lines is caused by the opposite shift in  $[100]$  of the  $(\text{OH})_{\text{ads}}$  in adjacent lines as the  $(\text{OH})_{\text{ads}}$  sits slightly closer to its respective  $\text{O}_{\text{surf}}\text{H}$  (Figure 4.4a). The calculated<sup>87</sup> adsorption energy decreases by 20 meV per  $\text{H}_2\text{O}$  molecule compared to the isolated water monomer, suggesting slightly repulsive interaction between the  $(\text{OH})_{\text{ads}}$  (see Table 4.2).

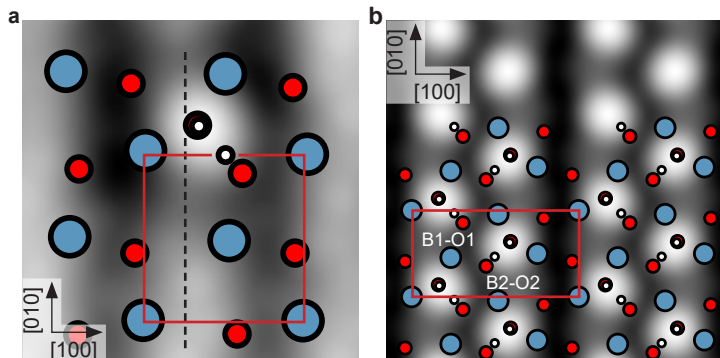


**Figure 4.4 | STM simulation of the dissociated monomer and DFT model of the  $(2 \times 1)$  overlayer.**<sup>87</sup> Ca – blue, O – red, H – white. **a)** The  $(\text{OH})_{\text{ads}}$  appears as a bright spot. When compared to the Ca-Ca bridge center (*dashed line*), the  $(\text{OH})_{\text{ads}}$  sits slightly closer to the  $\text{O}_{\text{surf}}\text{H}$  in  $[100]$  direction. The unit cell is marked by the *rectangle*. **b)** The  $(2 \times 1)$  overlayer (0.5 ML coverage) consists of monomers with one lattice constant spacing along  $[010]$ , leading to occupation of either the B1O1 or the symmetrically equivalent B2O2 configuration. In adjacent lines the monomers are shifted by half a lattice constant in  $[010]$  direction and thus occupy the other configuration. Therefore the  $(\text{OH})_{\text{ads}}$  on adjacent lines are slightly shifted in opposite directions along  $[100]$ , leading to narrow and wide gaps between the lines.

For the bright-dark feature no DFT model was found. This feature is tentatively



assigned to two  $(\text{OH})_{\text{ads}}$  on neighbouring bridge sites, i.e. B1O1 and B2O2, with one of the  $(\text{OH})_{\text{ads}}$  appearing darker than the other as it might be in a slightly different configuration.

## 4.2.2 The high-coverage overlayers

### The $c(2 \times 6)$ overlayer

Increasing the dose to the pristine surface to 0.5 L at 100 K, and annealing for 1 h at RT leads to a  $c(2 \times 6)$  OH overlayer that covers the whole surface, see Figure 4.5. The OH overlayer is now compressed along  $[010]$ ; 7  $(\text{OH})_{\text{ads}}$  are found on 6 unit cells, with a shift by half an OH-OH distance between adjacent lines. The  $(\text{OH})_{\text{ads}}$  along  $[010]$  do not form perfectly straight lines, but slightly undulate. The coverage increase from 0.34 ML to  $7/12 = 0.58$  ML (again, with respect to  $\text{O}_{\text{surf}}$  or Ca sites) fits well to the dose increase from 0.3 L to 0.5 L when compared to the coverage of the sample in Figure 4.1b.

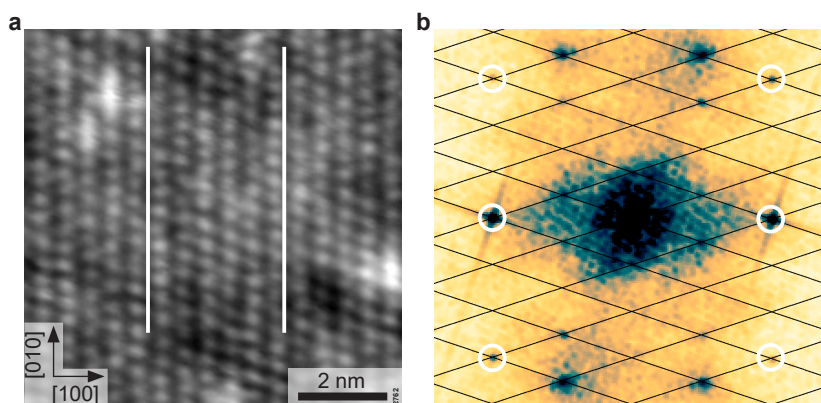


**Figure 4.5 | The  $c(2 \times 6)$  overlayer.** **a)** STM image of 0.5 L  $\text{H}_2\text{O}$  dosed at 110 K and subsequently annealed for 1 h at RT. The  $(\text{OH})_{\text{ads}}$  along  $[010]$  are not perfectly straight but slightly undulate (compare to the *lines*). STM parameters:  $V_s = -0.4$  V,  $I_t = 0.2$  nA,  $T_s = 78$  K; fast scan direction is  $18^\circ$  clockwise from horizontal. **b)** Fourier transform of the image in panel **a**. The *grid* shows the primitive unit cell of the OH overlayer; the *circles* mark the substrate spots. The overlayer exhibits a  $c(2 \times 6)$  periodicity corresponding to a coverage of 0.58 ML ( $7/6 \text{ H}_2\text{O}$  per unit cell).

### The $(1 \times 3)$ overlayer

Exposing the  $c(2 \times 6)$  overlayer to an additional  $\text{H}_2\text{O}$  dose of 0.15 L at 100 K, and annealing at RT for 1 h results in a surface covered by domains of a  $(1 \times 3)$  overlayer and a mixture of the bright-dark features and single water monomers, see Figure 4.6a.

The  $(1 \times 3)$  overlayer corresponds to 0.67 ML, and according to DFT calculations,<sup>87</sup> consists of dimers of dissociated water in the most favourable configurations along  $[010]$ , i.e. B1O1 and B2O2 (Figure 4.6b), or B2O2 and B1O1, with one unoccupied bridge site between them. The bright-dark features are separated by one unoccupied bridge site from either another bright-dark feature or a water monomer (along  $[010]$ ). Counting the number of bright-dark features and water monomers in a large-scale STM image (Figure 4.7a) gives an average 0.60 ML coverage for the mixture.

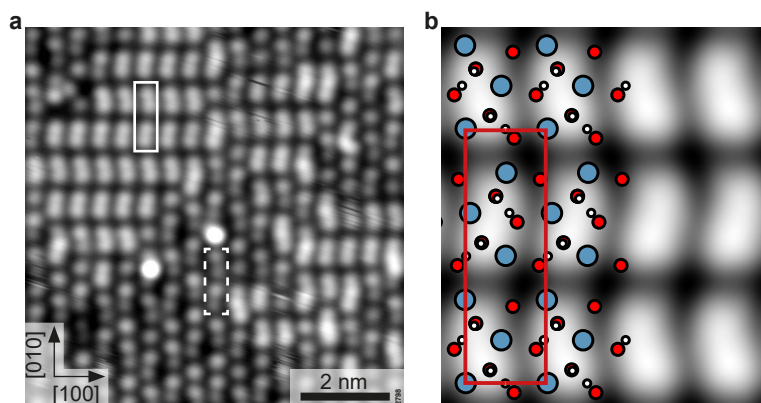


**Figure 4.6 | The  $(1 \times 3)$  overlayer.** **a)** STM image after exposing the  $c(2 \times 6)$  overlayer to 0.15 L at 100 K and subsequent annealing at RT for 1 h. The surface is covered by domains of a  $(1 \times 3)$  overlayer (*solid box*) as well as a mixture of bright-dark features (*dashed box*) and water monomers. STM parameters:  $V_s = -0.8$  V,  $I_t = 0.1$  nA,  $T_s = 78$  K; fast scan direction is  $18.5^\circ$  clockwise from horizontal. **b)** DFT model<sup>87</sup> and STM simulation of the  $(1 \times 3)$  overlayer, corresponding to 0.67 ML; Ca – blue, O – red, H – white. Along  $[010]$  pairs of dissociated water in the most favorable configurations are formed, i.e., B1O1 and B2O2 (shown here), or B2O2 and B1O1, with one unoccupied bridge site between them. The *box* marks the superstructure cell, which spans three substrate unit cells in  $[010]$  direction.

Further increasing the water coverage by increasing the initial dose to the  $c(2 \times 6)$  overlayer and decreasing the annealing time results in the  $(1 \times 3)$  domains covering first an increasing part and then almost the whole surface, see Figure 4.7a-c. The experimental annealing procedure (i.e., placing the sample into a RT environment for 15 min) leaves considerable uncertainty regarding the exact temperature that was reached; probably it was somewhere between 160 K and 300 K.

### The $(1 \times 1)$ overlayer

Increasing the coverage further by dosing 0.4 L to the  $(1 \times 3)$  covered surface leads to bright, slightly undulating lines along  $[010]$  with almost no gaps, see Figure 4.7d.

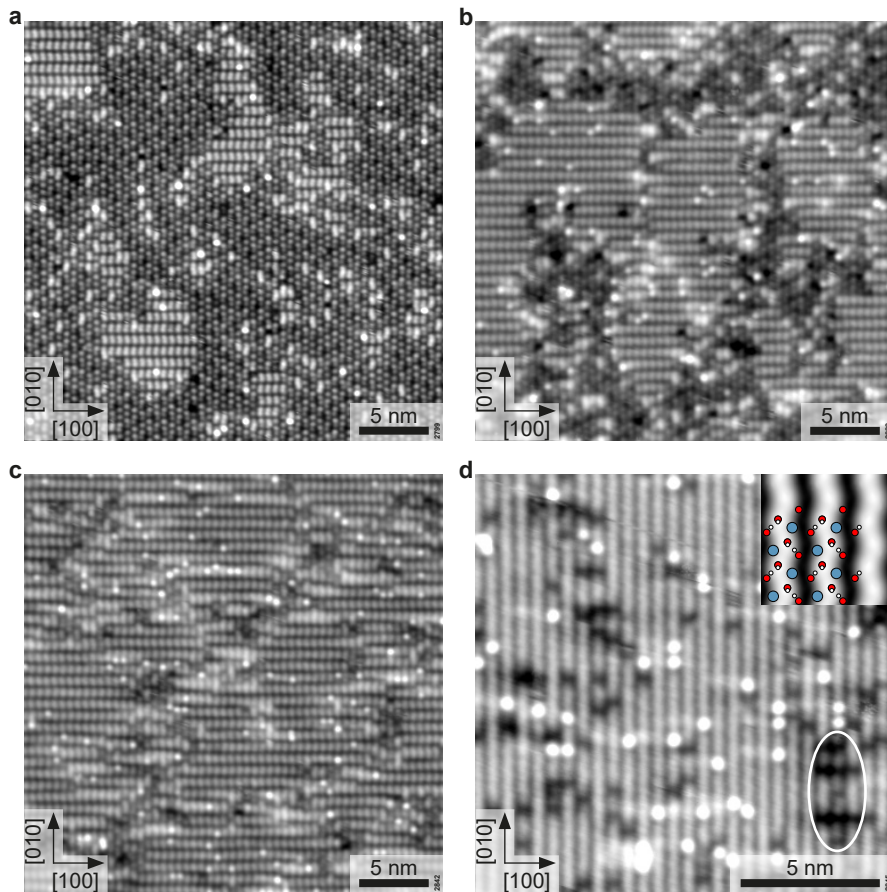


**Figure 4.7 | Effect of increasing water dose and the  $(1 \times 1)$  overlayer.** a-c) STM images after exposing the  $c(2 \times 6)$  overlayer to increasing  $\text{H}_2\text{O}$  doses at 105 K and subsequent annealing at RT for decreasing times ( $t$ ). **a)** 0.15 L and  $t = 1$  h. **b)** 0.5 L and  $t = 30$  min. **c)** 1.0 L and  $t = 15$  min. **d)** STM image after dosing 0.4 L  $\text{H}_2\text{O}$  to the sample in panel **c** without subsequent annealing. Bright, undulating lines in [010] direction cover the sample, showing only a few gaps, where the  $(1 \times 3)$  structure is still visible (*oval*). The single, bright dots are unidentified adsorbates ( $\approx 0.03$  ML) from the residual gas. The inset shows the DFT model<sup>87</sup> and STM simulation ( $V_s = +0.8$  V) of the  $(1 \times 1)$  overlayer. STM parameters:  $V_s = -0.8$  V,  $I_t = 0.1$  nA,  $T_s = 78$  K; fast scan direction is  $18^\circ$  clockwise from horizontal.

The continuous, undulating lines agree well with the STM simulation for the  $(1 \times 1)$  overlayer, i.e. the full monolayer with all  $O_{\text{surf}}$  atoms hydroxylated. Both equivalent adsorption sites (B1O1 and B2O2) in the unit cell are occupied, i.e., all  $O_{\text{surf}}$  are hydroxylated. Dosing more water to the fully hydroxylated surface without annealing leads to diffuse, white patches in STM that are assigned to molecular water moving under the tip, see Figure 4.8a; the presence of molecular water is confirmed in XPS, see Section 4.2.3. The adsorption energy and nominal coverage for the different overlayers are summarized in Table 4.3.

Configuration	$E_{\text{ads}}$ [eV]	Slab size	H <sub>2</sub> O molecules	Coverage [ML]
$(2 \times 1)$	1.62	$(2 \times 1)$	2	0.5
$c(2 \times 6)$	-	-	-	0.58
$(1 \times 3)$	1.59	$(1 \times 3)$	4	0.67
$(1 \times 1)$	1.48	$(1 \times 1)$	2	1.0
Molecular	0.78	$(1 \times 1)$	1	0.5

**Table 4.3 | Calculated adsorption energy<sup>87</sup> and nominal coverage for the OH overlayers.** No model was found for the  $c(2 \times 6)$  overlayer.

### Gradual desorption

In an attempt to desorb the molecular water, the sample was taken out of the STM head and placed in an ordinary slot of the sample storage (not the cooling stage in slot 1) in the LT-STM thus warming the sample. While the sample was warming up, the chamber pressure (base pressure of  $5 \times 10^{-12}$  mbar) increased and reached its maximum after 0.5 min at  $7 \times 10^{-11}$  mbar, see Table 4.4. After a total time of 1.5 min in the sample storage the sample was put back in the STM head. This annealing procedure was repeated 3 times with increasing annealing times. After the first annealing, Figure 4.8b shows that the molecular water was desorbed and the  $(1 \times 1)$  overlayer with very few gaps remained. After annealing for 3 min the  $(1 \times 1)$  overlayer exhibits more gaps (Figure 4.8c). Annealing for 6 min resulted in a break-up of the  $(1 \times 1)$  layer into short lines of varying length and a few patches of the  $(1 \times 3)$  overlayer (Figure 4.8d). Annealing for 9 min led to a mostly  $(1 \times 3)$  overlayer covered surface with only a few longer lines consisting of three or more dissociated monomers in a row along  $[010]$ .

It is noteworthy that even during the final annealing the desorbing water could be detected with the ion gauge, given the rather tiny sample size in the order of a

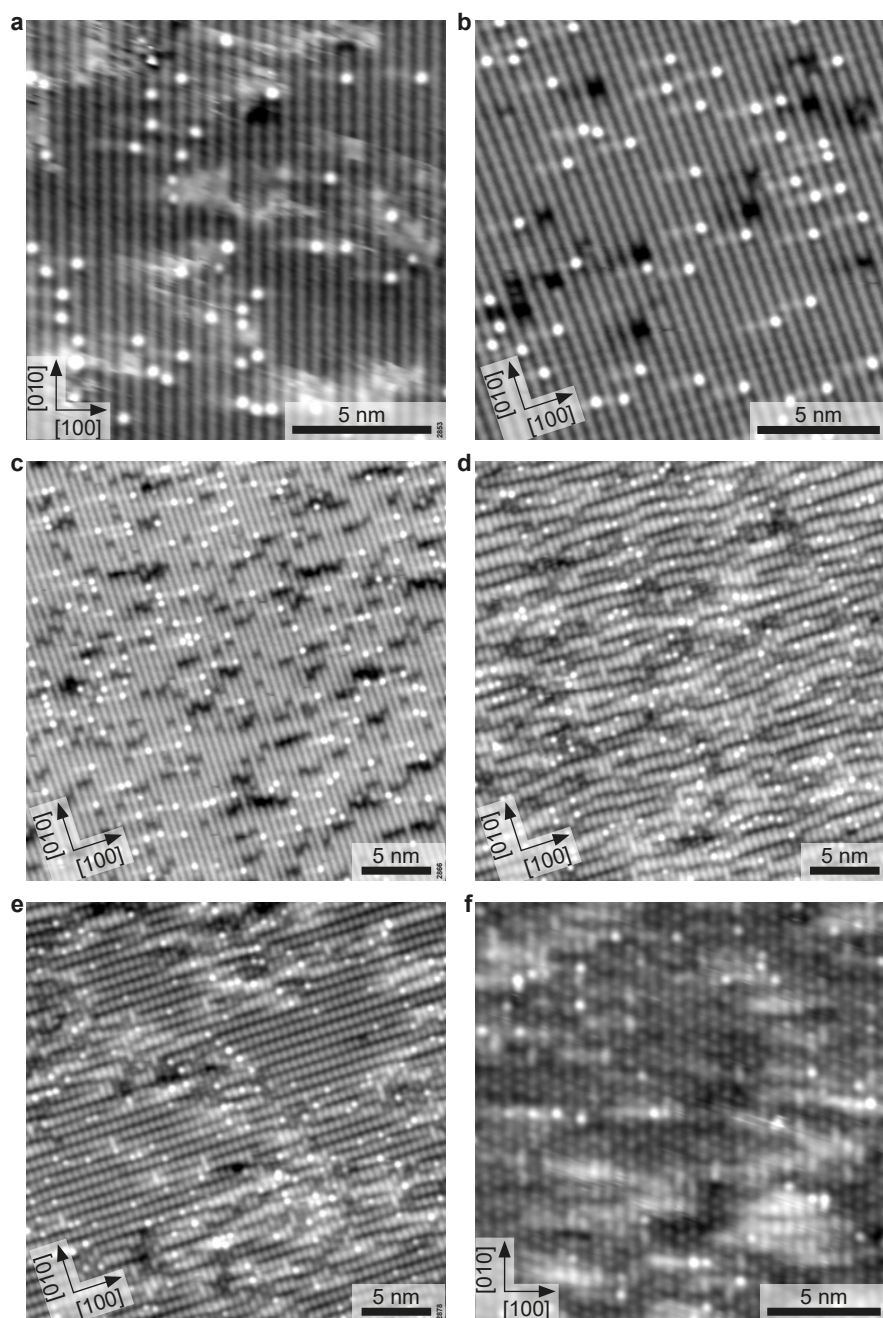


**Figure 4.8 | The (1 × 1) overlayer, molecular water and gradual desorption.** a) After dosing 0.75 L H<sub>2</sub>O to the sample in Figure 4.7d. The diffuse, white patches are assigned to molecular water. b-e) After annealing for 1.5 min, 3 min, 6 min and 9 min, respectively (see main text for detailed procedure). f) After annealing the sample in Figure 4.7c at RT for 3 h. STM parameters:  $V_s = -0.8$  V,  $I_t = 0.1$  nA,  $T_s = 78$  K; fast scan direction in panel a and f is 18° clockwise from horizontal.

Annealing time [min]	Maximum pressure [mbar]	Maximum after [min]	STM image
1.5	$7.0 \times 10^{-11}$	1	Figure 4.8b
3	$7.4 \times 10^{-12}$	1.5	Figure 4.8c
6	$6.3 \times 10^{-12}$	4	Figure 4.8d
9	$5.8 \times 10^{-12}$	4.5	Figure 4.8e

**Table 4.4 | Gradual water desorption.** Maximum chamber pressures and times measured during the gradual desorption of the OH-overlayers. The base pressure of the chamber was  $5.0 \times 10^{-12}$  mbar. See main text for description of annealing procedure.

few mm<sup>2</sup>. The detection of such small chamber pressure increases ( $8 \times 10^{-13}$  mbar) requires of course that no wobble stick movements or other activities that could disturb the settling of the chamber pressure are performed after the sample was taken out of the STM head.

### Long annealing at RT

Even after annealing an OH-covered sample at RT for several hours, water is still adsorbed. Figure 4.8f shows the sample in Figure 4.7c that is almost fully covered by the (1×3) overlayer after annealing for 3 h at RT. Only a few (1×3) overlayer patches remain while the sample is mainly covered by a mixture of the (2×1) OH overlayer and bright-dark features. A different OH-covered sample annealed at 330 K for 20 min was still covered by patches of the (2×1) OH overlayer, see Figure 4.9. A rough estimate for the adsorption energy based on the desorption rates and temperatures is < 1 eV to 1.3 eV. Annealing at higher temperatures was not possible because of the epoxy glue that was used to mount the sample.

### 4.2.3 X-ray photoelectron spectroscopy

Increasing coverages of water are followed in the O1s XPS, see Figure 4.10. The pristine surface exhibits an asymmetric peak at 529.2 eV binding energy (BE), broadened towards the high BE side. For all annealed water structures observed by STM (c(2×6), (1×3) and (1×1)) the spectrum shows a shoulder between 530.0 eV and 531.0 eV BE; i.e. roughly 1.5 eV above the as-cleaved O peak. This fits well to the calculated BE shifts of 1.57 eV and 1.23 eV for surface hydroxyls in the (1×3) and (1×1) overlayer, respectively, see Table A.2. Only after saturating the surface with hydroxyls and dosing additional water at 105 K without annealing, a peak at 533.1 eV

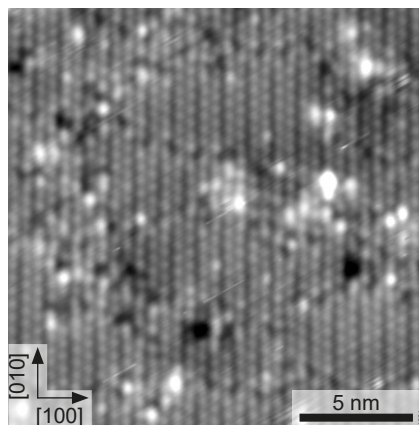


**Figure 4.9** | A different OH-covered sample after annealing at 330 K. After annealing at 330 K for 20 min the sample is still covered by patches of the  $(2 \times 1)$  overlayer.  $V_s = -0.8$  V,  $I_t = 0.1$  nA,  $T_s = 78$  K; fast scan direction is  $29^\circ$  clockwise from horizontal.

BE is observed; i.e. 3.9 eV above the bulk oxygen peak. This fits well to the calculated BE shift of 3.79 eV for molecular water.<sup>87</sup> Therefore, in agreement with the DFT results, the shoulder and the peak are attributed to dissociated and molecular water, respectively.

The asymmetric peak of the pristine surface is explained by DFT calculations:<sup>88</sup> the O1s core level for the oxygen atoms in the CaO plane is shifted to 0.7 eV higher BE compared to the RuO<sub>2</sub> planes, which serve as DFT reference. Keeping in mind that the higher BE O1s signal of the CaO planes contributes less to the total O1s intensity, the observation of only one asymmetric peak in the experiment is attributed to the limited resolution of the experimental setup.

#### 4.2.4 Oxygen vacancies

Oxygen vacancies ( $V_O$ ) were investigated as they are a common theme in metal-oxides and especially important for mixed ionic and electronic conductors, serving as electrodes in solid oxide fuel cells.<sup>2,3</sup>  $V_O$ s do not form spontaneously when cleaving the samples; here they were instead created by irradiating the clean surface by 1 keV electrons,<sup>30,108</sup> see Figure 4.11a,b. At low temperatures no interaction was observed between the water and the  $V_O$  (Figure 4.11c), but after annealing to room temperature bright, double-lobed features are observed that sit centred on the bright substrate lines (Figure 4.11d). These features are assigned to two neighbouring surface hydroxyls, formed by the dissociation of water that filled the  $V_O$ . The adsorption

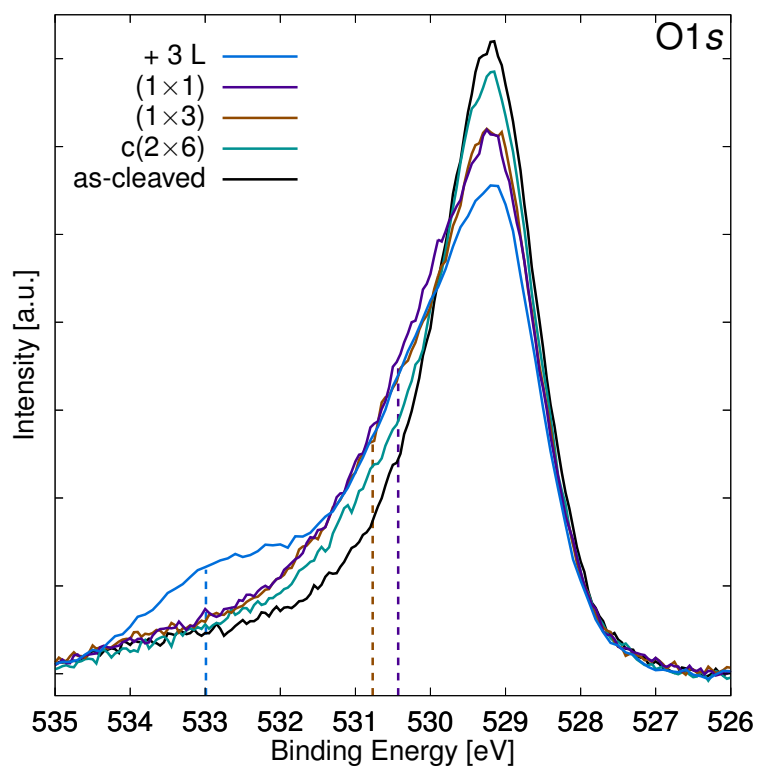


**Figure 4.10 | O1s XPS spectra of the as-cleaved surface and OH-overlayers.** Coverages up to and including the full monolayer lead to a shoulder between 530.0 eV and 531.0 eV BE for the  $c(2 \times 6)$ ,  $(1 \times 3)$  and  $(1 \times 1)$  overlayer (full monolayer). Exposing the full monolayer to water at 105 K leads to a peak at 533.1 eV BE (+3L). In agreement with DFT calculations<sup>87</sup> (dashed vertical lines, see Table A.2), the shoulder and the peak are assigned to hydroxyls and molecular water, respectively. (Mg  $K\alpha$ ,  $T_{\text{sample}} = 110$  K.)



energy for dissociative adsorption at an oxygen vacancy is 2.41 eV according to DFT calculations.<sup>87</sup> The hydrogen can be desorbed by scanning with a high positive bias voltage<sup>109</sup> leaving behind the pristine surface (Figure 4.11e,f).

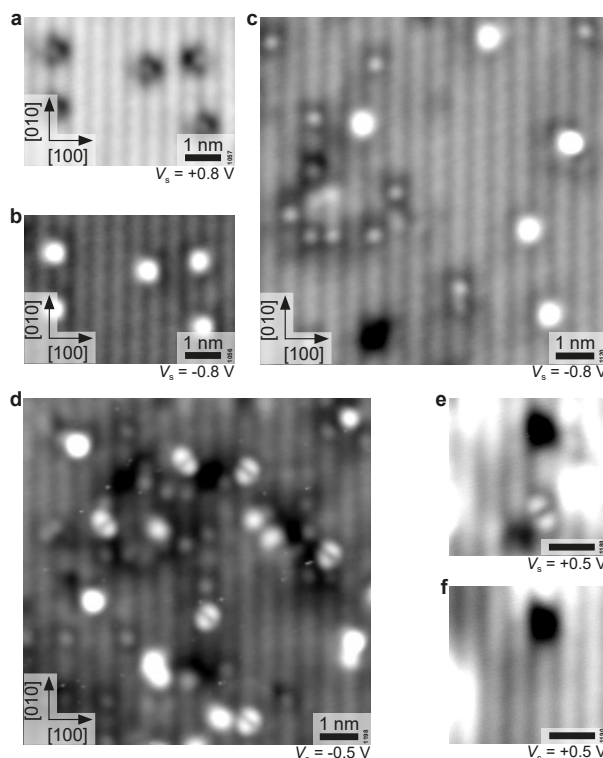


**Figure 4.11 | Oxygen vacancies and the interaction with water on  $\text{Ca}_3\text{Ru}_2\text{O}_7(001)$ .** **a)** Empty and **b)** filled-states STM image after irradiation with 1 keV electrons at 105 K. In empty states the oxygen vacancy ( $V_{\text{O}}$ ) appears as a small, bright dot on the dark substrate line with a one-sided, dark patch extending into the bright substrate line. In filled states the  $V_{\text{O}}$  appears as a large, bright dot on the dark substrate line. **c)** Filled-states STM image after exposure to 0.05 L  $\text{H}_2\text{O}$ . **d)** Different area than in panel c and after annealing at room temperature for 50 min. The bright, double-lobed features are attributed to neighbouring surface hydroxyls, formed by the dissociation of water that filled the  $V_{\text{O}}$ . **e)** Large-scale STM image of a double-lobed feature next to unidentified adsorbates. **f)** Same area as in panel e, but after scanning the area with a bias of  $V_s = +4.5$  V. The double-lobed feature has desorbed and at its former location the pristine surface is left behind. STM parameters:  $I_t = 0.1$  nA,  $T_s = 78$  K,  $V_{\text{sample}}$ : see panels; fast scan direction is  $16^\circ$  (a-d) and  $18^\circ$  (e-f) anticlockwise from horizontal.

### 4.3 Discussion

On the basis of the XPS measurements and DFT calculations<sup>87</sup> it is clear that water adsorbs dissociatively on  $\text{Ca}_3\text{Ru}_2\text{O}_7$ . STM images show ordering of the  $(\text{OH})_{\text{ads}}$  in

agreement with the calculated adsorption models. Interestingly, the – at first sight rather complex – evolution of ordered structures can be rationalized by considering the rotation and tilt of the O octahedra. According to DFT<sup>87</sup>, in the most preferred configuration B1O1 (Figure 4.2) the tilt of the hydroxylated octahedron increases from 12.9° to 16.3° towards its natural tilting direction when the water dissociates at this site. The O-Ru-O angle changes minimally from 178.2° to 177.6°. The O-O distances between the (OH)<sub>ads</sub> and the adjacent surface oxygen atoms O1 and O2 are 2.57 Å and 2.98 Å, respectively. The weaker adsorption energies for the configurations B2O1 and B3O1 correlate foremost with the forced tilting of the octahedron that is necessary to accommodate the dissociation fragments at similar O-O distances; in both cases this tilt goes against the natural direction and distorts the O-Ru-O angles (see Table 4.2 and Figure 4.3).

### Evolution of the OH overlayers

With the largest bridge site to O<sub>surf</sub> distance (*i.e.*, B1-O1 and B2-O2) providing the highest adsorption energy, only these sites are filled. At low coverages every other bridge site along [010] is left out, leading to a local (2 × 1) ordering of individual hydroxide pairs (Figure 4.1). As the coverage increases, the (2 × 1) OH overlayer is compressed along [010] and forms the c(2 × 6) OH overlayer with 7 (OH)<sub>ads</sub> on 6 unit cells (0.58 ML). The undulation probably arises from the inequivalent positions of the (OH)<sub>ads</sub> with respect to the bridge site due to the compression. Additionally the protons of the (OH)<sub>ads</sub> may be oriented differently depending on the exact positions of the oxygens.

Further increasing coverage leads to fragments of the dissociated water locating at neighbouring bridge sites in the (1 × 3) OH overlayer and the bright-dark features (Figure 4.6). The bright-dark feature is suggested to be a dissociated water dimer in two adjacent bridge sites along [010], eventually leading to a full (1 × 3) OH overlayer. However, in the precursor bright-dark structure the (OH)<sub>ads</sub> that is oriented towards the [0 $\bar{1}$ 0] direction appears darker. A possible explanation is the inequivalence of the bridge sites available for the second water once the first water has adsorbed and dissociated. In one case the (OH)<sub>ads</sub> is next to the unoccupied site, in the other case the O<sub>surf</sub>H.

The ratio of surface covered by the (1 × 3) OH overlayer to surface covered by the mixture of bright-dark features and water monomers depends on the overall wa-

ter coverage. The more water, the more surface is covered by the  $(1 \times 3)$  OH overlayer (Figure 4.7). This trend agrees with the  $(1 \times 3)$  OH overlayer being equivalent to 0.67 ML and the mixture of bright-dark features and monomers being equivalent to roughly 0.60 ML.

Dosing water to the  $(1 \times 3)$  overlayer resulted in formation of the  $(1 \times 1)$  overlayer where all surface oxygen atoms are hydroxylated. Only beyond that point the adsorption of molecular water was observed in STM and XPS.

The skipping of available sites and the monotonic decrease in adsorption energy as the coverage increases (Table 4.3) suggests that the ordering is governed by electrostatic repulsion. On BaO(001) the electrostatic repulsion between  $(\text{OH})_{\text{ads}}$  and  $\text{O}_{\text{surf}}\text{H}$  was shown to be screened by the  $\text{Ba}^{2+}$  cations.<sup>110</sup> However, the polarizability<sup>111</sup> of  $\text{Ca}^{2+}$  is four times lower than of  $\text{Ba}^{2+}$ , and  $\text{Ca}_3\text{Ru}_2\text{O}_7(001)$  is less symmetric than BaO(001) thus the screening may be less effective.

### Gradual desorption

The molecular water and the OH-overlayers could be gradually desorbed in a controlled manner (Table 4.4 and Figure 4.8). The clearly increasing times until the maximum pressures were reached and the accompanying gradual decrease in coverage observed by STM indicate that the sample reached higher and higher temperatures for increasing annealing times. Therefore the most weakly bound molecular water desorbed first (1.5 min annealing), followed by water that was adsorbed as dissociated monomer in the gaps of the  $(1 \times 1)$  overlayer in Figure 4.8c (3 min annealing). Interestingly, the majority of gaps is half a unit cell wide, i.e., only one dissociated monomer is missing. The maximum pressure observed during the following annealing (6 min) was observed after 4 min (*i.e.*, at higher sample temperature). Either the monomers in said gaps were more weakly bound than the other monomers, or the created gaps allowed for relaxations of the other monomers which led to a slightly increased adsorption energy. The latter is more likely. The complete break-up of the  $(1 \times 1)$  layer followed during the 6 min annealing, see Figure 4.8d. The maximum pressure in the final annealing (9 min) occurred virtually after the same time as in the previous annealing, indicating that the desorption energy of the respective monomers was equal. The gradual desorption is in agreement with the monotonic decrease in adsorption energy as the coverage increases (Table 4.3).

### Comparison to related oxides

It is instructive to compare the adsorption behaviour on Ca<sub>3</sub>Ru<sub>2</sub>O<sub>7</sub> to the related strontium ruthenate perovskite and the binary alkaline-earth oxide CaO, where the surface is much more symmetric and where detailed surface measurements are available. The dissociation into an (OH)<sub>ads</sub> fragment, adsorbed on a cation bridge site, and into a proton, adsorbed on a neighbouring surface oxygen, was observed on the SrO-terminated surface of Sr<sub>n+1</sub>Ru<sub>n</sub>O<sub>3n+1</sub> ( $n = 1, 2$ ) (see Chapter 5).<sup>89</sup> There the oxygen octahedra are not tilted with respect to the [001] direction, hence the surface oxygen sublattice is square and all bridge sites are equally spaced from the O<sub>surf</sub>. The (OH)<sub>ads</sub> fragment hops between the four equivalent cation bridge sites around the O<sub>surf</sub>H fragment at liquid-nitrogen temperature. On Ca<sub>3</sub>Ru<sub>2</sub>O<sub>7</sub> no hopping of the (OH)<sub>ads</sub> was observed. This agrees with one of the bridge sites surrounding the O<sub>surf</sub> being clearly preferred for adsorption (Table 4.2). At low coverages dimers are not formed, but every other bridge site along the [010] direction is unoccupied as discussed above. In contrast, on Sr<sub>n+1</sub>Ru<sub>n</sub>O<sub>3n+1</sub> stable dimers in adjacent Sr-Sr bridge sites are preferentially formed, evolving into one-dimensional chains.<sup>89</sup>

On the binary alkaline-earth oxide CaO(001), dissociation of the water monomer was predicted with adsorption energies around 0.9 eV.<sup>51,52</sup> Experimentally, mixed dissociative and molecular adsorption of water was observed at very low coverages on CaO(001).<sup>54</sup> The exclusively dissociative adsorption and the higher adsorption energy of 1.64 eV on Ca<sub>3</sub>Ru<sub>2</sub>O<sub>7</sub> is in agreement with the reported preference for dissociative adsorption for an increased lattice constant,<sup>51</sup> as the Ca-Ca distance on Ca<sub>3</sub>Ru<sub>2</sub>O<sub>7</sub> is 10.2 % larger than on CaO(001). A transformation into a disordered state with partially solvated Ca<sup>2+</sup> ions was reported on CaO after saturating the surface at room temperature.<sup>55</sup> No signs of such a transformation of the CaO surface layer were observed on Ca<sub>3</sub>Ru<sub>2</sub>O<sub>7</sub> after saturating the surface at 110 K and annealing at room temperature (see Figure 4.8).

### Oxygen vacancies

It is interesting that O<sub>surf</sub>H hydroxyl pairs that form when water dissociates at an oxygen vacancy and fills it also show preferential arrangement. Here such V<sub>O</sub>s were not observed on the as-cleaved surface but artificially created by electron bombardment. After dosing water at 105 K and annealing to room temperature bright, double-lobed features formed (Figure 4.11). The two lobes always span a bright sub-

strate line, indicating that the split-off proton prefers to adsorb on the  $O_{\text{surf}}$  that has the larger distance (4.5 Å compared to 3.2 Å) to the surface hydroxyl that formed at the location of the healed  $V_{\text{O}}$ .

## 4.4 Summary

Exposure of the  $\text{Ca}_3\text{Ru}_2\text{O}_7(001)$  surface to  $\text{H}_2\text{O}$  at 105 K results in dissociative adsorption. STM shows the  $(\text{OH})_{\text{ads}}$  of the dissociated monomer as bright spot on the bright substrate line. Increasing  $\text{H}_2\text{O}$  doses at 105 K and annealing to room temperature leads to the formation of ordered OH-overlayers:  $(2 \times 1)$ ,  $c(2 \times 6)$ ,  $(1 \times 3)$  and  $(1 \times 1)$ . Dosing additional water to the fully hydroxylated surface leads to adsorption of molecular water that appears as diffuse, white patches in STM. The molecular water and the OH-overlayers could be gradually desorbed by annealing to gradually increasing temperatures. Annealing a OH-covered sample at 330 K is not sufficient to desorb the  $(2 \times 1)$  OH-overlayer. The dissociated state of the water in the OH-overlayers was confirmed by XPS. Increasing coverage results in a  $\text{O}1s$  shoulder between 530.0 eV and 531.0 eV BE; i.e. roughly 1.5 eV above the  $\text{O}1s$  peak of the pristine surface. The dissociation of water at artificially created  $V_{\text{O}}$ s resulted in the formation of two neighbouring surface hydroxyls and healing of the  $V_{\text{O}}$ .

Accompanying DFT calculations<sup>87,88</sup> show that the  $(\text{OH})_{\text{ads}}$  group adsorbs on a Ca-Ca bridge site and that the split-off H is transferred to a neighboring  $O_{\text{surf}}$ ; adsorption models and STM simulations of the OH-overlayers are provided that are in accordance with the experimental findings.



# Chapter 5

## H<sub>2</sub>O Adsorption on Sr<sub>2</sub>RuO<sub>4</sub>

This chapter is based on an article published in *Nature Materials* **15**, 450–455 (2016), ref. [89]. However, this chapter contains additional information not available in the published article.

### 5.1 Introduction

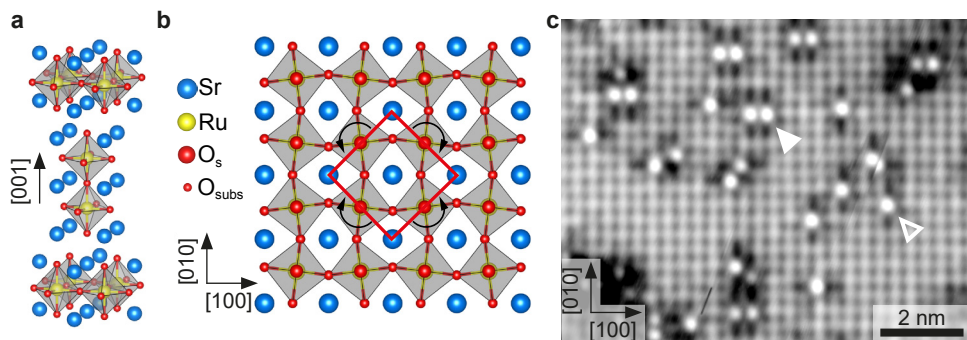
The adsorption of water on Sr<sub>2</sub>RuO<sub>4</sub>(001) and Sr<sub>3</sub>Ru<sub>2</sub>O<sub>7</sub>(001) was investigated by Bernhard Stöger as part of his PhD thesis.<sup>13</sup> A few results thereof are briefly summarized, before describing the work done in the course of the present thesis.

#### The pristine surface

Sr<sub>2</sub>RuO<sub>4</sub> and Sr<sub>3</sub>Ru<sub>2</sub>O<sub>7</sub> are the  $n = 1$  and  $n = 2$  member of the Ruddlesden-Popper series Sr <sub>$n+1$</sub> Ru <sub>$n$</sub> O <sub>$3n+1$</sub> . The main structural difference when compared to the calcium ruthenate series is the larger ionic radius of the A-site ion ( $r_{\text{Sr}^{2+}} = 1.44 \text{ \AA}$ ,  $r_{\text{Ca}^{2+}} = 1.34 \text{ \AA}$ )<sup>112</sup> and that the RuO<sub>6</sub> octahedra are not tilted with respect to the  $c$ -axis, see Figure 5.1a,b. The (001) surfaces of Sr<sub>2</sub>RuO<sub>4</sub> and Sr<sub>3</sub>Ru<sub>2</sub>O<sub>7</sub> both exhibit a very similar  $c(2 \times 2)$  surface unit cell due to an alternating rotation of the RuO<sub>6</sub> octahedra in the top surface layer by approximately 8°.<sup>13</sup>

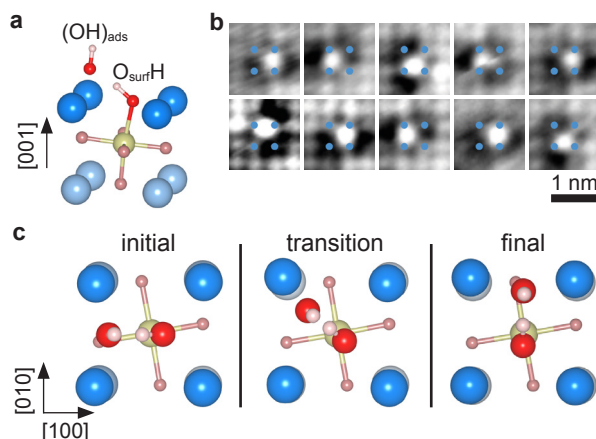
#### Water monomer

Figure 5.1c shows the Sr<sub>3</sub>Ru<sub>2</sub>O<sub>7</sub>(001) surface after a small amount of H<sub>2</sub>O was dosed at 115 K. Water monomers appear as intense, isolated spots accompanied by a dark shadow extending either in [100] or [010] direction; some adsorb next to each other as dimers. According to DFT calculations<sup>87</sup> the bright spots correspond to



**Figure 5.1 | The  $Sr_3Ru_2O_7$  structure and low dose of water.** **a)** Unit cell of  $Sr_3Ru_2O_7$ . **b)** Top view of the  $Sr_3Ru_2O_7(001)$  surface. The alternating rotation (*arrows*) of the  $RuO_6$  octahedra results in a  $c(2 \times 2)$  surface unit cell (*red square*). **c)** STM image of  $Sr_2RuO_4(001)$  after dosing 0.05 L of  $H_2O$  at 115 K. The Sr surface atoms appear as bright spots; water appears as intense, bright spots. Monomers (*open triangle*) and Dimers (*full triangle*) are observed. STM parameters:  $V_s = +0.05$  V,  $I_t = 0.15$  nA,  $T_s = 78$  K; fast scan direction is  $69^\circ$  counterclockwise from horizontal.

the  $(OH)_{ads}$  of dissociated water. The  $(OH)_{ads}$  is adsorbed on a Sr-Sr bridge and the split-off H is transferred to a nearby surface oxygen atom ( $O_{surf}$ ) forming a surface hydroxyl ( $O_{surf}H$ ), see model in Figure 5.2a.



**Figure 5.2 | The dissociated water monomer.** **a)** DFT model<sup>87</sup> of the dissociated water monomer. **b)** Sequence of STM images showing the hopping of the  $(OH)_{ads}$ . **c)** DFT model of the hopping process;  $E_{act} = 171$  meV.

When recording sequential STM images of the same monomer, hopping of the bright spot (*i.e.*, the  $(OH)_{ads}$ ) between four Sr-Sr bridge sites is observed, see Figure 5.2b. The  $(OH)_{ads}$  is always observed at one of the same four Sr-Sr bridge sites. According to DFT calculations<sup>87</sup> the  $(OH)_{ads}$  is bound by a hydrogen bond to its respective  $O_{surf}H$  that is located in the middle of the four bridge sites, thus hindering



the  $(\text{OH})_{\text{ads}}$  to diffuse anywhere else. The hopping between two adjacent Sr-Sr bridge sites was modelled by a transition state where the  $(\text{OH})_{\text{ads}}$  is located directly between the  $\text{O}_{\text{surf}}\text{H}$  and the Sr that is part of both Sr-Sr bridge sites, see Figure 5.2c. The calculated<sup>87</sup> activation energy for the hopping is 171 meV.

The experimentally observed hopping of the  $(\text{OH})_{\text{ads}}$  confirms the predicted dynamic behaviour of dissociated water by *ab initio* molecular dynamics calculations on the (001) surfaces of alkaline-earth oxides.<sup>52</sup>

## 5.2 Results

### 5.2.1 Activation energy measurement of the $(\text{OH})_{\text{ads}}$ hopping

#### Model

The hopping of the  $(\text{OH})_{\text{ads}}$  of the water monomer (see Figure 5.2) was modelled as one-dimensional, thermally activated random walk.<sup>113</sup> The hopping rate,  $R$ , varies with absolute temperature  $T$  as

$$R = \tau^{-1} = \nu \exp\left(-\frac{E_{\text{act}}}{kT}\right), \quad (5.1)$$

where  $\nu$  is an attempt frequency,  $E_{\text{act}}$  is the activation energy and  $\tau$  is the average lifetime; lifetime is defined as the time between two hops (of the same  $(\text{OH})_{\text{ads}}$ ). To obtain  $E_{\text{act}}$ , the average lifetime for different temperatures was measured by analyzing the  $(\text{OH})_{\text{ads}}$  hopping in STM movies.

To motivate the analysis method, it is noted that for constant  $T$  the average hopping rate,  $R$ , is constant, and that the occurrence of the next hop is independent from the last hop, qualifying the hopping as a Poisson process. Therefore the lifetimes,  $t_i$ , of the  $(\text{OH})_{\text{ads}}$  are exponentially distributed according to

$$N(t_i) \propto \exp\left(-\frac{t_i}{\tau}\right). \quad (5.2)$$

Determining the lifetime distribution,  $N(t_i)$ , and fitting to Equation (5.2) gives the average lifetime for the particular temperature. When the number of lifetimes was

too small ( $< 100$ ) for a reasonable fit, the hopping rate was calculated according to

$$R = \tau^{-1} = \frac{1}{t_f} \frac{\sum_{j=1}^{n-1} m_j}{\sum_{j=1}^{n-1} a_j}, \quad (5.3)$$

where  $a_j$  is the number of evaluated  $(\text{OH})_{\text{ads}}$  in frame  $j$ ,  $m_j$  is the number of observed hops between frame  $j$  and  $j + 1$ ,  $t_f$  is the acquisition time for a single frame and  $n$  is the total number of frames. The standard error of the hopping rate is then given as

$$\sigma_R = \frac{1}{t_f} \frac{\sqrt{\sum_{j=1}^{n-1} m_j}}{\sum_{j=1}^{n-1} a_j}. \quad (5.4)$$

## Experimental

A Sr<sub>2</sub>RuO<sub>4</sub> sample was cleaved at 107 K in the analysis chamber of the LT-STM and transferred to the STM head (78 K) to confirm the surface cleanliness. Then the sample was transferred on the cold manipulator (110 K) to the preparation chamber where 0.01 L H<sub>2</sub>O were dosed ( $p_{\text{H}_2\text{O}} = 1.0 \times 10^{-10}$  mbar for 133 s). The sample was transferred back to the STM head.

For the STM movies the temperature of the cryostat of the STM was lowered by evacuating the volume above the LN<sub>2</sub> by a roughing pump. Constant pumping decreased the temperature of the cryostat to 53 K within 12 hours. After the pump was switched off (and the pumped volume kept sealed) the temperature increased slowly with an approximate rate of 0.5 K/h, see Figure A.1. Decoupling the STM head from the cryostat sufficiently slowed temperature rate at the STM head to approximately 0.2 K/h. The mean of the temperatures at the start and the end of the STM movie was taken as temperature for the measured hopping rate. The scan speed was chosen sufficiently fast so that no double hops between two consecutive images were observed. All STM images were recorded with 0.1 nA tunnelling current and +0.2 V sample bias voltage. Movies 4-8 were recorded with an unusual tip condition that showed the  $(\text{OH})_{\text{ads}}$  as dark feature instead of the usual, bright spot. The movies are available in the [Electronic Supplement](#).

## Analysis

$(\text{OH})_{\text{ads}}$  adsorbed next to a surface defect or close to another  $\text{OH}_{\text{ads}}$  were ignored in the analysis; see Figure A.2 for which  $(\text{OH})_{\text{ads}}$  in movies M2 to M6 were ignored

(considered) in the analysis. During movie M1 the number of evaluated  $\text{OH}_{\text{ads}}$  groups changed because of image drift. Table A.1 lists the observed number of hops and the evaluated number of  $\text{OH}_{\text{ads}}$  groups for every frame of movie M1.

The lifetime distribution of the  $(\text{OH})_{\text{ads}}$  of movies M3 to M6 and fit to Equation (5.2) are shown in Figure 5.3. Note that with increasing number of counted lifetimes the measured distribution comes closer and closer to an exponential distribution. Movies M1 and M2 had too few lifetimes to produce a meaningful distribution, therefore the average lifetime was derived according to Equation (5.3). The recording of a higher number of lifetimes at the lower temperatures (65 to 69 K would have required a longer measurement time, but the temperature increase during such a long time would have been too large. Table 5.1 shows the acquisition details of the recorded movies and the resulting average lifetimes.

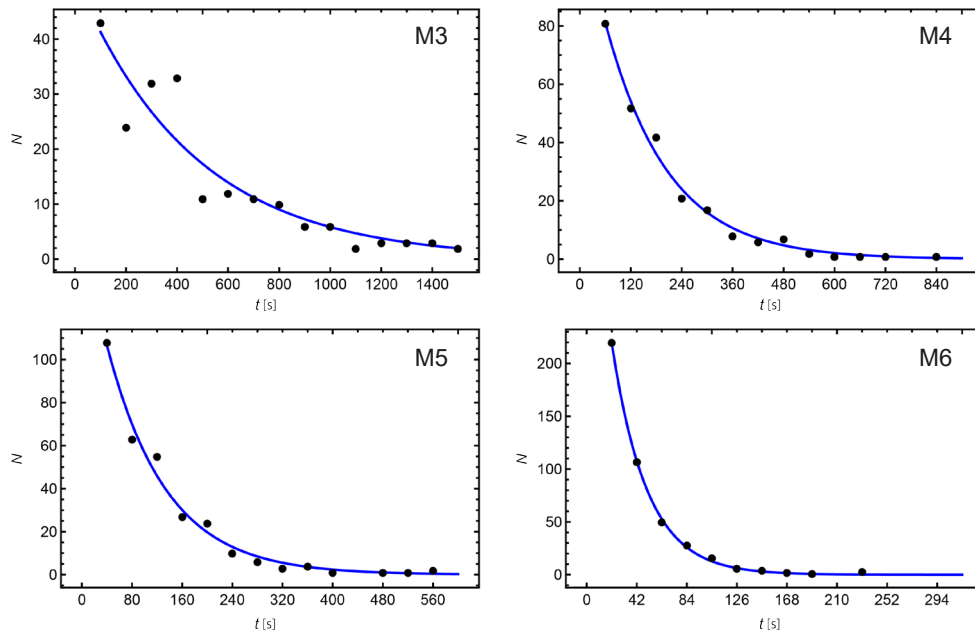


**Figure 5.3 | Lifetime distributions of the STM movies M3 to M6.** Counted lifetimes (*dots*) and exponential fit (*line*) according to Equation (5.2). Note the different time scales and total number of counted lifetimes.

**Exclusion of Tip-induced hopping** To exclude tip-induced hopping, two additional movies, M7 and M8, with shorter frame acquisition times than in movie M4 were recorded at 71.0 K. Table 5.2 compares the average lifetimes of movies M4, M7 and M8; the results are in good agreement with each other.

Movie	$T_{\text{start}}$ [K]	$T_{\text{end}}$ [K]	$T$ [K]	$n$	$t_f$ [s]	$m$	Eq.	$\tau$ [s]	$\sigma_\tau$ [s]
M1	65.5	65.7	65.6	40	67.5	8	(5.3)	2605.5	476.1
M2	67.1	67.5	67.3	66	100.0	69	(5.3)	1344.8	130.2
M3	68.9	69.4	69.15	70	100.0	210	(5.2)	460.0	51.2
M4	70.9	71.1	71.0	35	60.0	241	(5.2)	147.7	5.2
M5	72.6	72.8	72.7	63	40.0	305	(5.2)	94.7	5.7
M6	75.5	75.6	75.55	98	21.4	437	(5.2)	30.0	0.5

**Table 5.1 | STM movie details and measured average lifetimes.**  $T$  – mean temperature,  $n$  – total frames,  $t_f$  – acquisition time per frame,  $m$  – total number of hopping events,  $\tau$  – average lifetime,  $\sigma_\tau$  – standard error of  $\tau$ .

Movie	$T_{\text{start}}$ [K]	$T_{\text{end}}$ [K]	$T$ [K]	$n$	$t_f$ [s]	$m$	Eq.	$\tau$ [s]	$\sigma_\tau$ [s]
M4	70.9	71.1	71.0	35	60.0	241	(5.3)	191.7	11.1
M7	71.1	71.2	71.15	16	48.0	29	(5.3)	198.0	37.2
M8	71.2	71.3	71.25	30	33.1	21	(5.3)	213.3	50.8

**Table 5.2 | Comparison of results obtained from movies with different frame acquisition times.** Movies M7 and M8 were analyzed according to Equation (5.3) due to the small number of lifetimes. To provide comparability the same equation was used for movie M4.

### Arrhenius equation

In Figure 5.4  $\ln(\tau^{-1})$  is plotted against  $1000/T$  and a linear fit to the Arrhenius equation is calculated

$$\ln \tau^{-1} = \ln \nu - \frac{E_{\text{act}}}{kT}, \quad (5.5)$$

where each point is weighed by  $\frac{1}{\sigma_{\tau}^2}$ . The fit parameters give the activation energy and the attempt frequency:

$$E_{\text{act}} = 187 \pm 10 \text{ meV} \quad \text{and} \quad \nu = 10^{(11.0 \pm 0.7)} \text{ s}^{-1}.$$

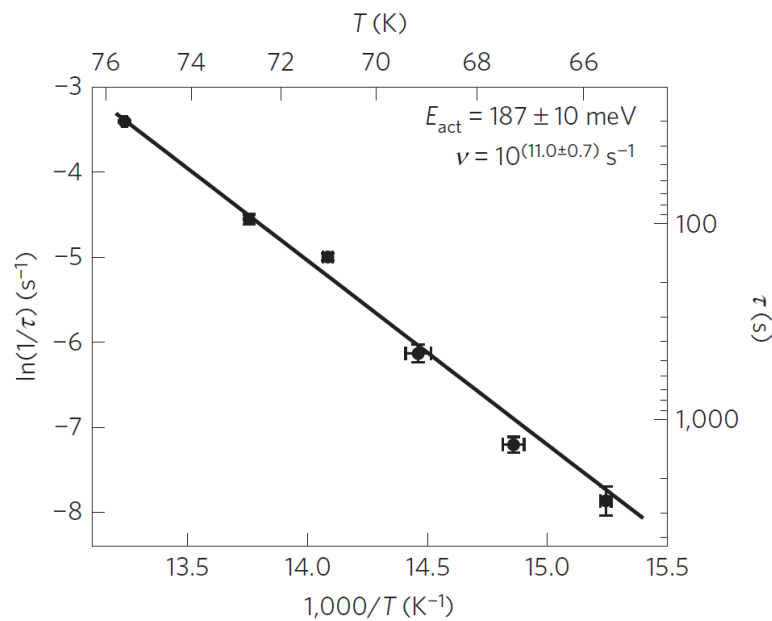


**Figure 5.4 | Arrhenius plot of the average lifetimes.** The plot shows the measured average lifetimes (dots) and the fit (line) according to Equation (5.5). Reprinted by permission from Springer Nature: *Nature Materials* **15**, 450–455 © (2016)

### 5.2.2 Water dimer

The adsorption site of the dimer on both surfaces ( $\text{Sr}_2\text{RuO}_4$  and  $\text{Sr}_3\text{Ru}_2\text{O}_7$ ) was found to depend on the rotation of the  $\text{RuO}_6$  octahedra in the top surface layer.<sup>13</sup> Two configurations were identified in DFT calculations: a dimer across a *narrow* or *wide* site, where narrow and wide refer to the distance of the subsurface oxygen atoms directly beneath the two  $(\text{OH})_{\text{ads}}$  of the dimer; the narrow site was found to be energetically preferred. Since the rotation of the octahedra gives rise to the  $c(2 \times 2)$

surface unit cell, dimers prefer a specific site of the unit cell; the preferred dimer configurations are shown in Figure 5.5a,b for dimers formed along [100] and [010]; the preference for those sites was experimentally confirmed on Sr<sub>2</sub>RuO<sub>4</sub>(001), see Figure 5.5c. In contrast to the monomer, no hopping of the (OH)<sub>ads</sub> of the dimer was observed.

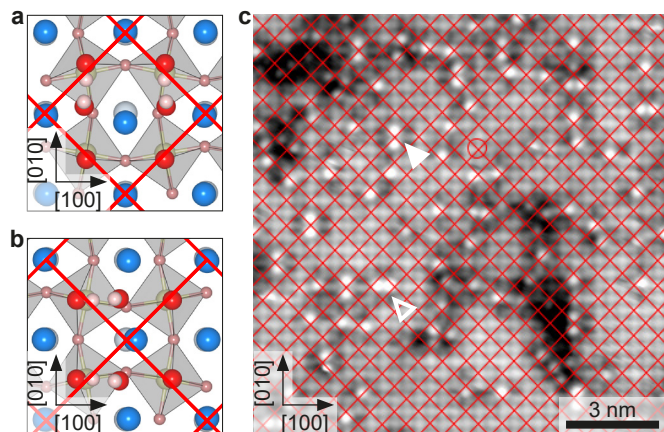


**Figure 5.5 | The preferred dimer adsorption sites.** **a)** and **b)** show the DFT model<sup>87</sup> for a dimer formed along [100] and [010], respectively. **c)** STM image. Dimers formed along [100] (*open triangle*) and [010] (*full triangle*) adsorb exclusively at the preferred adsorption site with respect to the  $c(2 \times 2)$  surface unit cell (*grid*). STM parameters:  $V_s = +0.05$  V,  $I_t = 0.15$  nA,  $T_s = 78$  K; fast scan direction is 21° clockwise from horizontal.

### 5.2.3 Higher coverage and XPS

Figure 5.6a shows the Sr<sub>2</sub>RuO<sub>4</sub>(001) surface after exposure to 1 L of water at 160 K. Chains of dissociated water form a percolating network.<sup>13</sup> In between the bright lines of the chains small areas remain spared out. Here the water appears in the form of isolated, bright spots; their number (up to six) depends on the size of the area. The large-scale image in Figure 5.6b shows the spots in relationship to the underlying surface atoms. Under the assumption that the (OH)<sub>ads</sub> in the chains continue to be positioned in Sr-Sr bridge positions, the bright spots are located mostly on-top of Sr.

A switch in adsorption site from bridge to top position indicates molecular instead of dissociative adsorption, according to calculations in ref. [51]. This was tested in an x-ray photoelectron spectroscopy experiment conducted in the MRS UHV system.<sup>65</sup> The O1s region of the clean, as-cleaved Sr<sub>2</sub>RuO<sub>4</sub>(001) surface shows a two-peak structure, see Figure 5.7c. In ref. [114] it was proposed that this should be due to the

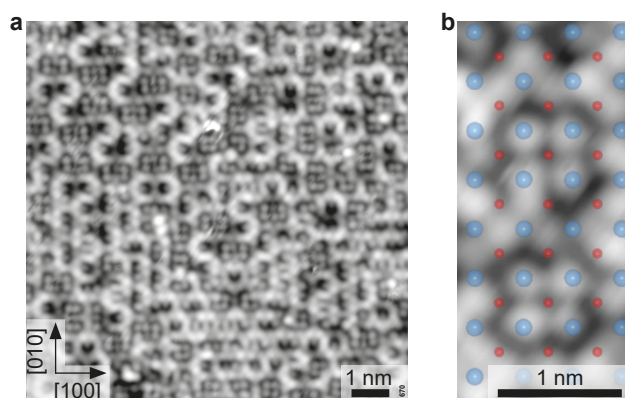


**Figure 5.6 | Full monolayer of water in STM. a)** The sample after dosing 1 L of water at 160 K. Bright lines form a percolating network; bright spots appear in the small areas spared out by the network.  $V_s = +0.5$  V,  $I_t = 0.1$  nA,  $T_s = 78$  K. **b)** Large-scale image with substrate atoms overlaid (Sr–blue, O–red).  $V_s = +0.4$  V,  $I_t = 0.1$  nA,  $T_s = 78$  K; fast scan direction in **a** and **b** is  $53.5^\circ$  counterclockwise from horizontal.

different bonding environments of the apical and the in-plane O atoms within the  $\text{RuO}_6$  octahedra; this is consistent with DFT calculations.<sup>88,89</sup> Upon dosing a small amount of  $\text{H}_2\text{O}$  at 140 K a shoulder at 530.4 eV BE appears that is indicative of OH groups. The substrate O1s peak at 528.4 eV decreases more strongly, in agreement with the assignment of apical O atoms, *i.e.*, the ones residing within the top surface plane. With increasing exposure the shoulder saturates after approximately 0.5 L. Starting from 0.2 L a clearly distinct peak at 532.8 eV develops, consistent with theoretical predictions for the presence of molecular water,<sup>88,89</sup> this peak saturates for a cumulative dose of 1.2 L at 140 K. (Accompanying XPS spectra of the Sr3d region are shown in Figure A.3.) Additional water dosed at a lower temperature (120 K) led to a peak at 533.1 eV, indicative of water multilayers, see Figure 5.8.

### 5.3 Discussion

The experimental confirmation of the theoretically-predicted, constricted motion of the  $(\text{OH})_{\text{ads}}$  fragment<sup>52</sup> raises confidence in computational studies of water adsorption. Moreover, it provides an easy identification of single, dissociated water molecules by STM, even at very low coverage where they are truly isolated. As is expected for a rocksalt-type surface with larger lattice constant, the monomer dissociates.<sup>51</sup> The fact that the O octahedra on a perovskite surface are less rigid as compared to a rocksalt structure contributes to the propensity for dissociation. Probably

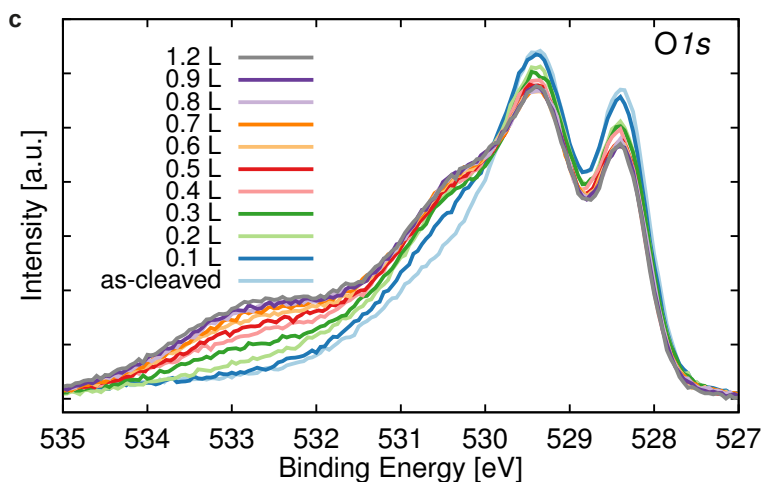


**Figure 5.7 | O1s XPS spectra of increasing water dose at 140 K.** The legend states the cumulative dose. The shoulder and peak at 530.4 eV and 532.8 eV are indicative of hydroxyls and molecular water, respectively. (Monochromatized Al  $K\alpha$ .)

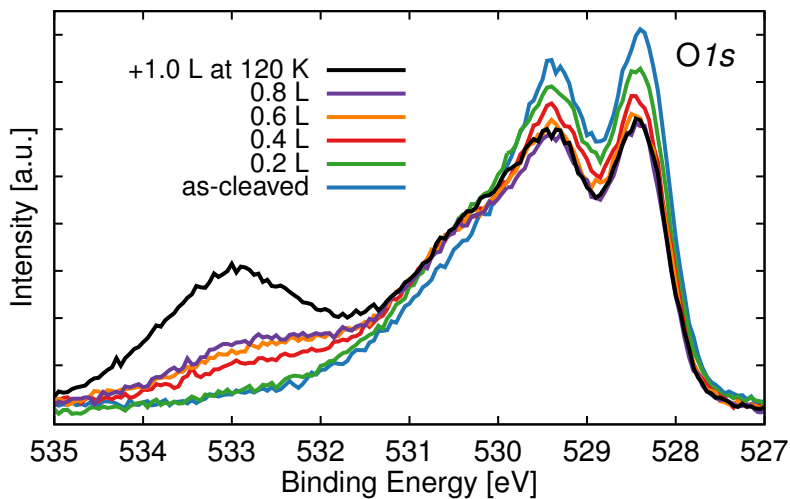


**Figure 5.8 | Water multilayers in the O1s XPS.** Dosing additional 1.2 L  $H_2O$  at 120 K after a cumulative dose of 0.8 L at 140 K leads to a peak at 533.1 eV, indicative of water multilayers. (Monochromatized Al  $K\alpha$ .)



this results in strong hydroxylation of SrO-terminated SrTiO<sub>3</sub>(001) surfaces that has been concluded from friction force measurements.<sup>115</sup> Recent near-ambient pressure XPS experiments report a rather complex O1s feature upon exposure to a humid atmosphere.<sup>116</sup> The XPS spectra in Figures 5.7, 5.8 and A.3, taken on an as-cleaved surface and backed up by atomically-resolved STM results, provide an unequivocal interpretation of the various peaks.

## 5.4 Summary

Water dosed at 110 K adsorbs dissociatively on the (001) surfaces of Sr<sub>2</sub>RuO<sub>4</sub> and Sr<sub>3</sub>Ru<sub>2</sub>O<sub>7</sub>. Sequential STM images show hopping of the (OH)<sub>ads</sub> between Sr-Sr bridge sites, a result already known from previous work.<sup>13</sup> In the present thesis the hopping was modelled as a one-dimensional, thermally activated random walk. The activation energy of the hopping was measured by recording STM movies on Sr<sub>2</sub>RuO<sub>4</sub>(001) at different temperatures; subsequent analysis gave an activation energy of  $187 \pm 10$  meV and an attempt frequency of  $10^{(11.0 \pm 0.7)} \text{ s}^{-1}$ . This result agrees well with the predicted<sup>88</sup> value of 171 meV.

Water dimers prefer a specific adsorption site in the  $c(2 \times 2)$  surface unit cell on Sr<sub>2</sub>RuO<sub>4</sub>(001), confirming the DFT calculation<sup>88</sup> and complementing the analogous measurement on Sr<sub>3</sub>Ru<sub>2</sub>O<sub>7</sub>(001).<sup>13</sup>

At the saturation coverage a switch in the adsorption site from bridge to top position was observed in STM and related to molecular adsorption instead of dissociative adsorption at lower coverage. The molecular adsorption was confirmed by XPS measurements. For water doses greater than 0.5 L a distinct O1s peak at 532.8 eV BE was observed.



# Chapter 6

## CO Adsorption on $\text{Ca}_3\text{Ru}_2\text{O}_7$

### 6.1 Introduction

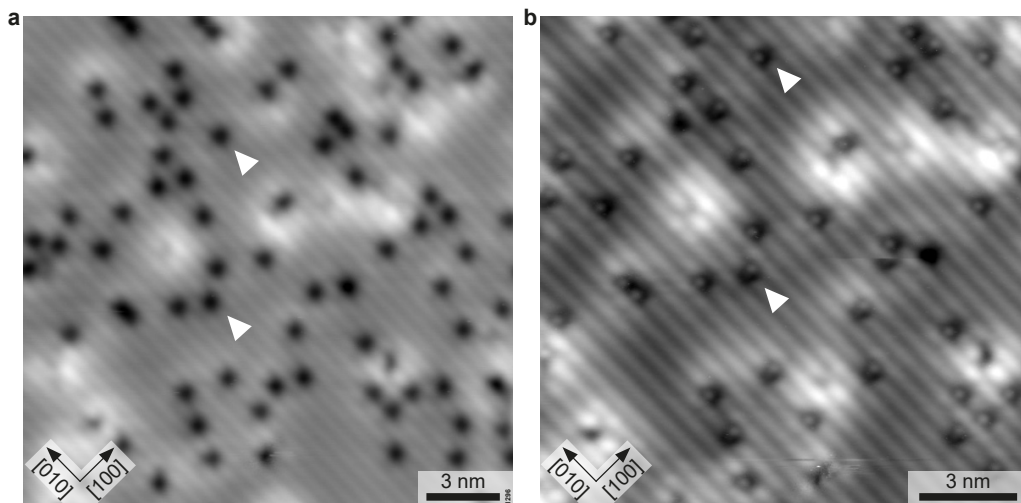
The surface chemistry with respect to carbon monoxide (CO) is of major interest as it is one of the main constituent of the residual gas in a UHV chamber and therefore always present while conducting experiments. An adsorption study on the  $\text{Sr}_3\text{Ru}_2\text{O}_7(001)$  surface<sup>13,117</sup> showed a strong reaction between CO and regular surface sites; CO chemisorbs as a metal carboxylate (Ru-COO) the formation of which involves breaking a bond between a surface oxygen atom and the underlying Ru. It is worthwhile to investigate if and how the tilted  $\text{RuO}_6$  octahedra and less symmetric surface of  $\text{Ca}_3\text{Ru}_2\text{O}_7$  influence the CO adsorption.

### 6.2 Results

#### 6.2.1 Initial adsorption

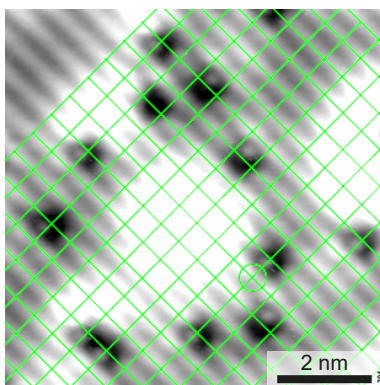
A small dose of 0.002 L CO was dosed into the STM head of the LT-STM to a freshly cleaved  $\text{Ca}_3\text{Ru}_2\text{O}_7(001)$  sample at 78 K. STM images at a sample bias voltage of +0.5 V show the CO as dark depression on the bright substrate lines, see Figure 6.1a. The majority of the depressions appears as single entities, only a few sit close together forming an elongated depression along [010]. Lowering the sample bias voltage to +0.4 V resulted in a tip change; Figure 6.1b shows a zoom-in of the same area as in Figure 6.1a after the tip change. The molecules are still shown as dark depressions but with an additional bright dot; the dot appears on the edge of the depression either in [100] or  $[\bar{1}00]$  direction. The faint, dark point defects with a bright halo are attributed

to impurities from the growth process (see Chapter 3); no obvious preference for or against adsorption close to those impurities is observed upon initial adsorption.



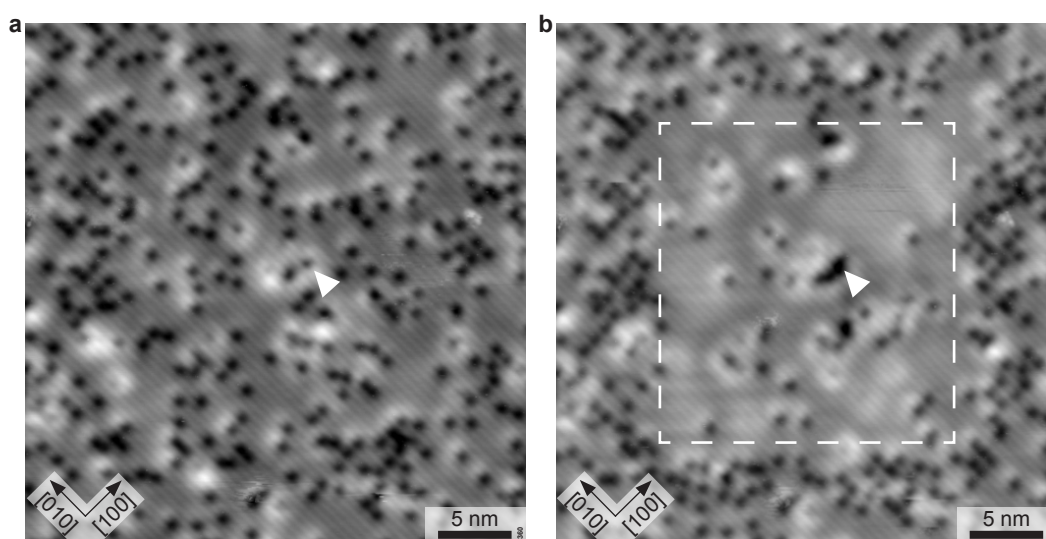
**Figure 6.1 | Initial adsorption of CO.** **a)** STM image after dosing 0.002 L CO. The molecules appear as dark depressions (marked by *triangles*) on the bright substrate lines. STM parameters:  $V_s = +0.5$  V,  $I_t = 0.1$  nA,  $T_s = 78$  K. **b)** Same area as in panel **a** after a tip change. The depressions show a bright dot at their edge. *Triangles* mark the same molecules as in panel **a**. STM parameters:  $V_s = +0.4$  V,  $I_t = 0.1$  nA,  $T_s = 78$  K.

Figure 6.2 shows a zoom-in of the area in Figure 6.1b and an overlaid grid with the dimensions of the surface unit cell of  $\text{Ca}_3\text{Ru}_2\text{O}_7$ . The grid shows that two adsorption sites exist in the unit cell; the orientation of the depression with the bright dot (either  $[100]$  or  $[\bar{1}00]$ ) is equal (opposite) for depressions that are shifted by a (half-)integer number of lattice constants along  $[010]$  relative to each other.



**Figure 6.2 | CO adsorption – registry of adsorption site.** The grid shows that the two orientations are shifted by a half-integer number of lattice constants along  $[010]$  relative to each other. STM parameters:  $V_s = +0.4$  V,  $I_t = 0.1$  nA,  $T_s = 78$  K.

When scanning at a slightly increased sample bias voltage of +0.7 V the adsorbed CO begins to be influenced by the tip; upon each scan the depressions are moved mostly, but not exclusively, along the [010] direction for a few lattice constants (not shown). Figure 6.3a shows the sample after dosing additional 0.002 L CO (cumulative dose 0.004 L) with a tip that shows the CO as dark depressions only, as in Figure 6.1a. The STM image in Figure 6.3b shows the same area as Figure 6.3a and was recorded after scanning an area in the center of the image 32 times with a sample bias voltage of +1.0 V ( $I_t = 0.1$  nA). As a result, almost all molecules were moved to the edge of the scanned area. A few molecules aggregated next to an unknown intrinsic surface defect in the scanned area, indicating a higher adsorption energy than on the pristine surface.



**Figure 6.3 | CO manipulation by the STM tip.** a) STM image of a sample with a cumulative dose of 0.004 L CO. The *triangle* marks a defect. b) Same area as in panel a. The area marked by the *dashed rectangle* was scanned 32 times with  $V_s = +1.0$  V. STM parameters:  $V_s = +0.5$  V,  $I_t = 0.1$  nA,  $T_s = 78$  K.

## 6.2.2 Chemisorption

The weakly bound CO (see Section 6.2.1) can be transformed into a strongly bound species either by the STM tip or by annealing. The weakly bound species will be referred to as precursor in the following. The transformation from the precursor to the chemisorbed state is triggered by either scanning at a sample bias voltage greater or equal to +1.4 V or by annealing at room temperature for 30 min; the exact

temperature necessary for the transformation is unknown.

Figure 6.4a shows the precursor-covered sample as in Figure 6.1a (0.002 L CO), but at a lower sample bias voltage of +0.3 V; at this bias the precursor species appears as faint dark spot on top of the bright substrate line with a bright halo extending in the [010] direction. After one scan with +1.4 V dark, uneven crosses with an almost circular bright halo appear at the previous precursor species locations, see Figure 6.4b.

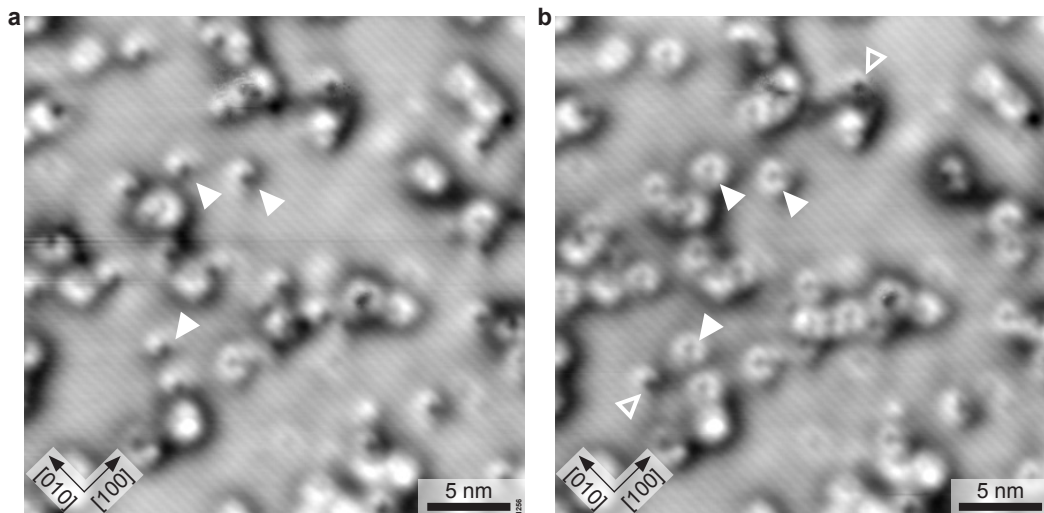


**Figure 6.4 | Transformation of the CO precursor into the chemisorbed species.** **a)** The precursor species (*full triangles*) appears as faint, dark spot with a bright halo extending in the [010] direction. **b)** Same area as in panel **a**. After one scan with  $V_s = +1.4$  V the chemisorbed molecules appear as a dark, uneven cross with an almost circular, bright halo. Some precursor species (*open triangles*) remain or were moved to a new location. STM parameters:  $V_s = +0.3$  V,  $I_t = 0.1$  nA,  $T_s = 78$  K.

A better resolved image of the chemisorbed species is shown in Figure 6.5. The appearance can be described as an uneven, dark cross consisting of one short, more pronounced line and a long, less pronounced line, see insets in Figure 6.5a. Two orientations of the cross are observed. The overlaid grid in Figure 6.5b has the dimensions of the unit cell and shows that the two orientations are shifted by a half-integer number of lattice constants along [010] relatively to each other (similarly to the precursor, see Figure 6.2).

Manipulation by the STM tip requires a higher sample bias voltage than for the precursor; the chemisorbed species is moved by the tip for sample bias voltages above +2.5 V and desorbed at +3.0 V (not shown).

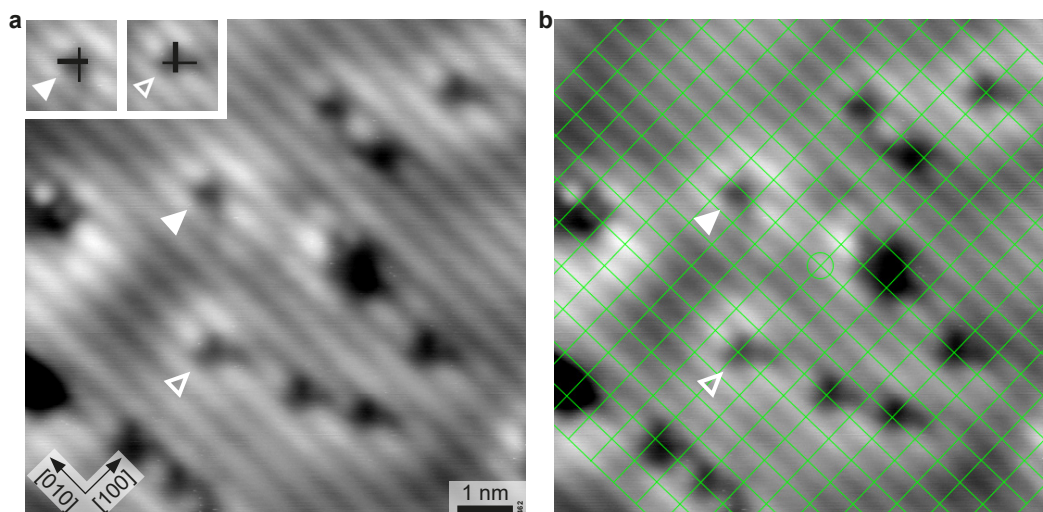


**Figure 6.5 | The chemisorbed species.** **a)** Two similar orientations are observed. The insets show a sketch of the uneven, cross-like appearance. **b)** Same area as in panel **a**. The grid shows that the two orientations are shifted by a half-integer number of lattice constants along  $[010]$  relative to each other. STM parameters:  $V_s = +0.5$  V,  $I_t = 0.1$  nA,  $T_s = 78$  K.

### 6.2.3 DFT

The observation of a weakly bound precursor and a chemisorbed species is in agreement with accompanying DFT calculations.<sup>88</sup> In the precursor configuration CO adsorbs on top of a surface oxygen with an adsorption energy of 0.85 eV (PBE), see Figure 6.6. The formed C-O<sub>surf</sub> bond has a length of 1.42 Å and is tilted mainly towards the  $[100]$  direction, opposite to the tilt of the RuO<sub>6</sub> octahedron. The O of the CO is tilted towards the  $[010]$  direction and the C-O bond length is increased to 1.25 Å compared to a calculated gas-phase value of 1.14 Å. The Ru-O<sub>surf</sub> bond length is 2.14 Å which is 9 % larger than for the pristine RuO<sub>6</sub> octahedron.

In the chemisorbed configuration the carbon atom of the CO replaces the O<sub>surf</sub> and forms a Ru-COO complex with an adsorption energy of 1.85 eV, see Figure 6.7. The Ru-C bond length is 2.04 Å with the Ru lifted by 0.11 Å in  $[001]$  direction compared to the pristine RuO<sub>6</sub> octahedron. The two oxygen atoms of the COO are symmetric to the C and the C-O bond length is 1.3 Å. The OCO angle is 120.3° and the oxygen atoms are oriented along the  $[110]$  direction, pointing towards Ca-Ca bridge sites. A configuration with the COO rotated by 90°, *i.e.*, the two oxygen atoms oriented along the  $[\bar{1}10]$  direction, is disfavoured by 70 meV; the energy penalty arises probably due to the O<sub>surf</sub> of the neighbouring octahedron (the one located in  $[\bar{1}10]$  direction

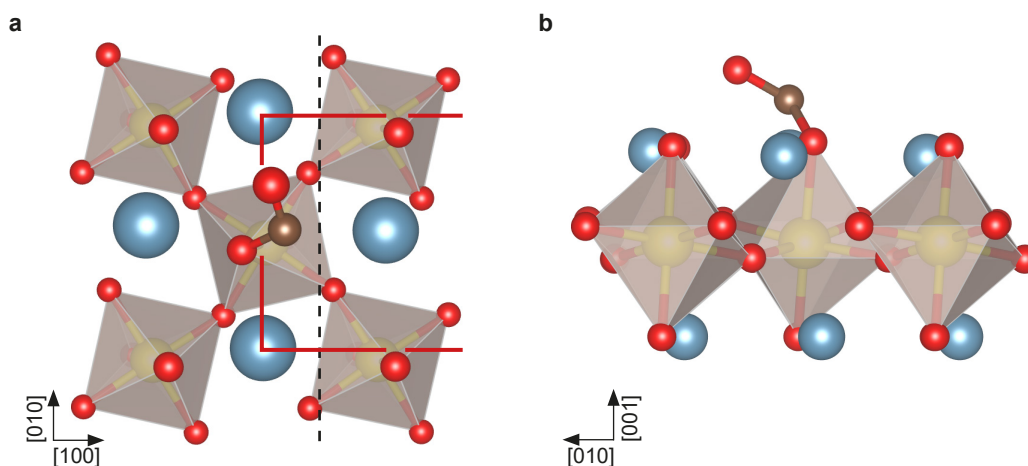


**Figure 6.6 | DFT<sup>88</sup> model of the precursor configuration.** Ca – blue, Ru – yellow, O – red, C – brown. **a)** Top view. The CO forms a  $\text{C-O}_{\text{surf}}$  bond that is tilted mainly towards  $[100]$ . The O of the CO is tilted towards  $[010]$ . The *red line* and the *dashed line* indicate the unit cell and the glide plane of the pristine surface, respectively. **b)** Side view.

relative to the COO) tilting towards the COO.

### 6.3 Discussion

The STM and DFT<sup>88</sup> results for CO adsorption on  $\text{Ca}_3\text{Ru}_2\text{O}_7(001)$  are similar to the results for  $\text{Sr}_3\text{Ru}_2\text{O}_7(001)$ .<sup>13,117</sup> On  $\text{Ca}_3\text{Ru}_2\text{O}_7$  the precursor adsorption energy of 0.85 eV is higher than on  $\text{Sr}_3\text{Ru}_2\text{O}_7$  (0.66 eV); while the bond lengths and the  $\text{O}_{\text{surf}}\text{-C-O}$  angle of the configurations are very similar, the  $\text{Ru-O}_{\text{surf}}\text{-C}$  angle of  $111^\circ$  is significantly smaller than on  $\text{Sr}_3\text{Ru}_2\text{O}_7$  ( $\approx 143^\circ$ ). On  $\text{Sr}_3\text{Ru}_2\text{O}_7$  the tip-induced removal of the precursor at a sample bias voltage of 0.4 V was suggested to be caused by an excitation of a molecule-surface vibrational mode at  $\approx 120$  meV; on  $\text{Ca}_3\text{Ru}_2\text{O}_7$  a significantly higher bias of 1.0 V is required to influence the precursor although the vibrational mode energy is virtually the same.<sup>87</sup> Therefore the proposed mechanism of exciting the molecule-surface vibrational mode is probably not the cause for the tip-induced removal of the precursor.

The chemisorbed Ru-COO is less strongly bound on  $\text{Ca}_3\text{Ru}_2\text{O}_7$  (1.85 eV)<sup>87</sup> than on  $\text{Sr}_3\text{Ru}_2\text{O}_7$  (2.17 eV).<sup>117</sup> The bond lengths and angles of the Ru-COO complex are virtually the same on both substrates; the adsorption energy might be decreased due to the decreased O-Ru-C angle of  $171^\circ$  along the  $c$ -axis of the  $\text{RuCO}_5$  octahedron ( $179^\circ$  for the  $\text{RuO}_6$  octahedra of the pristine surface). The tip-induced desorption



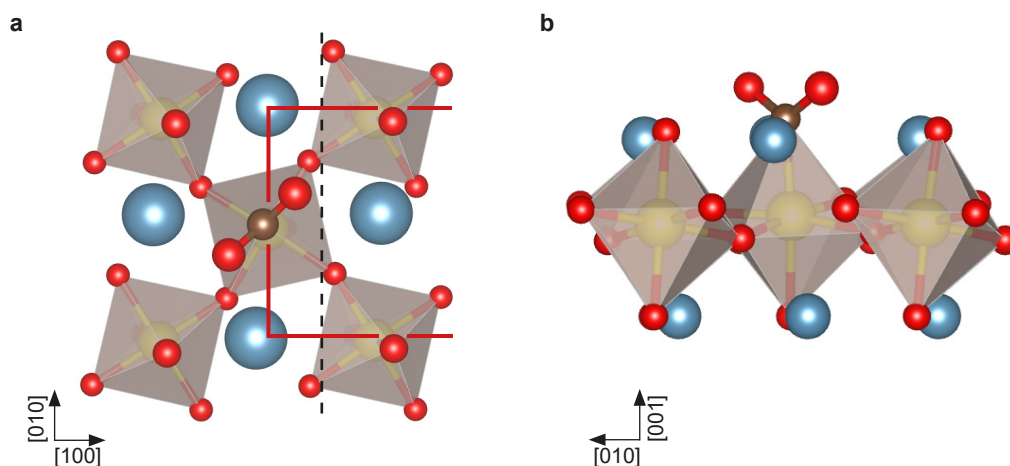


**Figure 6.7 | DFT<sup>88</sup> model of the chemisorbed Ru-COO configuration.** Ca – blue, Ru – yellow, O – red, C – brown. **a)** Top view. The Os of the Ru-COO are oriented along  $[110]$  maximizing the distance to the neighbouring apical O; a configuration that is rotated by  $90^\circ$  is disfavoured. The *red line* and the *dashed line* indicate the unit cell and the glide plane of the pristine surface, respectively. **b)** Side view.

of the chemisorbed species on  $\text{Sr}_3\text{Ru}_2\text{O}_7$  was explained by electron capture into the lowest antibonding O-CO orbital at +2.4 eV; the desorption was observed for sample bias voltages above +2.7 V.<sup>117</sup> On  $\text{Ca}_3\text{Ru}_2\text{O}_7$  a slightly higher bias is necessary for desorption (+3.0 V) which is in agreement with the lowest antibonding O-CO orbital lying slightly higher at +2.7 V.<sup>87</sup> A tip-induced rotation of the COO complex by  $90^\circ$  as observed on  $\text{Sr}_3\text{Ru}_2\text{O}_7$  is hindered by the less symmetric  $\text{Ca}_3\text{Ru}_2\text{O}_7$  unit cell.

The observation of two orientations for both the precursor and the chemisorbed species in STM are in agreement with the unit cell symmetry. The orientations can be transformed into each other by a glide plane operation: mirroring across the  $b$ -axis ( $[010]$ ) and translation by a half lattice constant along  $[010]$  (see the indicated glide plane in Figures 6.6 and 6.7).

## 6.4 Summary

CO initially adsorbs as weakly bound precursor on  $\text{Ca}_3\text{Ru}_2\text{O}_7(001)$  when dosed at 78 K. Depending on the state of the tip the precursor appears in STM either as dark depression only or as dark depression with a bright dot at the edge of the depression; in both cases the depression is centered on the bright substrate line, which is in agreement with DFT models.<sup>87</sup>

Upon scanning at increased sample bias voltage or by annealing to room temperature the precursor is transformed into a strongly bound species. In STM the chemisorbed CO appears as dark, uneven cross and is harder to influence by the tip than the precursor.

Accompanying DFT<sup>87</sup> calculations show that the CO precursor binds to the surface via a C-O<sub>surf</sub> bond ( $E_{\text{ads}} = 0.85$  eV). In the chemisorbed configuration the CO forms a Ru-COO complex with an adsorption energy of 1.85 eV.

The CO adsorption on  $\text{Ca}_3\text{Ru}_2\text{O}_7(001)$  and  $\text{Sr}_3\text{Ru}_2\text{O}_7(001)$ <sup>117</sup> is similar; small differences in the adsorption configurations and energies arise due to the reduced surface symmetry which is related to the tilted  $\text{RuO}_6$  octahedra of  $\text{Ca}_3\text{Ru}_2\text{O}_7$ .

# Chapter 7

## O<sub>2</sub> Adsorption on Ca<sub>3</sub>Ru<sub>2</sub>O<sub>7</sub>

This chapter is based on an article published in *J. Mater. Chem. A* **6**, 5703–5713 (2018), ref. [91]. However, this chapter contains additional information not available in the published article.

### 7.1 Introduction

Molecular O<sub>2</sub> in its triplet ground state is an inert species and requires activation to undergo catalytic reactions or dissociation into atomic oxygen.<sup>10</sup> In general, the activation of O<sub>2</sub> is achieved by either exciting the neutral molecule to one of its two singlet states<sup>118</sup> or by charging the molecule thus forming a superoxide (O<sub>2</sub><sup>-</sup>) or a peroxide (O<sub>2</sub><sup>2-</sup>) ion. If available, the electrons for charging the O<sub>2</sub> can be transferred directly from the oxide surface, but a substantially unperturbed oxide (*i.e.*, stoichiometric, step- and defect-free) rarely provides electrons for a spontaneous formation of charged oxygen species. Often the oxide has to be activated by photo-induced electron transfer, surface intermolecular electron transfer,<sup>119</sup> or the introduction of dopants, defects, or low-coordinated sites.<sup>120</sup>

Superoxo and peroxo species have been predicted and/or observed on a few catalytically relevant binary oxides. In experiments on anatase TiO<sub>2</sub>(101) it was recently experimentally shown that molecular oxygen accepts charge from subsurface Nb<sup>+</sup> dopants, resulting in a mixed adsorption of neutral O<sub>2</sub> and superoxide ions<sup>120</sup> at low temperature (5 K). Charged oxygen species have been predicted for reduced CeO<sub>2</sub>(111)<sup>121</sup>, (110) and (100) surfaces,<sup>122</sup> and their formation has been experimentally confirmed on polycrystalline CeO<sub>2</sub>.<sup>123,124</sup> Calculations for pure ZrO<sub>2</sub> show only

a weak physisorption of O<sub>2</sub> while yttria stabilized zirconia should facilitate dissociation via a superoxo species.<sup>125</sup> Similarly, O<sub>2</sub> is predicted to adsorb weakly on pure ZnO(10 $\bar{1}$ 0)<sup>126</sup> but to form a superoxo species when the ZnO is Al-doped.<sup>127</sup> Charged oxygen species on SnO<sub>2</sub> play a crucial role in chemical sensing, although the correct interpretation of experimental results has been questioned.<sup>128</sup>

Molecular oxygen does not adsorb on the unperturbed CaO(001)<sup>59</sup> and MgO(001)<sup>129</sup> surface. Only after introducing defects by ultraviolet or gamma irradiation, thermal activation, or doping with transition metal ions the formation of charged oxygen species was observed.<sup>58,59</sup> Ultrathin MgO films supported on a metal (Ag or Mo) allow for an electron transfer from the substrate to activate adsorbed oxygen, explaining the catalytic properties of such systems.<sup>129–131</sup>

Turning to ternary oxides, direct experimental evidence on microscopic reaction pathways is sparse. One of the most studied perovskite oxides is SrTiO<sub>3</sub>.<sup>132</sup> Calculations have shown that on the technologically relevant SrO-terminated (001) surface O<sub>2</sub> is activated to O<sub>2</sub><sup>-</sup> only if surface oxygen vacancies are present.<sup>133</sup> In contrast, the defect free LaO-terminated La<sub>2</sub>NiO<sub>4</sub>(001) surface is theoretically predicted to readily chemisorb oxygen either as superoxo or peroxo species.<sup>134</sup>

In the present work, it is shown that the pristine CaO-terminated Ca<sub>3</sub>Ru<sub>2</sub>O<sub>7</sub>(001) surface enables the activation of O<sub>2</sub> to a superoxide ion without a need for prior surface treatment, or the presence of steps, oxygen-vacancies or dopants. Surface spectroscopy in combination with atomically-resolved Scanning Probe Microscopy and DFT calculations<sup>87</sup> confirm the charge state of the as-formed oxygen and provide detailed models for the adsorption geometry of isolated molecules and the dense (2 × 1) O<sub>2</sub><sup>-</sup> overlayer formed at higher coverage.

## 7.2 Results

### 7.2.1 Low coverage

Figure 7.1 shows an STM image of the surface after dosing a small amount of O<sub>2</sub> at 110 K. Compared to the pristine surface the image shows streaks across surface defects. Occasionally the streaks continue along the [010] direction after the tip first scanned across a defect, indicating that an adsorbate was being moved along the bright substrate line. Decreasing the sample bias voltage and the tunneling cur-

rent (minimum  $\approx 25$  pA) or repeating the measurements at LHe temperature did not prevent interactions between the tip and the adsorbates. These first experiments were conducted in the LT-STM, which only provided STM but no AFM measurements.

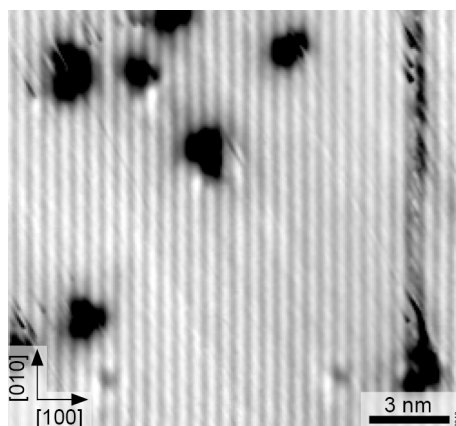


**Figure 7.1 | Interaction between adsorbates and the STM tip after exposure to a low dose of  $O_2$ .** STM image after dosing  $0.025$  L  $O_2$  at  $110$  K. The adsorbates appear as streaks across point defects. STM parameters:  $V_s = +0.1$  V,  $I_t = 0.1$  nA,  $T_s = 78$  K; fast scan direction is  $58^\circ$  clockwise from horizontal.

AFM images taken at  $0$  V sample bias voltage show dark spots of varying contrast and size after exposing the surface to a low dose of  $O_2$ , see Figure 7.2a. When applying a slightly negative or positive sample bias voltage, tunnelling current starts to flow and a few adsorbates interact with the tip (Figure 7.2b). That is in agreement with the STM measurement in Figure 7.1, showing that the adsorbates first adsorb at surface defects and the difficulty of imaging weakly-bound adsorbates with STM, see also Figure 7.7b. In Figure 7.2c two larger, dark spots change their position and contrast in the consecutive image and an additional feature appears in the vicinity of the two spots (Figure 7.2d). This suggests that the varying contrast and size of the dark spots at zero bias voltage can be attributed to adsorbates at surface defects or in non-equilibrium positions, or adsorbates too close to each other to be resolved.

According to the KPFM and XPS measurements (see Sections 7.2.3 and 7.2.4), molecular  $O_2$  adsorbs as a charged molecule. This was confirmed by accompanying DFT calculations<sup>87</sup> including van-der-Waals interactions (vdW-DFT) predicting adsorption of  $O_2$  as superoxo species. In the low-coverage case the molecule adsorbs at a Ca-Ca bridge, see Figure 7.3a. The octahedral tilt leads to two non-equivalent bridge sites, the one chosen by the molecule (B1, equivalent to B2) lies on the on the bright substrate lines. Due to the charge transfer, the intramolecular O-O bond

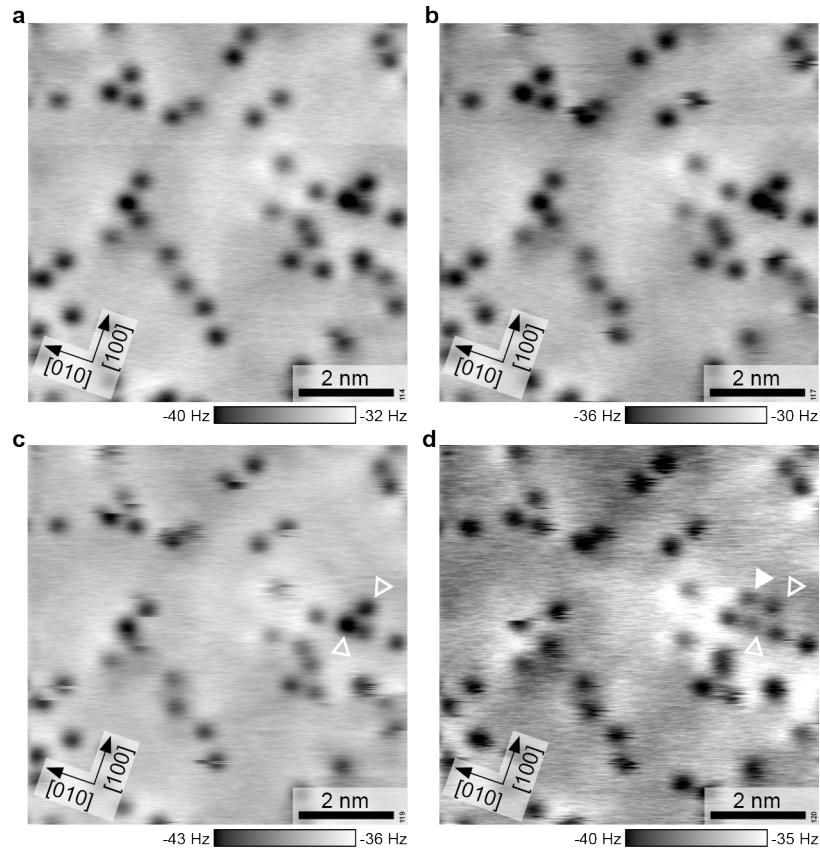


**Figure 7.2 | Interactions between adsorbates and the STM/AFM-tip for varying sample bias voltages.** Constant-height AFM images after dosing 0.8 L of  $O_2$  at 5.5 K. All panels show the same area (common AFM parameters:  $A = 40$  pm,  $T_s = 4.8$  K, scale bars 2 nm) but varying bias voltages and tip-sample distances. **a)**  $V_s = 0$  V. **b)**  $V_s = -120$  mV,  $\Delta z = +25$  pm. **c)**  $V_s = +150$  mV,  $\Delta z = 0$  pm. **d)**  $V_s = +220$  mV,  $\Delta z = +28$  pm. *Open triangles* in **c** and **d** mark the same position. The *full triangle* marks a new feature, suggesting that the darker spots contain more than one adsorbate.

length is increased to a value of 1.35 Å. The molecule is rotated by 34° with respect to the bright [010] substrate lines, and tilted by 29° with respect to the surface plane, see Figure 7.3b. One O of the molecule is located almost at the center of the Ca-Ca bridge (O-Ca1 = 2.37 Å, O-Ca2 = 2.46 Å), the other O sits far away from Ca1 (O-Ca1 = 3.69 Å), but maintains a similar distance to Ca2 (O-Ca2 = 2.34 Å) as the first O due to the tilt of the molecule. The molecule slightly distorts the substrate as the tilt of the two nearest RuO<sub>6</sub> octahedra is increased to 15° compared to 13° in the pristine surface. In addition, the volume of these octahedra decreases by 1.64 % and 0.26 %, respectively, due to a shortening of the Ru-O<sub>surf</sub> bond. The adsorption energy according to vdW-DFT is 1.4 eV. However, higher-level theory invoked for the high-coverage case shows that the adsorption energy is over-estimated by vdW-DFT, see Section 7.2.5. Adsorption at B3 or B4, *i.e.*, at positions where STM shows a dark line, is disfavoured by 0.4 eV due to the shorter distances to the surface oxygen atoms and the resulting repulsion between O<sub>surf</sub><sup>2-</sup> and (O<sub>2</sub>)<sub>ads</sub><sup>-</sup>. Dissociative adsorption results in an energy penalty close to 1 eV.<sup>87</sup>

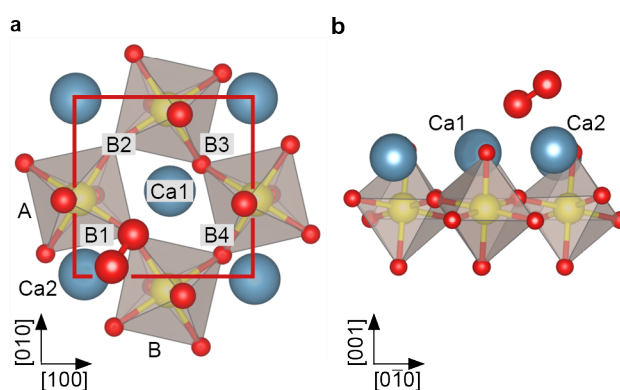


**Figure 7.3** | DFT model<sup>87</sup> of O<sub>2</sub><sup>-</sup> adsorbed on Ca<sub>3</sub>Ru<sub>2</sub>O<sub>7</sub>(001). Ca – blue, Ru – yellow, O – red. **a)** Top view and **b)** side view. The molecule adsorbs as a tilted superoxo species close to a Ca-Ca bridge (here B1).

## 7.2.2 High coverage

STM images of increasing O<sub>2</sub> dose are shown in Figure 7.4. First, the density of streaks (as observed in the low coverage case, Figure 7.1) increases until at sufficient coverage the O<sub>2</sub><sup>-</sup> locally form a (2 × 1) overlayer on a dark background (compared to the pristine surface). Simultaneously, the streaks appear only at the border between

the  $(2 \times 1)$  overlayer and the remaining, uncovered substrate, that appears as bright rows in  $[010]$  direction (Figure 7.4d).

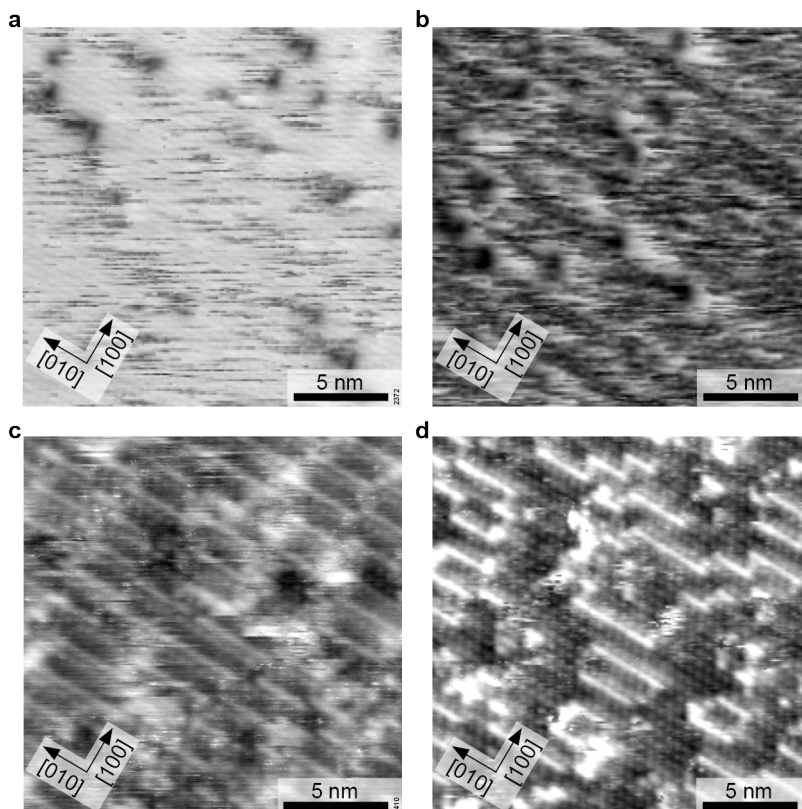


**Figure 7.4 | Increasing  $\text{O}_2^-$  coverage in STM.** Cumulative  $\text{O}_2$  doses at 110 K in panel **a**, **b**, **c** and **d**: 0.075, 0.15, 0.4 and 0.6 L, respectively. **a**) The adsorbate appears as streaks across surface defects and on the pristine surface. **b**) The streak density increases. **c**) The streak density decreases and molecules arranged in rows of bright spots along the  $[010]$  direction become visible. **d**) A  $(2 \times 1)$  overlayer covering most of the sample is clearly visible. Uncovered substrate lines appear as bright rows in  $[010]$  direction. STM parameters:  $V_s = +1.0$  V,  $T_s = 78$  K, **a**  $I_t = 0.1$  nA, **b**  $I_t = 0.025$  nA, **c** and **d**  $I_t = 0.05$  nA.

A detailed STM image of the experimental saturation coverage of close to one monolayer (ML, where 1 ML is defined as one adsorbate per primitive unit cell) is shown in Figure 7.5a. The  $\text{O}_2^-$  covered part of the surface appears as rows of pairs of a bright and a slightly weaker spot on a black background, running in  $[010]$  direction. The distance between the pairs along the row is one lattice constant, and every other gap between the bright and slightly weaker spots is more pronounced. Neighbouring rows are shifted by half a lattice constant in  $[010]$  direction, and appear subtly different as the spots in one row strongly (weakly) undulate with respect to the  $[100]$  direction, marked by *s* (*w*) in Figure 7.5a. The  $\text{O}_2^-$  rows have alternat-



ingly narrow and wide gaps in  $[100]$  direction. The bright, streaky areas are domain boundaries: The spacing of the rows labelled *s* and *w* is narrow in the upper half of the image, but wide in the lower half. The row that undulates strongly in the upper half of the image undulates weakly in the lower half and vice versa. This is because the molecules are shifted half a lattice constant in  $[010]$  direction across the domain boundary, where the row with all  $\text{O}_2^-$  adsorbed in B1 sites becomes a row with all  $\text{O}_2^-$  adsorbed in B2 sites and vice versa (compare to the white dots that mark lattice-constant-intervals along  $[010]$ ). The streaky appearance of the domain boundaries indicates weakly-bound molecules that cannot be imaged with STM. Figure 7.5b shows two  $\text{O}_2^-$  rows (marked by arrows) that start next to an unknown, dark surface defect. Both rows begin with a bright spot followed by the more pronounced gap and a slightly weaker spot.

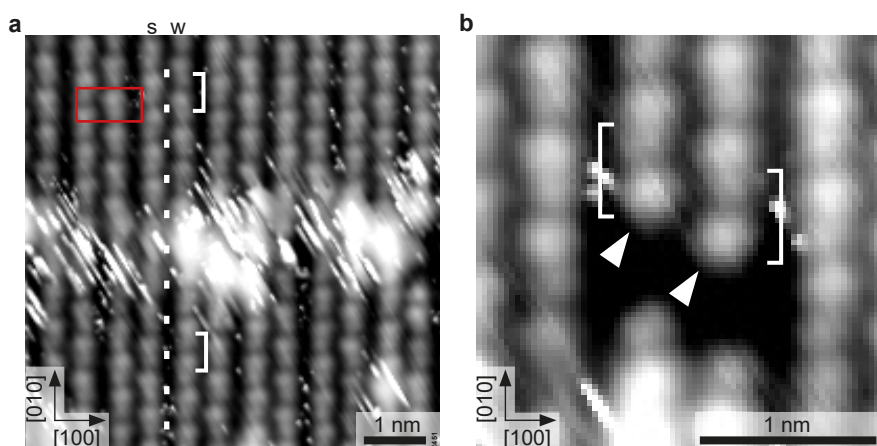


**Figure 7.5 | The  $(2 \times 1)$   $\text{O}_2^-$  overlayer.** **a)** STM image of the  $(2 \times 1)$  overlayer. The bright, streaky area at the center is a domain boundary as indicated by the registry of the *white dots*. The  $\text{O}_2^-$  rows show a weak ('w') or strong ('s') degree of undulation. **b)** Detailed STM image of  $\text{O}_2^-$  adsorbed next to a surface defect. Both rows begin with a bright spot (*arrows*) followed by the distinct node and a slightly weaker spot. STM parameters:  $V_s = +1.0$  V,  $I_t = 0.05$  nA,  $T_s = 78$  K; fast scan direction is  $59^\circ$  clockwise from horizontal.

Accompanying DFT calculations<sup>87</sup> for a coverage of one molecule per primitive unit cell confirmed the adsorption of  $\text{O}_2^-$  in a zigzag arrangement, see the STM simulation and model in Figure 7.6. All  $\text{O}_2^-$  are spaced one lattice constant apart in  $[010]$  direction and adjacent rows are shifted by half a lattice constant in  $[010]$  direction. With the  $\text{O}_2^-$  in one row adsorbed exclusively at the B1 site and in the adjacent one adsorbed exclusively at the B2 site, they form a  $(2 \times 1)$  overlayer. The detailed STM im-

age of the O<sub>2</sub><sup>-</sup> adsorbed next to a surface defect (Figure 7.5b) agrees well with the STM simulation<sup>87</sup>: the bright, elongated spots correspond to a superposition of two lobes of neighboring O<sub>2</sub><sup>-</sup>, separated by a dark node at the center of the molecular bond, rather than between two molecules. The electronic contrast leads to the observed alternating spacing of the rows in STM although the O<sub>2</sub><sup>-</sup> molecules are (physically) equally spaced in [100] direction.

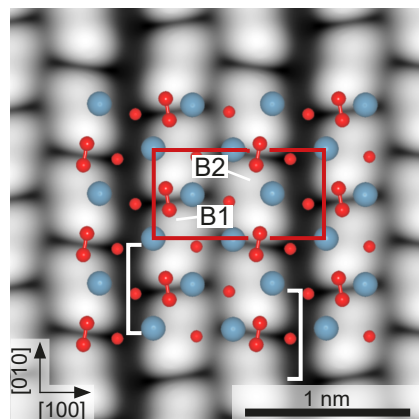


**Figure 7.6 | DFT model<sup>87</sup> and STM simulation of the (2 × 1) overlayer** Ca – blue, O – red. One molecule per primitive unit cell; bridge sites B1 and B2 are labeled as in Figure 7.3a. The O<sub>2</sub><sup>-</sup> appear as bright elongated spots with a dark node in the center (*brackets*);  $V_s = +0.8$  V).

The saturation coverage is shown in Figure 7.7a where the molecules appear as pairs of bright and less bright spots. The bright, streaky areas are domain boundaries of the (2 × 1) overlayer. This results in an apparent coverage of only 0.9 ML when counting all O<sub>2</sub><sup>-</sup> on the rows. The molecules next to the domain boundaries are able to diffuse (induced by the tip), leading to moving domain boundaries in sequentially recorded STM images (see [Electronic Supplement](#), movie O2\_1). To determine where the molecules are adsorbed with respect to the substrate, the overlayer was partially desorbed by scanning with a higher sample bias voltage, see Figure 7.7b. The image shows that the molecules are adsorbed on the bright substrate lines, confirming the DFT<sup>87</sup> adsorption model.

While, as pointed out above, STM disturbs molecules at low coverage too much for reliable imaging, this is possible with AFM. Figure 7.8 shows an AFM image of a sample partially covered with O<sub>2</sub><sup>-</sup>. It should be noted that after the tip approach with non-zero sample bias voltage the tip was moved to a different region with 0 V bias voltage to exclude a possible charging or manipulation of the adsorbate upon

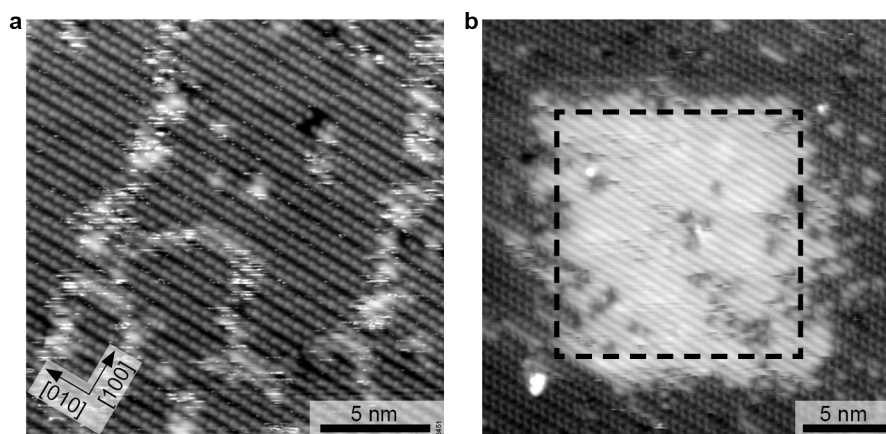


**Figure 7.7 | The  $\text{O}_2^-$ -saturated surface and tip-induced desorption. a)** The saturation coverage after dosing 2.5 L  $\text{O}_2$  at 110 K. The molecules appear as pairs of bright and less bright spots and form a  $(2 \times 1)$  overlayer. The domain boundaries appear as streaky, bright areas. STM parameters:  $V_s = +1.0$  V,  $I_t = 0.05$  nA,  $T_s = 78$  K. **b)** Partially removed  $(2 \times 1)$  overlayer. The area marked by the *dashed box* was previously scanned with  $V_s = +2.0$  V. STM parameters:  $V_s = +1.0$  V,  $I_t = 0.1$  nA,  $T_s = 78$  K

the initial scan. In AFM the molecules are imaged as bright spots (less negative  $\Delta f$ , more repulsive). The surface oxygen atoms of the uncovered sample between the  $\text{O}_2^-$  rows are imaged as faint, bright spots. The overlay shows the surface atoms of the pristine surface aligned to the uncovered part of the sample, and confirms that the  $\text{O}_2^-$  molecules adsorb close to a Ca-Ca bridge. In contrast to STM images the rows are equally spaced by one lattice constant in  $[100]$  direction. Thus the alternating row spacing in STM images (Figure 7.5a) is mainly due to a difference in electronic contrast.

### 7.2.3 Kelvin probe force microscopy

To gain experimental information on the charge state of the adsorbed oxygen, point Kelvin probe force microscopy<sup>135</sup> was performed. For a quantitative analysis it was assumed that the Cu(110) sample used for tip preparation has a work function ( $\phi$ ) of 4.5 eV.<sup>136</sup> The measured local contact potential difference (LCPD) of the Cu sample of +0.4 V (Figure 7.9) gives  $\phi_{\text{tip}} = 4.1$  eV, according to  $V_{\text{LCPD}} = (\phi_{\text{sample}} - \phi_{\text{tip}})/|e|$ , with  $e$  the charge of the electron. This tip was then used to measure the LCPD on a sample where part of the  $(2 \times 1)$  overlayer was removed (similar to one shown in Figure 7.7b) allowing to measure on the  $(2 \times 1)$  overlayer and the pristine surface in close succession, thus excluding a tip change between the measurements. LCPD values of  $-1.45$  V

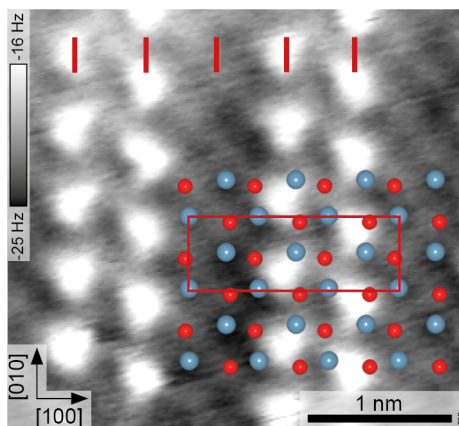


**Figure 7.8 | Partially  $O_2^-$ -covered sample.** Constant-height AFM image of a  $(3 \times 1)$  overlayer after dosing 0.5 L of  $O_2$  at 120 K. *Red ticks* mark lattice-constant intervals along  $[100]$ . The  $O_2^-$  and surface O are imaged as intense and faint, bright spots, respectively (corresponding to repulsion). The overlay shows the surface atoms of the pristine surface; Ca – blue, O – red. AFM parameters:  $A = 500$  pm,  $V_s = 0$  V,  $T_s = 4.8$  K.

and +0.2 V were found for the pristine surface and the  $(2 \times 1)$  overlayer, respectively, see Figure 7.10. Combining the  $\phi_{\text{tip}}$  and the measured LCPDs gives  $\phi_{\text{surf}} = 2.7$  eV and  $\phi_{(2 \times 1)} = 4.3$  eV for the pristine surface and the  $(2 \times 1)$  overlayer, respectively. Such a work function increase is due to a negatively charged adsorbate overlayer.<sup>86</sup> DFT calculations give  $\phi_{\text{surf}} = 3.1$  eV and  $\phi_{(2 \times 1)} = 5.4$  eV.

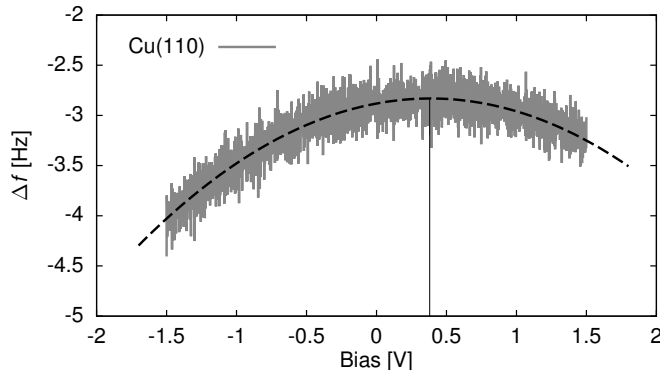


**Figure 7.9 | KPFM on Cu(110).** Point Kelvin probe force microscopy of the pristine Cu(110) surface ( $T_{\text{sample}} = 78$  K). Shown are the measured (*full, noisy line*) and the numerically fitted (*dashed line*) Kelvin parabola, showing that  $V_{\text{LCPD-Cu}} = +0.4$  V.

## 7.2.4 X-ray photoelectron spectroscopy

In XPS the pristine surface exhibits an asymmetric O1s peak at 529.1 eV binding energy (BE), broadened towards the high BE side, see Figure 7.11. According to vdW-

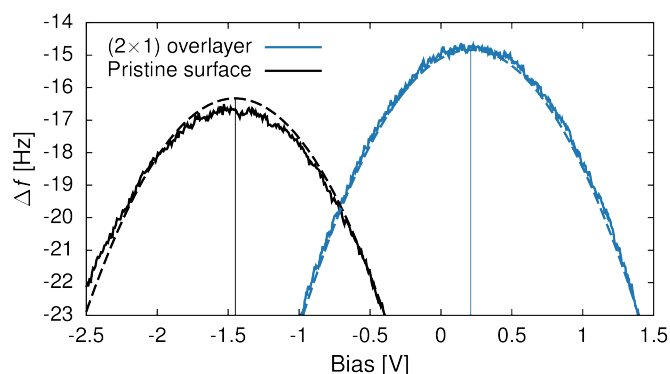


**Figure 7.10 | KPFM of  $\text{O}_2^-$  on  $\text{Ca}_3\text{Ru}_2\text{O}_7$ .** Point Kelvin probe force microscopy of the pristine surface and the  $(2 \times 1)$   $\text{O}_2^-$  overlayer ( $T_{\text{sample}} = 78$  K). Shown are the measured (*full line*) and the numerically fitted (*dashed lines*) Kelvin parabolas, reflecting a change in work function (see main text for analysis details).

DFT calculations the O1s core level for the O atoms in the rock-salt like CaO planes is shifted to 0.7 eV higher BE compared to the  $\text{RuO}_2$  planes, which serve as DFT reference. On a structurally related  $\text{Sr}_2\text{RuO}_4$  sample, two distinct O1s peaks were observed and attributed to the apical and equatorial O atoms, see Section 5.2.3. The observation of only one asymmetric peak for  $\text{Ca}_3\text{Ru}_2\text{O}_7$  is attributed to the limited resolution of the experimental setup, the 3:4 ratio of O atoms in the CaO and  $\text{RuO}_2$  planes, and potentially the different electronic structure of these materials. Exposing the sample to 2.5 L  $\text{O}_2$  at 110 K results in a  $(2 \times 1)$  overlayer and an O1s peak at 532.6 eV BE; *i.e.*, 3.5 eV higher binding energy than the peak of the pristine surface. In addition, the lattice oxygen peak shifts towards lower BE due to an upward band bending of 0.1 eV. The  $\text{O}_2^-$  peak lies approximately half way between reported BEs for physisorbed, neutral  $\text{O}_2$  of 536 to 538 eV,<sup>120,137</sup> and the double negatively charged bulk O at 529.1 eV. Thus, the XPS result is consistent with a superoxo species.

For the superoxo species a double peak with a 1:3 ratio is expected due to the coupling of the O1s hole spin to the  $\text{O}2p$  valence states resulting in a single or triplet final state configuration. Similarly, adsorbed neutral  $\text{O}_2$  leads to a double peak with a 2:4 ratio (doublet and quadruplet) and a splitting of roughly 1 eV.<sup>120,137</sup> The observation of only one broad peak is attributed to the relatively small splitting of 0.25 eV (estimated from DFT calculations) and the limited experimental resolution.

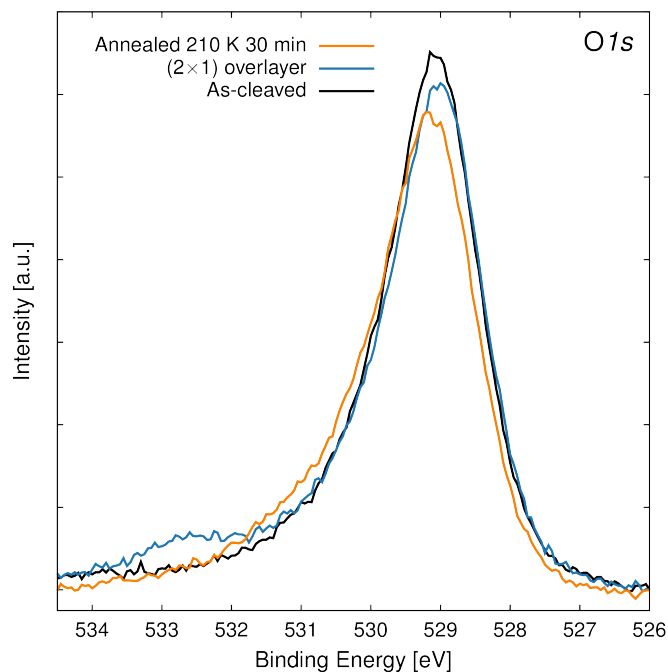


**Figure 7.11 | XPS of O<sub>2</sub><sup>-</sup> on Ca<sub>3</sub>Ru<sub>2</sub>O<sub>7</sub>(001).** O1s spectra of the as-cleaved surface, the (2 × 1) O<sub>2</sub><sup>-</sup> overlayer and after annealing at 210 K for 30 min (Mg Kα, T<sub>sample</sub> = 110 K).

### Annealing at RT

When annealing the O<sub>2</sub><sup>-</sup> saturated sample to room temperature, the molecule desorbs, the band bending vanishes, and subsequent STM images show the pristine surface. The superoxo peak in the O1s XPS starts to disappear at approximately 200 K (Figure 7.11). The slight increase at higher binding energy is probably due to hydroxyls that accumulated during this experiment, see Section 4.2.3. A rough estimate for the adsorption energy based on the desorption temperature is 0.6 eV, which is in good agreement with the calculated (Random phase approximation, RPA) adsorption energy of 0.72 eV, see Section 7.2.5.

### 7.2.5 Charge transfer

Different levels of theory were used to calculate the structure and adsorption energy for O<sub>2</sub><sup>-</sup> on Ca<sub>3</sub>Ru<sub>2</sub>O<sub>7</sub>.<sup>87</sup> For any level of theory the molecule adsorbs as a superoxo species but with considerably different adsorption energies, see Table A.3. A detailed analysis of the energy differences can be found in ref. [91]. The most sophisticated calculation (RPA) resulted in an adsorption energy of 0.72 eV per O<sub>2</sub><sup>-</sup> of the (2 × 1) layer.

The source of electrons for charging the  $O_2$  are the Ru d-states in the  $RuO_2$  subsurface layer below the CaO-terminated surface.<sup>91</sup> According to the calculations, in the metallic phase the electron is transferred from the valence band, while in the insulating phase it is transferred mainly from a neighbouring  $RuO_6$  octahedron, which is also reflected in a stronger contraction of that octahedron. A charge density difference plot for the insulating phase is shown in Figure A.4.

## 7.3 Discussion

The spectroscopic results and DFT calculations<sup>87</sup> conclusively show that molecular oxygen readily adsorbs as  $O_2^-$  on the as-cleaved  $Ca_3Ru_2O_7(001)$  surface. The source of electrons for charging the  $O_2$  are the Ru d-states in the  $RuO_2$  subsurface layer below the CaO-terminated surface. This charge transfer is crucial for the adsorption: on CaO(001) chemisorption was only observed after introducing Mo impurities that donate electrons to the oxide.<sup>59</sup> Here, the metallic  $RuO_2$  layers in  $Ca_3Ru_2O_7$  can be seen as intrinsic electron donors. Consequently a full monolayer of adsorbed  $O_2^-$  can form. An enhancement of the charge transfer due to the Ti impurities in the  $Ca_3Ru_2O_7$  samples (see Chapter 3) is not expected. Calculations<sup>46</sup> showed that Ti, which substitutes Ru, occurs as  $Ti^{4+}$  and contributes very little to the density of states at the Fermi energy. The transfer of a second electron, *i.e.*, the formation of a peroxo species was not observed. According to calculations, this is hindered by a too weak hybridization of the states of the substrate and the molecule.<sup>87,91</sup>

### Comparison to other perovskites

Molecular oxygen adsorbs as a neutral species on defect-free  $SrTiO_3(001)$ ,<sup>133</sup> but as an activated species on  $La_2NiO_4(001)$ .<sup>134</sup> This observation was correlated to the charge transferred from the A-site ions:<sup>134</sup> while  $Sr^{2+}$  does not deviate from its formal ionic charge and no charge transfer is observed, the La charge changes from +3 to +2 for both adsorption modes (peroxo and superoxo), suggesting a covalent bond character between La and the charged molecule. In the present work no major charge transfer from the Ca ions is found: while the Ca ions are polarized, the Ca Bader charge stays +2, similarly to  $Sr^{2+}$  on  $SrTiO_3(001)$ .<sup>133</sup> On  $Ca_3Ru_2O_7(001)$  the charge is transferred from the subsurface Ru to the ionically bonded  $O_2^-$  at the surface. Preliminary DFT calculations<sup>87,88</sup> (not shown) show a similar charge transfer mechanism

on the related, SrO-terminated Sr<sub>3</sub>Ru<sub>2</sub>O<sub>7</sub>(001) surface, suggesting that the difference is due to the energetic levels of the B-site ions.

### **Influence of the work function**

Ultrathin oxide films that are only a few layers (L) thick are often considered as model systems for metal oxide surface chemistry. Calculations for ultrathin MgO films supported on a metal (Mo and Ag) concluded that charge can be transferred from the metal support through the oxide film to the adsorbed oxygen. A comparison of O<sub>2</sub><sup>-</sup> adsorbed on MgO(2L)/Ag ( $\phi = 3.1$  eV)<sup>138</sup> and MgO(3L)/Mo ( $\phi = 2.05$  eV)<sup>138</sup> showed that the adsorption energy<sup>129</sup> is smaller for the system with the higher work function. This suggests that the higher the work function the harder it is to transfer an electron to an adsorbate. The work function and O<sub>2</sub><sup>-</sup> adsorption energy on Ca<sub>3</sub>Ru<sub>2</sub>O<sub>7</sub>(001) of 2.7 eV and 0.72 eV, respectively, are similar to the values for the MgO(2L)/Ag system, 3.1 eV and 0.64 eV.

### **Interaction with the tip**

The formation of a full, adsorbed overlayer of O<sub>2</sub><sup>-</sup>, and the availability of atomically-resolved nc-AFM allows to directly inspect the configurations of the adsorbate, thus providing a tight connection to the theoretical calculations. At low coverage, single O<sub>2</sub><sup>-</sup> could be imaged by AFM, but the application of a relatively low sample bias voltage ( $\approx 100$  mV) already resulted in interactions between the scanning tip and the molecules. The interactions occurred for positive as well as negative sample bias voltages, and the exact threshold varied between 100 and 150 mV depending on the tip-sample distance and the particular molecule. It is well-known that the tip's electric field and/or the tunnelling current can influence adsorbates.<sup>139,140</sup> The calculated O-O stretch mode for the adsorbed O<sub>2</sub><sup>-</sup> lies at 139 meV ( $1121$  cm<sup>-1</sup>),<sup>87</sup> exciting this mode could be the reason for the observed tip-adsorbate interaction. At higher sample bias voltages of roughly -1 and +2 V the O<sub>2</sub><sup>-</sup> is desorbed by the tip and the pristine surface is revealed. The desorption at negative sample bias voltage, where the electrons tunnel from the molecule to the tip, might be facilitated by discharging the O<sub>2</sub><sup>-</sup> as shown on anatase TiO<sub>2</sub>(101).<sup>120</sup>

At increasing coverages the O<sub>2</sub><sup>-</sup> form a (2 × 1) overlayer up to an apparent (in STM) saturation coverage of close to 1 ML. In contrast to isolated O<sub>2</sub><sup>-</sup> the molecules in the overlayer can be imaged by STM without perturbation by the tip, except for



the overlayer domain boundaries. Within the ordered overlayer the molecules are not moved about by the STM tip, probably because they are locked in by adjacent molecules, while at the domain boundaries tip-induced movement of molecules is possible. This agrees with the observation that after desorbing the  $\text{O}_2^-$  from a specific area by scanning at higher sample bias voltage, molecules from the surrounding area diffuse back to the area again during subsequent STM images taken at the usual, lower bias (see [Electronic Supplement](#), movie O2\_2).

### Realistic working conditions

Applications utilizing the ORR usually operate at much higher temperatures than the experimental temperatures of the present work. Therefore it is interesting how the interaction with  $\text{O}_2$  would change at realistic working conditions. As the tilting/rotation of the  $\text{RuO}_6$  octahedra strongly influences the adsorption energy of  $\text{O}_2^-$  in the different adsorption sites (B1/B2 and B3/B4, see Table 4.2) it is appropriate to consider what happens to the  $\text{RuO}_6$  as the temperature is raised. The temperature dependence of the  $\text{Ca}_3\text{Ru}_2\text{O}_7$  structure was studied by Yoshida *et al.*<sup>33</sup> using neutron scattering up to 292 K. Up to this temperature their data suggests that the  $\text{RuO}_6$  tilting angle slightly decreases but the structure does not undergo any dramatic changes. The orthorhombic structure of  $\text{Ca}_2\text{RuO}_4$  and  $\text{Ca}_3\text{Ru}_2\text{O}_7$  is caused by  $\text{RuO}_6$  octahedral rotation and tilt. For  $\text{Ca}_2\text{RuO}_4$ , when both rotation and tilt disappear at elevated temperatures ( $> 357$  K), its structure becomes tetragonal.<sup>141</sup> If  $\text{Ca}_3\text{Ru}_2\text{O}_7$  follows a similar trend (this has not been studied), adsorption of  $\text{O}_2$  as superoxo species would still be expected as it was calculated for tetragonal  $\text{Sr}_3\text{Ru}_2\text{O}_7$  (not published). However, due to the rather low adsorption energy of approximately 0.6 eV, the oxygen partial pressure would have to be substantially increased to achieve any  $\text{O}_2^-$  coverage at elevated temperatures: for example, if a simple Langmuir adsorption model is assumed, the  $\text{O}_2$  partial pressure necessary for a coverage of 0.5 ML at 900 K is 1 bar. Regarding a possible change of the surface termination at elevated temperatures it can only be speculated that a  $\text{RuO}_2$ -terminated surface would reconstruct. This is based on the fact that the CaO termination is by far the lowest-energy configuration, and that  $\text{SrTiO}_3$  (the only perovskite, where a significant number of surface studies are available) is known to form a variety of complex reconstructions with a structure that is sensitively dependent on the composition.<sup>142</sup> However, studies of different perovskite-type materials after high temperature (1000 °C) treatment under

oxidizing conditions suggest that the surfaces are AO-terminated.<sup>143</sup>

## 7.4 Summary

Exposure of the Ca<sub>3</sub>Ru<sub>2</sub>O<sub>7</sub>(001) surface to O<sub>2</sub> at low temperatures ( $\approx 110$  K and 5.5 K) results in the adsorption of a superoxo species. When no sample bias voltage is applied, isolated O<sub>2</sub><sup>-</sup> can be imaged in AFM. At relatively small sample bias voltages ( $\approx 100$  mV) isolated O<sub>2</sub><sup>-</sup> molecules begin to strongly interact with the STM/AFM-tip. The interaction leads to streaks in the images and tip-induced movement of the O<sub>2</sub><sup>-</sup>. When the O<sub>2</sub><sup>-</sup> coverage is increased, an ordered (2 × 1) overlayer forms, which can be imaged in STM without the described tip-adsorbate interaction. Depending on the state of the STM tip, the O<sub>2</sub><sup>-</sup> molecule appears either as a single spot or a pair of spots (one slightly weaker than the other). At the saturation coverage of one O<sub>2</sub><sup>-</sup> per unit cell the (2 × 1) overlayer covers the complete surface and forms domain boundaries. O<sub>2</sub><sup>-</sup> adsorbed at the domain boundaries interact with the tip similar to the isolated O<sub>2</sub><sup>-</sup> at low coverage. The O<sub>2</sub><sup>-</sup> desorb when scanning at higher sample bias voltages of -1 V or +2 V, or when the sample is annealed above 210 K. A rough estimate for the adsorption energy based on the desorption temperature is 0.6 eV.

The negative charge state of the O<sub>2</sub><sup>-</sup> molecules is evident in Kelvin Probe Force Microscopy and XPS. The work function increases from  $\phi_{\text{pristine}} = 2.7$  eV to  $\phi_{(2 \times 1)} = 4.3$  eV which is in accordance with a negatively charged overlayer. In XPS the O<sub>2</sub><sup>-</sup> results in an O1s peak at 532.6 eV BE, *i.e.*, 3.5 eV above the peak of the pristine surface.

Accompanying DFT calculations<sup>87,88</sup> show that the charge is transferred from the Ru d states to the adsorbate and provide models of the adsorption configurations which are in accordance with the experimental findings.

# Chapter 8

## Electronic Effects on $\text{Ca}_3\text{Ru}_2\text{O}_7$

### 8.1 Introduction

When investigating the  $\text{Ca}_3\text{Ru}_2\text{O}_7(001)$  surface in the QPlus UHV system, which offers the most sensitive STM and AFM capabilities, two unusual effects were observed. First, constant-height images of the as-cleaved surface displaying the tunneling current showed unusually thin lines with a width in the 10 pm range. Secondly, when single  $\text{O}_2^-$  molecules were adsorbed, sudden and locally confined changes in the tunneling conductance were observed. Both effects were only present at LHe temperature ( $T_s = 4.8$  K). The cause for the observed effects is probably linked to the correlated and exotic electronic structure of  $\text{Ca}_3\text{Ru}_2\text{O}_7$ .

### 8.2 Results

#### 8.2.1 Thin lines

The constant-current STM image of the as-cleaved surface in Figure 8.1 shows thin lines of different shapes. Lines with open and closed paths are found. Along its path the same line can appear either brighter or darker than its background. Generally, the lines (open or closed) seem to curl around a common center that influences the path of lines that come close to it; for example, in the marked region in Figure 8.1a the open lines appear to curl around the center of the “inner” closed line. Occasionally the lines cross each other.

A simultaneously recorded STM and AFM image of a different area is shown in Figure 8.2. Several dark and bright lines are observed in the tunneling-current im-

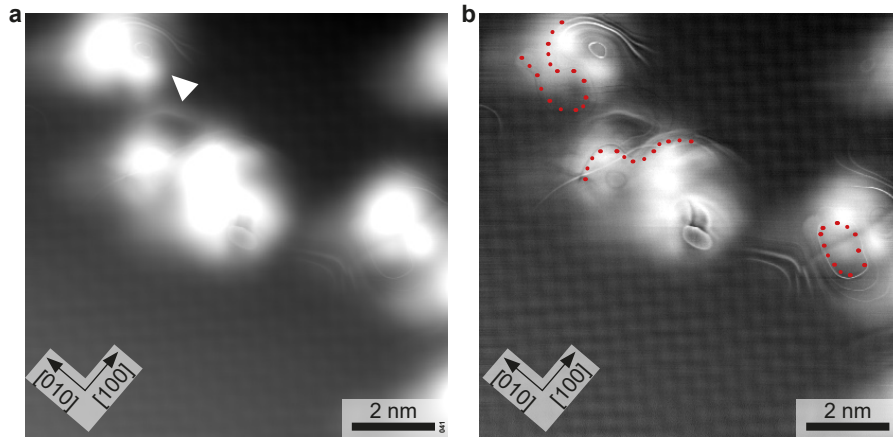


**Figure 8.1 | Thin lines on the as-cleaved surface.** **a)** Constant-current STM image. Open and closed thin lines of different shapes can be seen. The *triangle* marks the detail that is shown in Figure 8.3. STM parameters:  $V_s = +0.25 \text{ V}$ ,  $I_t = 0.03 \text{ nA}$ ,  $T_s = 4.8 \text{ K}$ . **b)** High-pass filtered image of **a**, providing better visibility of the lines. The *dots* outline the path of a few selected lines to guide the eye.

age. The atomically-resolved frequency-shift image shows the pristine surface with the  $\text{O}_{\text{surf}}$  appearing as bright dots arranged in zigzag lines (see Chapter 1). The frequency-shift image shows no obvious surface defects that might cause the lines in the tunneling-current image, but at three locations the dark area between the bright zigzag lines appears slightly darker than in the rest of the image. These subtle frequency-shift variations are most probably caused by subsurface defects. However, the locations of the suspected defects do not exactly correlate with the position or shape of the tunneling-current lines.

A sequence of constant-height images at different sample bias voltages of the detail marked in Figure 8.1a is shown in Figure 8.3; the images show the tunneling current. In empty states the area enclosed by the innermost line increases in diameter when the bias is lowered from +300 to +150 mV. The two bright lines in the top of the image shift outwards as well. In filled-states first only a bright region appears, the shape of which resembles the line observed in empty states at +150 mV. With increasing negative bias, closed lines appear also in the filled-states images. At -110 mV at least four concentric, closed lines can be distinguished. The images show that the position and intensity of the lines is clearly bias-dependent.

Thin, concentric lines on a different sample are shown in Figure 8.4. With increasing tip-sample distance (at constant bias) the lines shift towards the center of the image, *i.e.*, the curvature radius of the lines becomes smaller. The bias-dependence

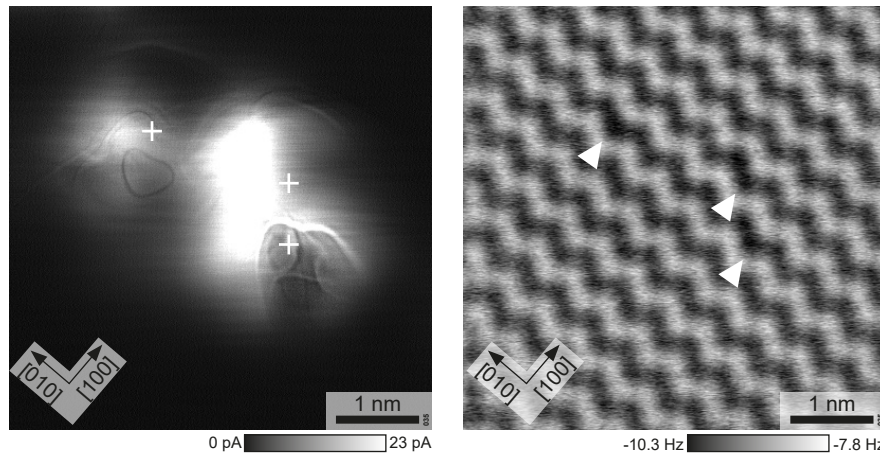


**Figure 8.2 | Simultaneous, constant-height STM and AFM image of the thin lines.** The crosses in the tunneling-current image (left) mark the locations of the slightly darker regions (*triangles*) in the frequency-shift image (right). AFM parameters:  $A = 50$  pm,  $V_s = 0.24$  V,  $T_s = 4.8$  K.

of two lines was investigated by tunneling spectroscopy. Figure 8.5a shows a  $dI/dV$  map of spectra recorded along the path marked in Figure 8.4. The dispersion of the two states that are imaged as lines in the empty-states images (Figure 8.4) is clearly visible (marked by arrows). At least three states can be seen in the the filled-states half of the  $dI/dV$  map. A few selected  $dI/dV$  spectra of adjacent measurement points are shown in Figure 8.5b. The spectra show the band gap from approximately  $-50$  to  $+80$  mV and the local  $dI/dV$  maxima that shift in energy depending on the recording location of the spectra, *i.e.*, the position of the tip.

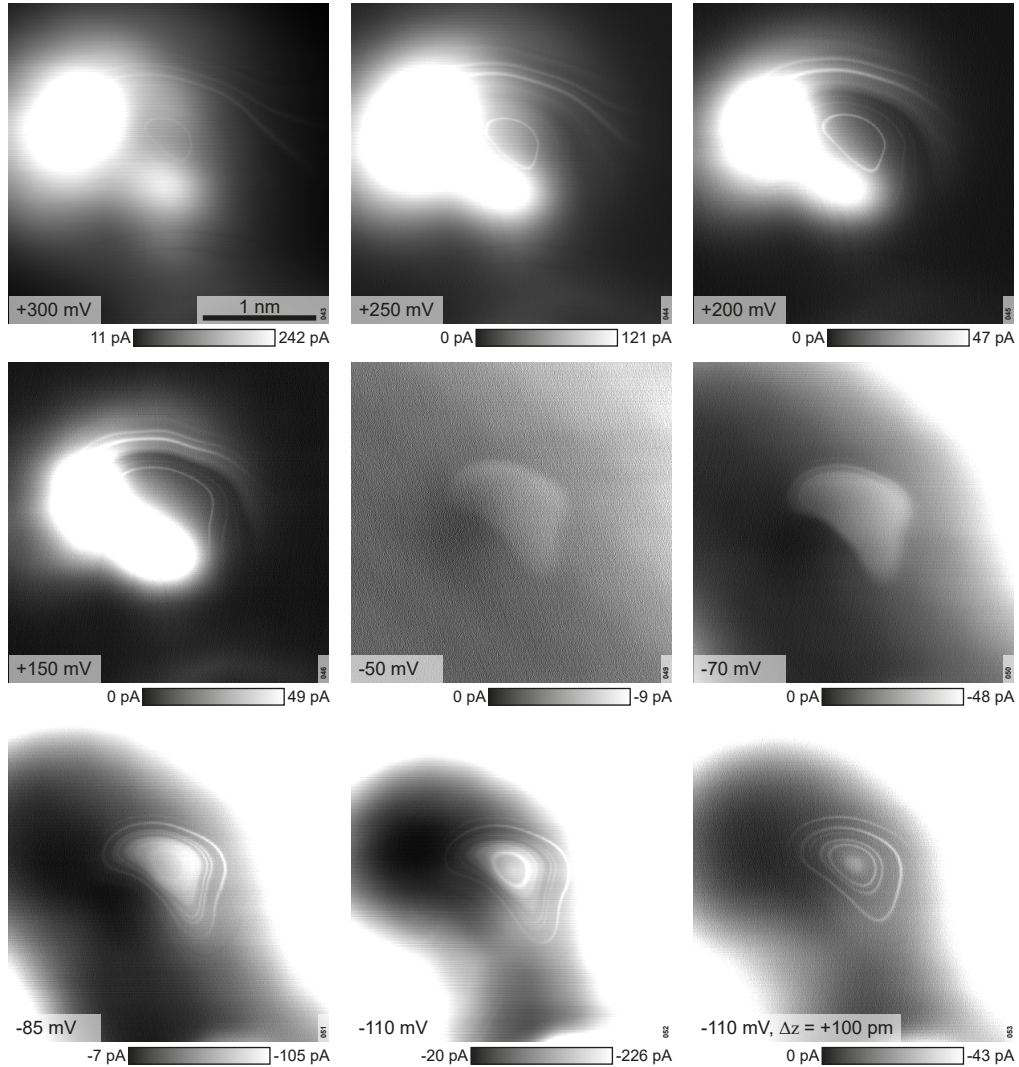


**Figure 8.3 | Bias-dependence of concentric lines in empty and filled states.** Constant-height images of the same area showing the tunneling current at different sample bias voltages (see labels). All images show the same area; the scale bar applies to all images.  $T_s = 4.8$  K.

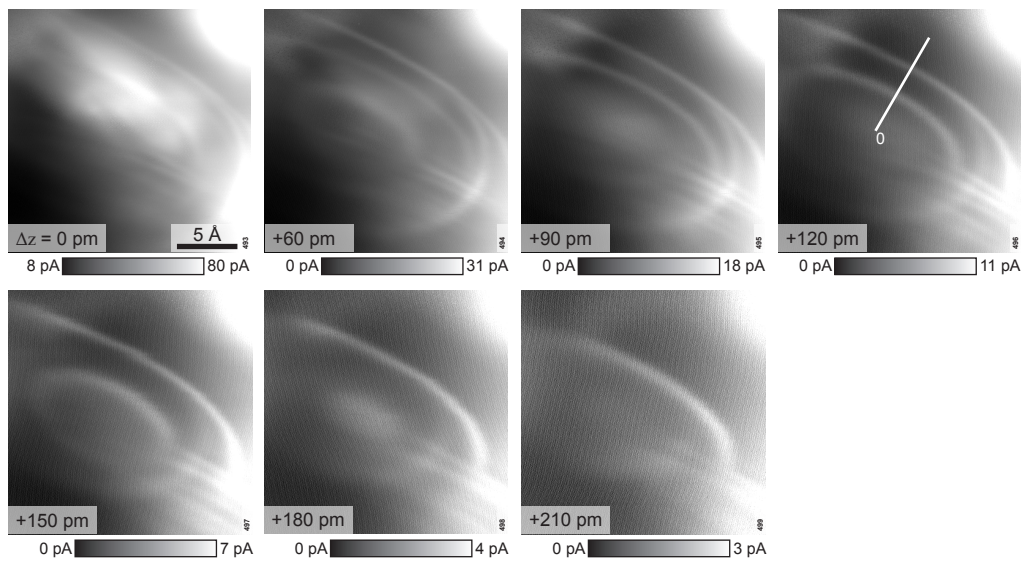


**Figure 8.4 | Influence of the tip-sample distance on concentric lines.** Constant-height images of the same area showing the tunneling current at increasing tip-sample distance (see labels). The *line* marks the measurement location of the  $dI/dV$  spectra shown in Figure 8.5. STM parameters:  $V_s = +0.25$  V,  $T_s = 4.8$  K.

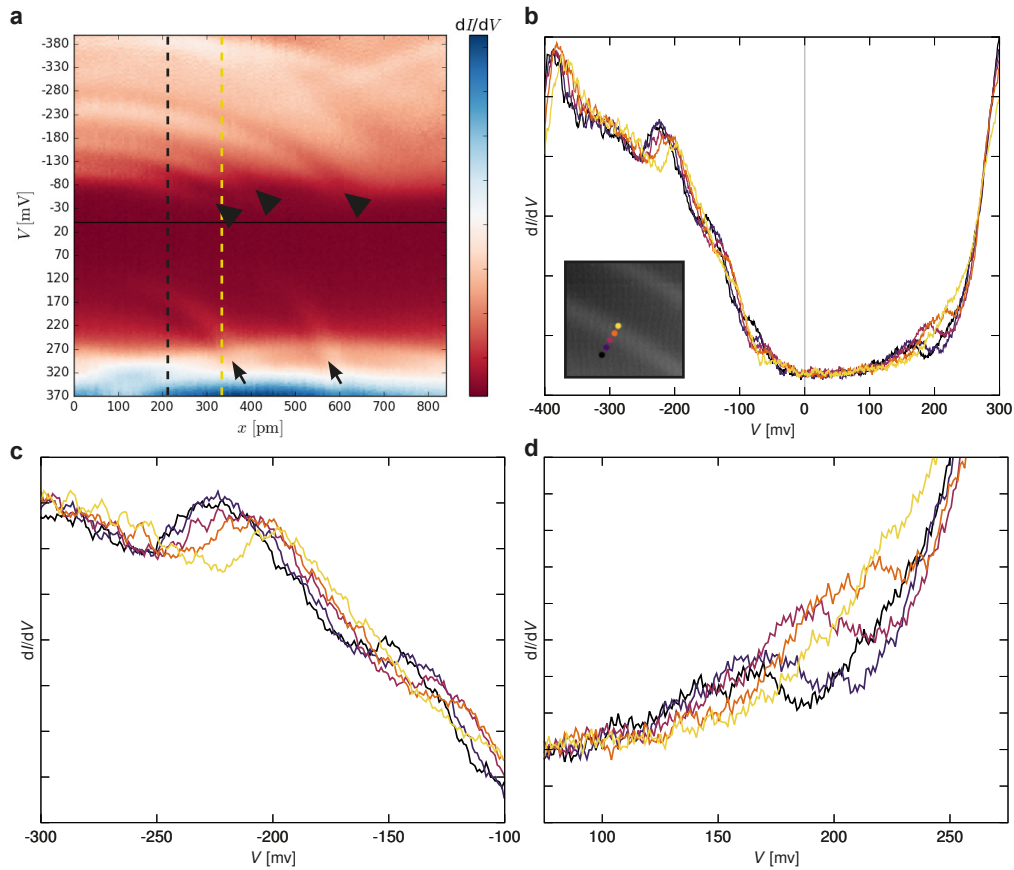


**Figure 8.5 | Tunneling Spectroscopy.** **a)**  $dI/dV$  map of spectra recorded along the path marked in Figure 8.4. Dispersed empty- and filled-states are marked by *arrows* and *triangles*, respectively. The color-coded *dotted lines* mark the positions of the first and last spectra shown in panel **b**. **b)** Selected  $dI/dV$  spectra from adjacent points (see inset) showing the band gap and the local maxima attributed to the dispersed states shown in panel **a**. **c,d)** Zoom-in of **b** showing the local  $dI/dV$  maxima. Lock-in parameters:  $V_{pp} = 20$  mV,  $f = 123$  Hz.



## 8.2.2 Random telegraph noise

In Chapter 7 it was shown that molecular oxygen adsorbs as  $O_2^-$  on  $Ca_3Ru_2O_7$  and that single superoxo species imaged by AFM are influenced by the tip when a sample bias voltage is applied. Here it will be shown that the corresponding tunneling-current images show sudden, locally confined conductance changes of the surface and that measurements of the tunneling-current over time at a fixed tip-position resulted in random telegraph noise signals.

Simultaneously recorded AFM and STM images of a sample covered by single superoxo species are shown in Figure 8.6. At slightly negative sample bias voltage (Figure 8.6a) the tunneling current image shows sudden changes in the conductance. The simultaneous AFM image shows streaks across three  $O_2^-$  indicating some influence by the scanning tip; the  $O_2^-$  were not desorbed by the tip as sequentially recorded images showed. The conductance changes are not correlated in time or location to the the influenced  $O_2^-$ . At positive bias (Figure 8.6b) the conductance changes frequently and the majority of  $O_2^-$  is influenced by the tip. Again, a spatial correlation between the  $O_2^-$  and the conductance changes is not found.

A different sample with a lower coverage of  $O_2^-$  is shown in Figure 8.7. At a sample bias voltage of +60 mV the tunneling current is zero for certain areas on the surface that appear slightly brighter in the AFM image; these variations indicate that the band gap (tunneling current) and the electrostatics (frequency shift) are not homogeneous across the surface. A single  $O_2^-$  is adsorbed in the center of an area that has two different diameters depending on the position of the  $O_2^-$ : while scanning, the diameter of the area suddenly changes (Figure 8.7a). In the image shown in Figure 8.7b most of the area is in its small-diameter state and the AFM image shows that the  $O_2^-$  position shifted by half a unit cell in [010] direction compared to Figure 8.7a (where the area was in its large-diameter state at the time the  $O_2^-$  was imaged in AFM). The area switches back to its large-diameter state in the upper half of the image. In the images shown the switching occurs at the same lateral distance between tip and  $O_2^-$ , but in other images (not shown) the switching occurs also at different distances.

When recording the tunneling current over time with the tip at a fixed position (marked in Figure 8.7b) that lies inside the large-diameter area but outside the small-diameter area the signal switches between two distinct values, *i.e.*, a low state and high state, see Figure 8.8. Two measurements with sample bias voltages of +160 and

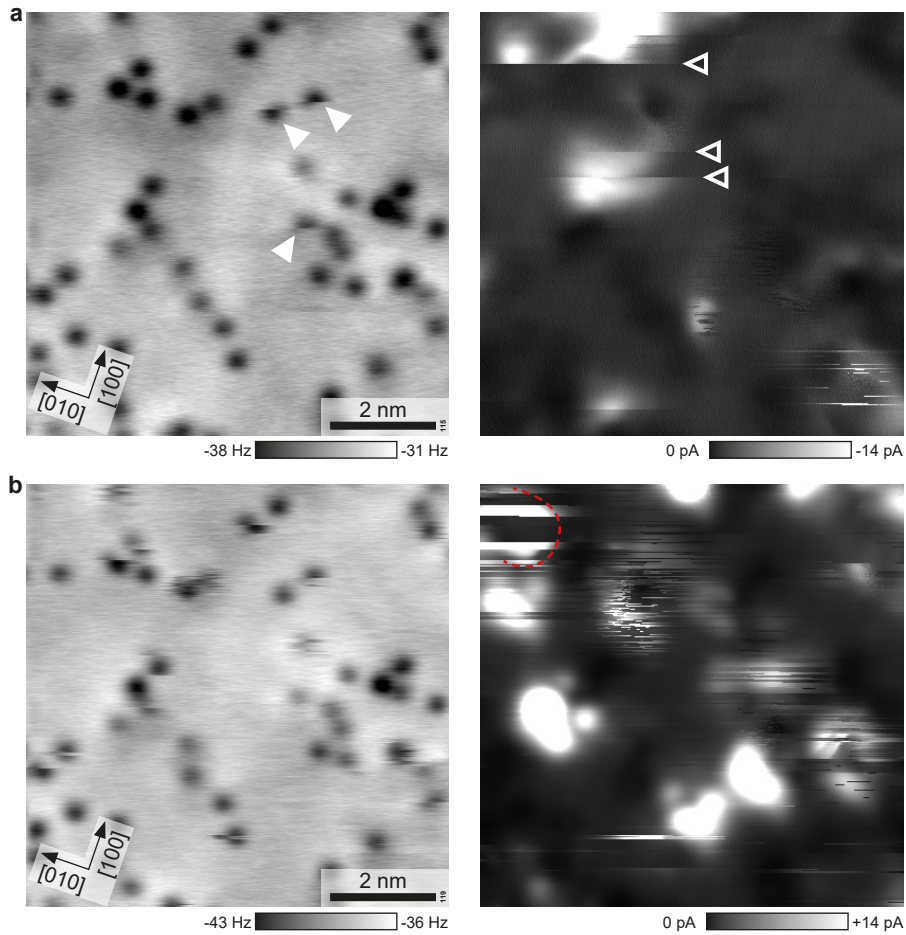


**Figure 8.6 | Sudden conductance changes.** Simultaneously recorded constant-height AFM and STM images. Adsorbed  $\text{O}_2^-$  appear as dark spots in the AFM images. **a)** Three  $\text{O}_2^-$  are influenced by the tip (*full triangles*). Sudden conductance changes are observed (*open triangles*) in the tunneling current image. AFM parameters:  $A = 40 \text{ pm}$ ,  $V_s = -0.05 \text{ V}$ ,  $T_s = 4.8 \text{ K}$ . **b)** Same area with slightly higher bias voltage. The influence on the adsorbed  $\text{O}_2^-$  is somewhat enhanced. In the circular region (*dashed line*) the conductance apparently switches between a high- and low-conductance state. AFM parameters:  $A = 40 \text{ pm}$ ,  $V_s = +0.15 \text{ V}$ ,  $T_s = 4.8 \text{ K}$ .

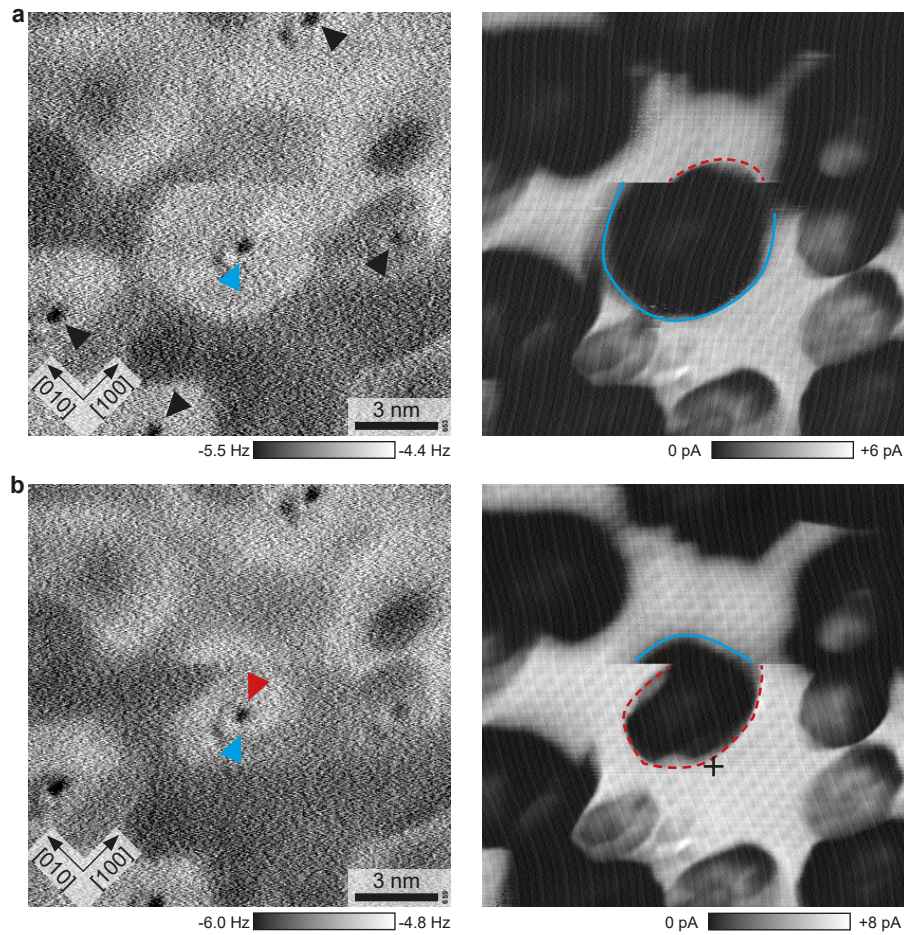


**Figure 8.7 | Conductance related to the position of a superoxo species.**  $\text{O}_2^-$  appear as dark spots (*triangles* in **a**) in AFM. **a)** The *blue triangle* marks the  $\text{O}_2^-$  position, the *blue line* marks the outline of the large-diameter state. **b)** The *red triangle* marks the new  $\text{O}_2^-$  position, the *blue line* marks the outline of the small-diameter state. The *cross* marks the tip-position for the signals shown in Figure 8.8.  $A = 150 \text{ pm}$ ,  $V_s = +0.06 \text{ V}$ ,  $T_s = 4.8 \text{ K}$ ; slow scan direction: up.

+180 mV are shown. At higher bias the switching occurs more often and the time spent in the high state increases. The form of the signal is that of Random Telegraph Noise (RTN) that occurs in metal-oxide-semiconductor transistors due to charge trapping at oxide defects,<sup>144</sup> hence the signals will be referred to as RTN signals; the time of the individual segments that the signal spends in the high state and low state is referred to as capture and emission time, respectively. The average capture and emission time is referred to as  $\tau_c$  and  $\tau_e$ , respectively.

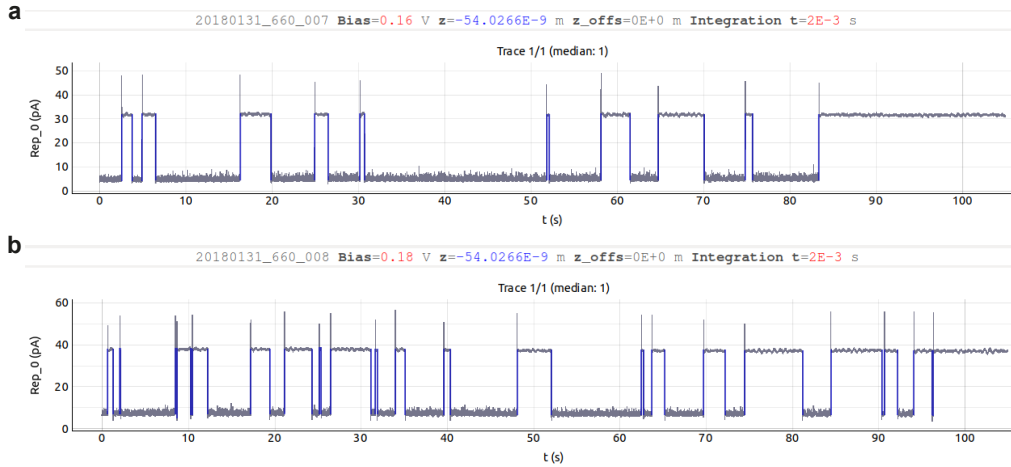


**Figure 8.8 | Random telegraph noise signal.** The spectra show the tunneling current over time recorded at a fixed tip-position that is marked in Figure 8.7b.<sup>145</sup> **a)**  $V_s = +0.16$  V. **b)**  $V_s = +0.18$  V.

Generally, the RTN signals were observed for both positive and negative sample bias voltage; the higher the bias (positive or negative) the more switching events occurred. The dependence of the switching frequency on the tunneling current is not linear. A slightly higher  $\text{O}_2^-$  coverage similar to the coverage shown in Figure 8.6 resulted in multiple levels in the RTN signals, see Figure A.5.

It should be noted that the direct correlation between a position shift of a single  $\text{O}_2^-$  and the high state and low state of the RTN signal in the tunneling current as shown in Figures 8.7 and 8.8 was an exception. For the majority of measured RTN signals it was impossible to establish such a connection. Therefore it can not be stated that a position shift of a  $\text{O}_2^-$  is necessary for the occurrence of a low- and high-conductance state. However, the presence of  $\text{O}_2^-$  is necessary since the RTN was never observed on the pristine surface.

Table 8.1 shows temperature-dependent average capture and emission times of the RTN signals obtained for positive and negative sample bias voltage; the measurement

position and the signals are shown in the appendix in Figures A.6 to A.8. For negative bias  $\tau_c$  decreases with increasing temperature from 0.8 to 0.13 s;  $\tau_e$  and the times for positive bias did not show such clear trends, except that the switching frequency increased with increasing temperature, *i.e.*, the sum of  $\tau_c$  and  $\tau_e$  became smaller. The rather weak dependence of  $\tau_c + \tau_e$  on temperature suggests that the switching is not only thermally activated. It should be noted that increasing the temperature of the STM/AFM head resulted in drift that made it difficult to keep the position of the tip (tip-sample distance and lateral position) constant; the drift also limits the measurement time and thus the switching events of which a sufficient number is required for statistical analysis.

$T$ [K]	$V_s = +0.19$ V			$V_s = -0.17$ V		
	$\tau_c$ [s]	$\tau_e$ [s]	$\tau_c + \tau_e$ [s]	$\tau_c$ [s]	$\tau_e$ [s]	$\tau_c + \tau_e$ [s]
4.8	-	-	-	0.8	0.04	0.84
5.8	0.08	0.26	0.34	0.47	0.26	0.73
6.8	0.05	0.21	0.26	-	-	-
8.8	0.01	0.25	0.26	0.31	0.21	0.52
11.1	0.05	0.04	0.09	0.13	0.27	0.40

**Table 8.1 | Temperature-dependent average capture and emission times.** Times were measured for positive and negative sample bias voltage ( $V_s$ ).<sup>145</sup> The signals are shown in Figures A.7 and A.8.

### 8.3 Discussion

The observation of thin lines in the tunneling-current images of the as-cleaved surface raises the question about the cause for these lines. Since no obvious explanation can be stated, it is instructive to review cases where similar features were observed in STM. The scattering of surface states at steps<sup>146</sup> or point defects<sup>147</sup> that disrupt a periodic potential leads to interference between reflected and incident waves resulting in a standing wave. However, the thin lines on  $\text{Ca}_3\text{Ru}_2\text{O}_7$  do not resemble regular oscillations of the local density of states as expected for a standing wave. Charge manipulation of donors<sup>148</sup> or acceptors<sup>149</sup> in semiconductors or wide-gap oxides<sup>150</sup> by tip-induced band bending leads to ring-like features in  $dI/dV$  images. However, on  $\text{Ca}_3\text{Ru}_2\text{O}_7$  the thin lines are observed directly in the tunneling current images. A work function difference between tip and sample leads to tip-induced band bending

in semiconductors. On InAs(110) the tip-induced downward band bending results in tip-induced states in the band gap, a so-called quantum dot.<sup>151</sup> The work function of  $\text{Ca}_3\text{Ru}_2\text{O}_7$  is lower than the work function of the tip (see Chapter 7) which results in upward band bending; therefore a tip-induced quantum dot is not expected. However, the discrete states of a quantum dot could explain the observation of states at different energies in the  $dI/dV$  spectra.  $\text{Ca}_3\text{Ru}_2\text{O}_7$  has a quasi-two-dimensional metallic ground state<sup>40</sup> that can be interpreted as a confinement of carriers in  $c$  direction; the samples contain Ti impurities (see Chapter 3) that are known to act as strong scatterers and might cause an additional confinement in  $a$  and  $b$  direction which is necessary for the formation of a quantum dot. The meandering pattern of some of the thin lines are strikingly similar to the paths of drift states on InAs(110).<sup>152</sup> These paths were interpreted as contour lines of a potential landscape. Indeed, indications of a disordered potential<sup>153</sup> in  $\text{Ca}_3\text{Ru}_2\text{O}_7$  were observed (Figure 8.7); the disordered potential could be caused by the Ti impurities.

In metal-oxide-semiconductor transistors RTN signals are observed in the source-drain current.<sup>144,154,155</sup> The signals are attributed to charge trapping at defects that are located in the oxide that insulates the gate from the channel; the capture or emission of a unit charge at a defect electrostatically modulates the channel width thus resulting in discrete changes of the source-drain current. The discrete changes of the tunneling-current on  $\text{Ca}_3\text{Ru}_2\text{O}_7$  could hint at a similar mechanism, although it is not clear where a charge could be trapped and how this would exactly cause the change in conductance. The RTN signals were only observed at low temperatures from 4.8 K to at least 11.1 K (but not above 48 K) in combination with adsorbed  $\text{O}_2^-$ . According to calculations<sup>87</sup> the electron that is transferred to the  $\text{O}_2^-$  originates from the Ru of the closest  $\text{RuO}_6$  octahedron (see Chapter 7). The resulting  $\text{Ru}^{5+}$  “defect” might be able to catch an electron, but the observed conductance changes are not centered around the  $\text{O}_2^-$  (Figure 8.6) as one would expect in this case. For the same reason it is unlikely that the  $\text{O}_2^-$  itself acts as the charge trap. This leaves the Ti impurities and the related hypothetical quantum dot (see above) as possible trap sites that are “activated” by an influence of the adsorbed  $\text{O}_2^-$  on the electronic structure; this influence might be caused by local band bending due to the negative charge of the  $\text{O}_2^-$  or the missing charge on the  $\text{Ru}^{5+}$  species and the related contraction of the  $\text{RuO}_6$  octahedron.<sup>91</sup>

## 8.4 Summary

Thin lines in tunneling-current images of the as-cleaved surface were observed at 4.8 K. The lines have open or closed paths and the same line can appear both brighter and darker than the background along its path. The locations and paths of the lines are not exactly correlated to subsurface defects. The diameter (closed path) or curvature radius (open path) of the lines depends on the sample bias voltage and the tip-sample distance.

The presence of adsorbed  $\text{O}_2^-$  resulted in sudden, locally confined changes of the conductivity. Measuring the tunneling-current over time at a fixed tip position revealed a Random Telegraph Noise signal switching between two discrete tunneling-current levels. At increased  $\text{O}_2^-$  coverage multiple levels were observed in the RTN signal. The switching frequency and the times spent in the low state and high state depend on temperature and bias.

The cause for the thin lines and the RTN signals is unclear. Both effects are only observed at temperatures below the metal to insulator transition at  $T_{\text{MI}} = 48$  K. The quasi-two-dimensional ground state of  $\text{Ca}_3\text{Ru}_2\text{O}_7$  and Ti impurities are suspected to be involved in the mechanism responsible for the effects.





# Chapter 9

## Conclusion

At the beginning of the present thesis nothing was known about the surface chemistry of  $\text{Ca}_3\text{Ru}_2\text{O}_7$ . As a first important result it can be stated that the CaO-terminated (001) surface is highly reactive towards CO and  $\text{H}_2\text{O}$ . A similar reactivity towards these molecules was found on the SrO-terminated (001) surface of the related strontium ruthenates.<sup>13</sup> CO adsorbs as a strongly bound chemisorbed Ru-COO species on both, calcium and strontium ruthenate, which indicates a high reactivity of AO-terminated surfaces of Ru-based perovskite oxides towards CO in general.

At low coverages water adsorbs exclusively dissociatively on  $\text{Ca}_3\text{Ru}_2\text{O}_7(001)$  and forms different OH overlayers until a full layer of hydroxyls covers the complete surface. The OH overlayers show a pronounced ordering of the dissociation fragments, caused by inequivalent adsorption sites in the surface unit cell. The inequivalence originates from the distorted oxygen sublattice consisting of the apical oxygen atoms of the underlying rotated and tilted  $\text{RuO}_6$  octahedra. On the related strontium ruthenates, where the  $\text{RuO}_6$  octahedra are not tilted, a mixed dissociative and molecular adsorption was observed. This demonstrates the influence of octahedral rotation and tilt on the surface reactivity of perovskites and that the engineering of these structural elements (*e.g.*, by utilizing strain, piezoelectricity or ferroelectricity) could be useful for tuning the surface chemistry of perovskite oxides.

The activation energy of the  $(\text{OH})_{\text{ads}}$  hopping on  $\text{Sr}_2\text{RuO}_4(001)$  was measured in the present thesis to complement the research done in the course of the thesis of Bernhard Stöger.<sup>13</sup> The experimental confirmation of the theoretically-predicted, constricted motion of the  $(\text{OH})_{\text{ads}}$  fragment<sup>52</sup> raises confidence in computational studies of water adsorption. No such dynamic behaviour of the dissociation fragments was observed on  $\text{Ca}_3\text{Ru}_2\text{O}_7(001)$  as the tilted  $\text{RuO}_6$  octahedra render the Ca-Ca bridge

sites inequivalent for the  $(\text{OH})_{\text{ads}}$ , thus preventing the hopping to neighbouring sites.

Molecular oxygen adsorbs as  $\text{O}_2^-$  and forms a full monolayer on  $\text{Ca}_3\text{Ru}_2\text{O}_7(001)$ . The negative charge state of the molecules is evident in Kelvin Probe Force Microscopy and X-ray Photoelectron Spectroscopy. The advantages of a combined STM and nc-AFM approach in case of adsorbates sensitive to electric field or tunnelling current were demonstrated; as single superoxo species are strongly influenced by the STM tip. No dopants, defects, or low-coordinated sites are necessary to facilitate the activation of  $\text{O}_2$  on the  $\text{Ca}_3\text{Ru}_2\text{O}_7(001)$  surface as the charge stems from the subsurface  $\text{RuO}_2$  layer. Only preliminary results were obtained for  $\text{O}_2$  adsorption on  $\text{Sr}_3\text{Ru}_2\text{O}_7(001)$  in the thesis of Bernhard Stöger<sup>13</sup>. Future experiments using the now available nc-AFM could deliver new results, which would allow a comparison with the results on  $\text{Ca}_3\text{Ru}_2\text{O}_7(001)$ .

Rather unexpected, intriguing electronic effects were encountered on the as-cleaved and  $\text{O}_2^-$  covered surfaces of  $\text{Ca}_3\text{Ru}_2\text{O}_7$  below the metal-to-insulator transition temperature of 48 K. At this point it can only be speculated that the cause for the observed thin lines and the RTN signals lies in the highly correlated and exotic electronic structure of  $\text{Ca}_3\text{Ru}_2\text{O}_7$ . Further research will be necessary to understand these effects.

# Appendix A

## Supplement

### A.1 Supplementary Figures

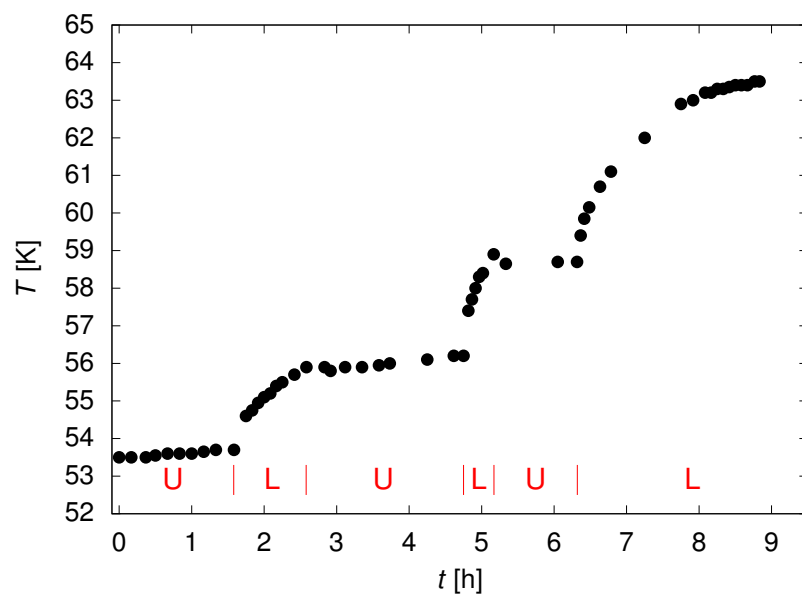
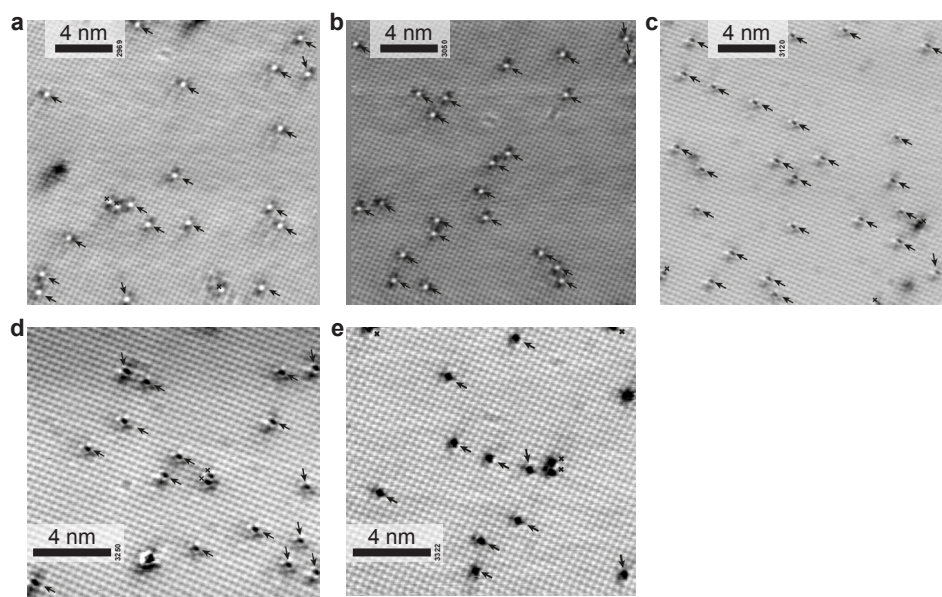
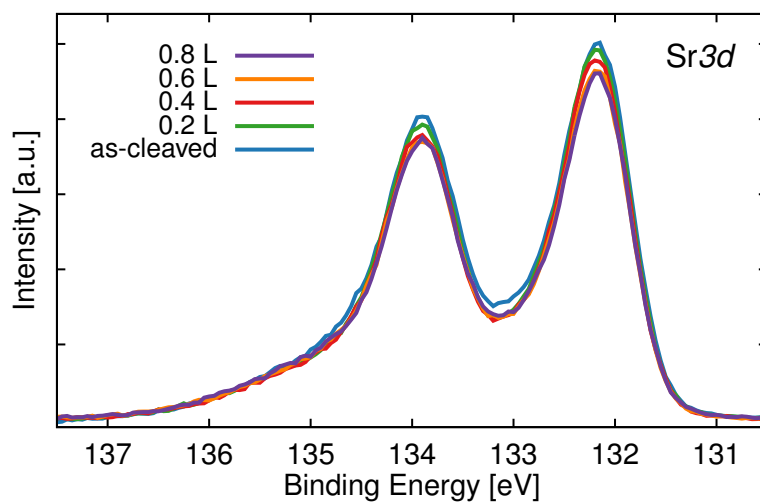


Figure A.1 | Temperature of the STM-head against time after stopping the pumping of the LN<sub>2</sub> cryostat. The STM-head was locked (“L”) and unlocked (“U”) several times.



**Figure A.2 | a-e)** Single frames of movies M3 to M6, respectively, showing the evaluated (*arrows*) and ignored (*crosses*)  $(\text{OH})_{\text{ads}}$ .



**Figure A.3 | Sr3d XPS spectra of increasing water dose at 140 K.** The legend states the cumulative dose. (Monochromatized Al  $K\alpha$ .)

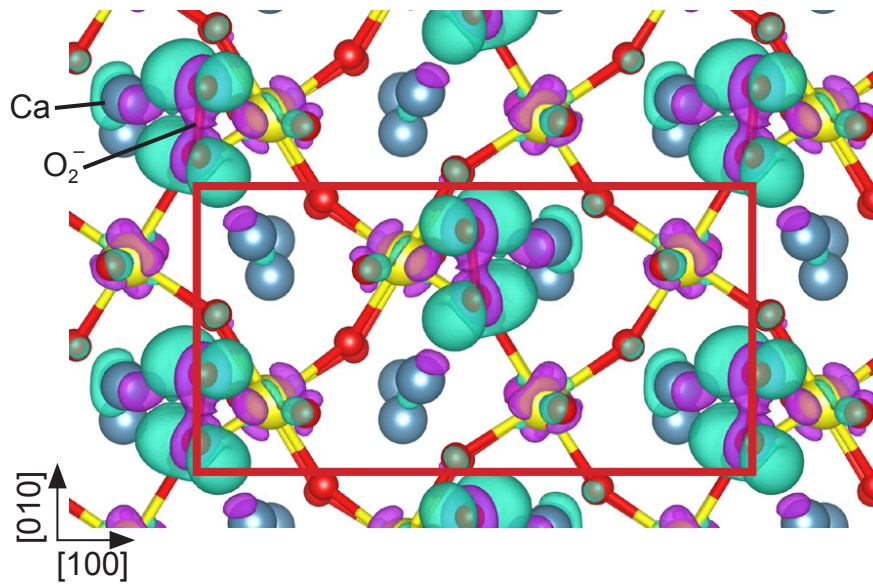


**Figure A.4 | Charge density difference plot<sup>87,91</sup> of the  $(2 \times 1)$   $\text{O}_2^-$  overlayer for the insulating substrate phase (HSE06). Top view; Ca – blue, Ru – yellow, O – red. Charge is transferred to and from the *turquoise* and *violet* areas, respectively.**

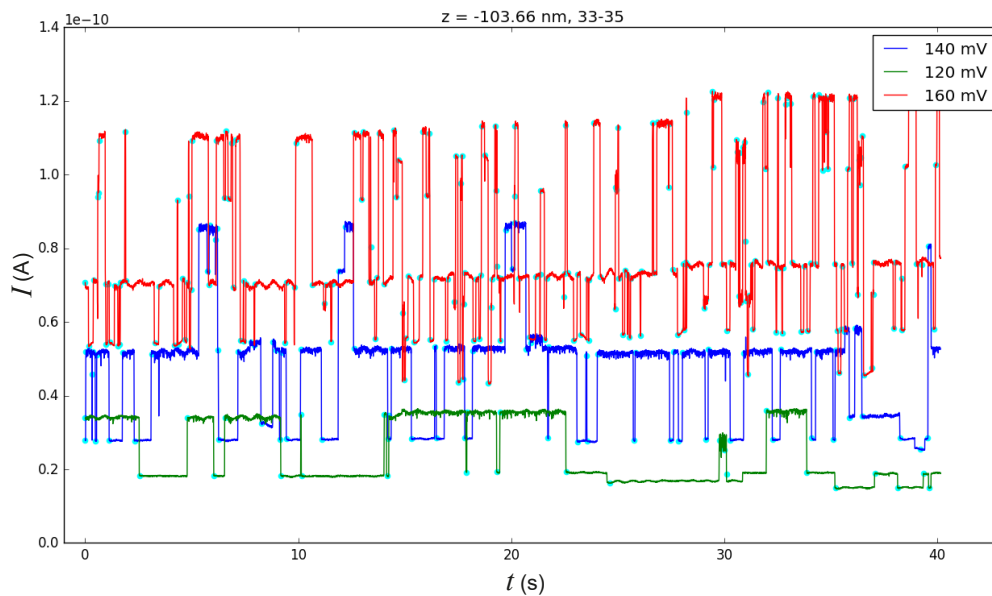


**Figure A.5 | RTN signals with multiple levels.** Measured on a sample with an  $\text{O}_2^-$  coverage similar to the coverage shown in Figure 8.6. With increasing sample bias voltage the switching frequency increases and the signal spends increasing times at higher levels.

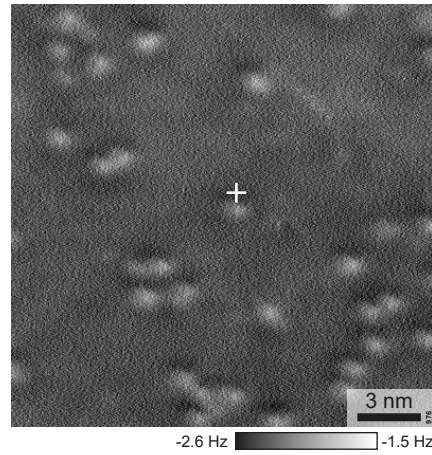


**Figure A.6** | AFM image showing adsorbed  $\text{O}_2^-$  as bright dots. The cross marks the measurement location of the RTN signals shown in Figures A.7 and A.8. AFM parameters:  $A = 500 \text{ pm}$ ,  $V_s = -0.05 \text{ V}$ ,  $T_s = 4.8 \text{ K}$ .

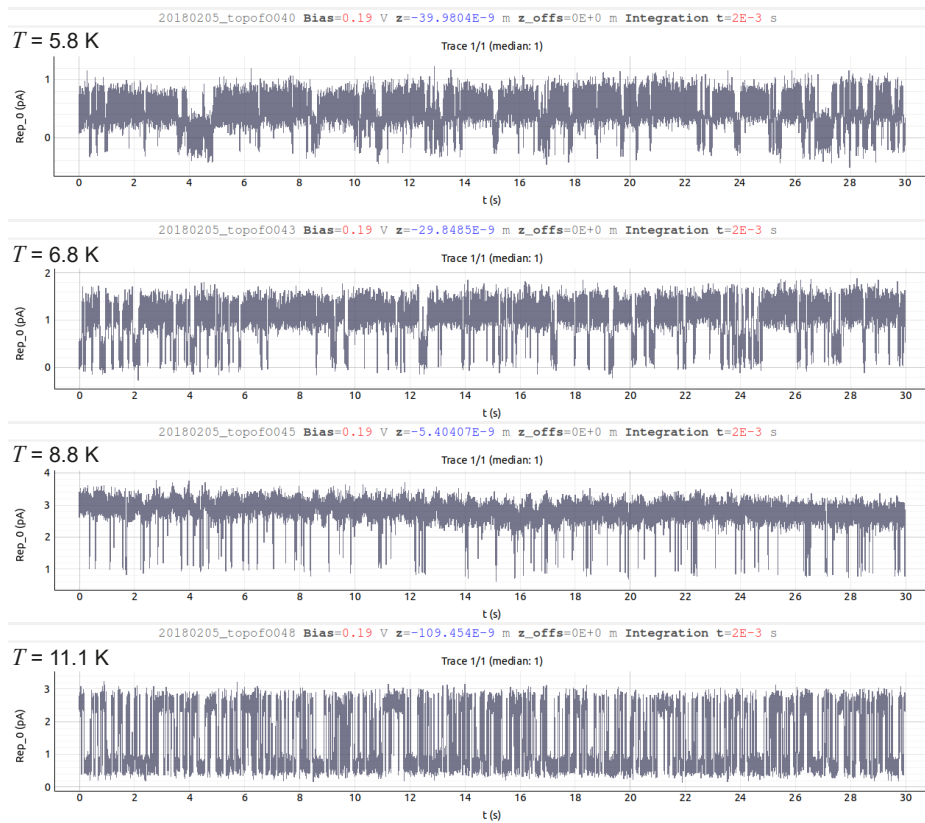


**Figure A.7** | RTN signals at positive sample bias voltage for different temperatures. All signals were measured at a sample bias voltage of  $+0.19 \text{ V}$ .<sup>145</sup> See Table 8.1 for average capture and emission times.

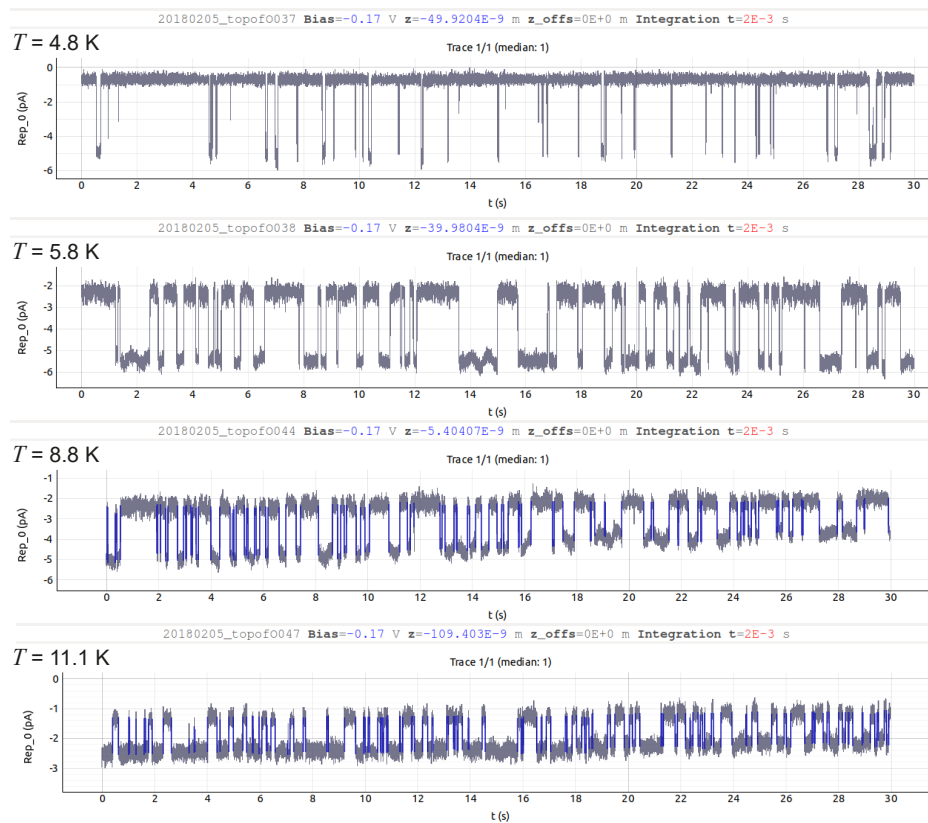


**Figure A.8 | RTN signals at negative sample bias voltage for different temperatures.** All signals were measured at a sample bias voltage of  $-0.17$  V.<sup>145</sup> See Table 8.1 for average capture and emission times.

## A.2 Supplementary Tables

$j$	$m_j$	$a_j$	$j$	$m_j$	$a_j$	$j$	$m_j$	$a_j$
1	2	19	14	0	18	27	0	22
2	1	19	15	0	18	28	0	23
3	1	19	16	0	18	29	1	23
4	1	19	17	0	18	30	1	22
5	1	18	18	0	18	31	2	21
6	1	18	19	0	18	32	0	21
7	1	19	20	0	20	33	0	21
8	0	19	21	0	20	34	2	21
9	0	19	22	0	20	35	1	21
10	0	18	23	1	21	36	1	21
11	0	18	24	0	21	37	0	21
12	1	17	25	1	21	38	1	21
13	0	18	26	0	22	39	0	21

**Table A.1** | Observed hops and evaluated  $\text{OH}_{\text{ads}}$  groups for every frame of STM movie M1.  $j$  – frame number,  $m_j$  – number of hops in frame  $j$ ,  $a_j$  – number of observed  $(\text{OH})_{\text{ads}}$  in frame  $j$ .

Configuration	Slab size [unit cells]	$\text{H}_2\text{O}$ molecules	Coverage [ML]	O1s shift [eV]
Molecular	$1 \times 1 \times 0.5$	1	0.5	3.79
B1O1	$3 \times 3 \times 0.5$	1	0.06	1.77
$(1 \times 3)$	$1 \times 3 \times 0.5$	4	0.67	1.57
$(1 \times 1)$	$1 \times 1 \times 0.5$	2	1.0	1.23

**Table A.2** | Calculated O1s BE shifts for  $\text{H}_2\text{O}$  on  $\text{Ca}_3\text{Ru}_2\text{O}_7(001)$ .<sup>87</sup> O1s core level shifts of molecular and dissociated  $\text{H}_2\text{O}$ ; referenced to the O1s level in the  $\text{RuO}_2$  plane.



Computational method	Adsorption energy [eV]
PBE	0.93
PBE+U (U – J = 4 eV)	0.68
vdW-DF	1.19
HSE06	0.59
RPA	0.72

**Table A.3 | DFT adsorption energies<sup>87</sup> of  $\text{O}_2^-$  on  $\text{Ca}_3\text{Ru}_2\text{O}_7(001)$ .** Adsorption energy per molecule of the  $(2 \times 1)$  overlayer obtained at different levels of theory. The insulating phase was modelled by an additional on-site interaction<sup>156</sup> (U – J = 4 eV) added to the Ru d-states. The vdW contributions amount to approximately 0.27 eV.

### A.3 Electronic Supplement

Movie	Short description	Link
M1	(OH) <sub>ads</sub> hopping/Sr <sub>2</sub> RuO <sub>4</sub>	<a href="#">M1<sup>89</sup></a>
M2	(OH) <sub>ads</sub> hopping/Sr <sub>2</sub> RuO <sub>4</sub>	<a href="#">M2<sup>89</sup></a>
M3	(OH) <sub>ads</sub> hopping/Sr <sub>2</sub> RuO <sub>4</sub>	<a href="#">M3<sup>89</sup></a>
M4	(OH) <sub>ads</sub> hopping/Sr <sub>2</sub> RuO <sub>4</sub>	<a href="#">M4<sup>89</sup></a>
M5	(OH) <sub>ads</sub> hopping/Sr <sub>2</sub> RuO <sub>4</sub>	<a href="#">M5<sup>89</sup></a>
M6	(OH) <sub>ads</sub> hopping/Sr <sub>2</sub> RuO <sub>4</sub>	<a href="#">M6<sup>89</sup></a>
M7	(OH) <sub>ads</sub> hopping/Sr <sub>2</sub> RuO <sub>4</sub>	<a href="#">M7<sup>89</sup></a>
M8	(OH) <sub>ads</sub> hopping/Sr <sub>2</sub> RuO <sub>4</sub>	<a href="#">M8<sup>89</sup></a>
O2.1	Moving domain boundaries O <sub>2</sub> <sup>-</sup> /Ca <sub>3</sub> Ru <sub>2</sub> O <sub>7</sub>	<a href="#">O2.1.gif*</a>
O2.2	Diffusing O <sub>2</sub> <sup>-</sup> /Ca <sub>3</sub> Ru <sub>2</sub> O <sub>7</sub>	<a href="#">O2.2<sup>91</sup></a>

**Table A.4 | List of the STM movies available as electronic supplement.** \*This file is available from the author upon request.

# Appendix B

## List of all STM/AFM files

**Table B.1** | List of STM/AFM files used in the figures.

<b>Figure</b>		<b>File number</b>	<b>Folder</b>
Figure 3.2	a	3175	Ca3Ru2O7_2015
	b	019	CRO327_QPlus_2016b
Figure 3.3	a	2508	Ca3Ru2O7_2014
	b	3175	Ca3Ru2O7_2015
Figure 3.4	a	1313	Ca3Ru2O7_2015
	b	1181	Ca3Ru2O7_2015
Figure 3.5	a	1007	Ca3Ru2O7_2015
	b	190	CRO327_QPlus_2016b
Figure 4.1	a	2725	Ca3Ru2O7_2014
	b	2737	Ca3Ru2O7_2014
Figure 4.5	a	2762	Ca3Ru2O7_2014
Figure 4.6	a	2798	Ca3Ru2O7_2014
Figure 4.7	a	2799	Ca3Ru2O7_2014
	b	2829	Ca3Ru2O7_2014
	c	2842	Ca3Ru2O7_2014
	d	2845	Ca3Ru2O7_2014
Figure 4.8	a	2853	Ca3Ru2O7_2014
	b	2859	Ca3Ru2O7_2014
	c	2866	Ca3Ru2O7_2014
	d	2870	Ca3Ru2O7_2014

*Continued on next page*

Table B.1 – *Continued from previous page*

	e	2878	Ca3Ru2O7_2014
	f	2881	Ca3Ru2O7_2014
Figure 4.9		1521	Ca3Ru2O7_2016
Figure 4.11	a	1057	Ca3Ru2O7_2016
	b	1056	Ca3Ru2O7_2016
	c	1120	Ca3Ru2O7_2016
	d	1198	Ca3Ru2O7_2016
	e	1188	Ca3Ru2O7_2016
	f	1190	Ca3Ru2O7_2016
Figure 5.1	c	1819	Sr2Ru1O4_2014
Figure 5.2	b	8647-69	Sr3Ru2O7
Figure 5.5	c	1818	Sr2Ru1O4_2014
Figure 5.6	a	1670	Sr2Ru1O4_2014
	b	1676	Sr2Ru1O4_2014
Figure 6.1	a	1296	Ca3Ru2O7_2015
	b	1304	Ca3Ru2O7_2015
Figure 6.2	a	1304	Ca3Ru2O7_2015
Figure 6.3	a	1360	Ca3Ru2O7_2015
	b	1394	Ca3Ru2O7_2015
Figure 6.4	a	1256	Ca3Ru2O7_2015
	b	1258	Ca3Ru2O7_2015
Figure 6.5	a	1462	Ca3Ru2O7_2015
Figure 7.1		2340	Ca3Ru2O7_2015
Figure 7.2	a	114	CRO327_QPlus_2016b
	b	117	CRO327_QPlus_2016b
	c	119	CRO327_QPlus_2016b
	d	120	CRO327_QPlus_2016b
Figure 7.4	a	2372	Ca3Ru2O7_2015
	b	2385	Ca3Ru2O7_2015
	c	2410	Ca3Ru2O7_2015
	d	2416	Ca3Ru2O7_2015

*Continued on next page*

Table B.1 – *Continued from previous page*

Figure 7.5		2451	Ca3Ru2O7_2015
Figure 7.7	a	2451	Ca3Ru2O7_2015
	b	2516	Ca3Ru2O7_2015
Figure 7.8		092	CRO327_QPlus_2016a
Figure 8.1		041	CRO327_QPlus_2016b
Figure 8.2		035	CRO327_QPlus_2016b
Figure 8.3		043-050	CRO327_QPlus_2016b
Figure 8.4		493-499	CRO327_QPlus_2016b
Figure 8.6	a	115	CRO327_QPlus_2016b
	b	119	CRO327_QPlus_2016b
Figure 8.7	a	653	CRO327_QPlus_2016b
	b	659	CRO327_QPlus_2016b
Figure A.6		976	CRO327_QPlus_2016b
Figure A.2		see images	Sr2Ru1O4_2014

# List of Figures

1.1	The ideal perovskite oxide structure and the d orbitals . . . . .	3
1.2	The layered structure of Ruddlesden-Popper compounds . . . . .	5
1.3	The structure of $\text{Ca}_3\text{Ru}_2\text{O}_7$ . . . . .	6
1.4	Magnetic phases of $\text{Ca}_3\text{Ru}_2\text{O}_7$ . . . . .	7
2.1	The sample assembly . . . . .	14
2.2	The concept of Scanning Tunneling Microscopy . . . . .	15
2.3	The qPlus sensor. Schematic and photo. . . . .	21
2.4	Energy diagram of X-ray Photoelectron Spectroscopy . . . . .	22
3.1	DFT model of the cleaved $\text{Ca}_3\text{Ru}_2\text{O}_7(001)$ surface . . . . .	24
3.2	STM and AFM image of the pristine $\text{Ca}_3\text{Ru}_2\text{O}_7(001)$ surface . . . . .	25
3.3	Point defects of the as-cleaved surface in STM . . . . .	26
3.4	STM images of line and area defect . . . . .	28
3.5	STM and AFM image of surfaces of unsuccessful cleavings . . . . .	29
4.1	STM images of a low dose of $\text{H}_2\text{O}$ on $\text{Ca}_3\text{Ru}_2\text{O}_7(001)$ . . . . .	33
4.2	DFT model for water adsorption on $\text{Ca}_3\text{Ru}_2\text{O}_7(001)$ . . . . .	34
4.3	DFT models of different monomer adsorption configurations . . . . .	35
4.4	STM simulation of the dissociated monomer and DFT model of the ( $2 \times 1$ ) overlayer . . . . .	36
4.5	STM image and Fourier transform of the $c(2 \times 6)$ overlayer . . . . .	37
4.6	STM image and simulation of the ( $1 \times 3$ ) overlayer . . . . .	38
4.7	STM images of the effect of increasing water dose and the ( $1 \times 1$ ) overlayer . . . . .	39
4.8	STM images of the ( $1 \times 1$ ) overlayer, molecular water and gradual desorption . . . . .	41
4.9	STM image of a sample after annealing at 330 K . . . . .	43

4.10	O1s XPS spectra of the as-cleaved surface and OH-overlayers . . . . .	44
4.11	STM images of oxygen vacancies and the interaction with water on $\text{Ca}_3\text{Ru}_2\text{O}_7(001)$ . . . . .	45
5.1	The $\text{Sr}_3\text{Ru}_2\text{O}_7$ structure and low dose of water in STM . . . . .	52
5.2	DFT model and STM images of the dissociated water monomer . . . . .	52
5.3	Lifetime distributions of the STM movies M3 to M6 . . . . .	55
5.4	Arrhenius plot of the average lifetimes . . . . .	57
5.5	DFT model and STM image of the preferred dimer adsorption sites . . . . .	58
5.6	Full monolayer of water in STM . . . . .	59
5.7	O1s XPS spectra of increasing water dose at 140 K . . . . .	60
5.8	Water multilayers in the O1s XPS . . . . .	60
6.1	Initial adsorption of CO in STM . . . . .	64
6.2	CO adsorption – registry of adsorption site . . . . .	64
6.3	CO manipulation by the STM tip . . . . .	65
6.4	STM images of the transformation of the adsorbed CO precursor into the chemisorbed species . . . . .	66
6.5	STM images of the chemisorbed species. . . . .	67
6.6	DFT model of the CO precursor configuration . . . . .	68
6.7	DFT model of the chemisorbed Ru-COO configuration . . . . .	69
7.1	Interaction between adsorbates and the STM tip after exposure to a low dose of $\text{O}_2$ . . . . .	73
7.2	Interactions between adsorbates and the STM/AFM-tip for varying sample bias voltages . . . . .	74
7.3	DFT model of $\text{O}_2^-$ adsorbed on $\text{Ca}_3\text{Ru}_2\text{O}_7(001)$ . . . . .	75
7.4	Increasing coverage of $\text{O}_2^-$ in STM. . . . .	76
7.5	STM image of the $(2 \times 1)$ $\text{O}_2^-$ overlayer. . . . .	77
7.6	DFT model and STM simulation of the $(2 \times 1)$ overlayer . . . . .	78
7.7	The $\text{O}_2^-$ -saturated surface and tip-induced desorption. . . . .	79
7.8	AFM image of a partially $\text{O}_2^-$ -covered sample . . . . .	80
7.9	KPFM on Cu(110) . . . . .	80
7.10	KPFM of $\text{O}_2^-$ on $\text{Ca}_3\text{Ru}_2\text{O}_7$ . . . . .	81
7.11	XPS of $\text{O}_2^-$ on $\text{Ca}_3\text{Ru}_2\text{O}_7$ . . . . .	82

8.1	Thin lines on the as-cleaved surface . . . . .	88
8.2	Simultaneous, constant-height STM and AFM image of the thin lines	89
8.3	Bias-dependence of concentric lines in empty and filled states . . . . .	90
8.4	Influence of the tip-sample distance on concentric lines . . . . .	91
8.5	Tunneling Spectroscopy . . . . .	92
8.6	Sudden conductance changes . . . . .	94
8.7	Conductance related to the position of a superoxo species . . . . .	95
8.8	Random telegraph noise signal . . . . .	96
A.1	Temperature of the STM-head against time after stopping the pump- ing of the LN <sub>2</sub> cryostat . . . . .	103
A.4	Charge density difference plot of the (2 × 1) O <sub>2</sub> <sup>-</sup> overlayer . . . . .	105
A.5	RTN signals with multiple levels . . . . .	105
A.6	AFM image showing adsorbed O <sub>2</sub> <sup>-</sup> as bright dots . . . . .	106
A.7	RTN signals at positive sample bias voltage for different temperatures	106
A.8	RTN signals at negative sample bias voltage for different temperatures	107

## List of Tables

3.1	Impurity concentrations measured by LA-ICP-MS . . . . .	27
4.1	Bridge site to surface oxygen distances . . . . .	34
4.2	Adsorption energies and geometry details of the monomer configura- tions . . . . .	36
4.3	Adsorption energy and nominal coverage for the OH overlayers . . . . .	40
4.4	Maximum chamber pressures and times measured during the gradual water desorption . . . . .	42
5.1	STM movie details and measured average lifetimes . . . . .	56
5.2	Comparison of results obtained from STM movies with different frame aquisition times . . . . .	56



---

8.1	Temperature-dependent average capture and emission times . . . . .	97
A.1	Observed hops and evaluated OH <sub>ads</sub> groups for every frame of STM movie M1 . . . . .	108
A.2	Calculated O1s BE shifts for H <sub>2</sub> O on Ca <sub>3</sub> Ru <sub>2</sub> O <sub>7</sub> (001) . . . . .	108
A.3	DFT adsorption energies of O <sub>2</sub> <sup>-</sup> on Ca <sub>3</sub> Ru <sub>2</sub> O <sub>7</sub> (001) . . . . .	109
A.4	List of the STM movies available as electronic supplement . . . . .	110
B.1	List of STM/AFM files used in the figures. . . . .	111



# References

1. Peña, M. A. & Fierro, J. L. G. Chemical structures and performance of perovskite oxides. *Chemical Reviews* **101**, 1981–2017 (2001).
2. Kilner, J. A. & Burriel, M. Materials for Intermediate-Temperature Solid-Oxide Fuel Cells. *Annual Review of Materials Research* **44**, 365–393 (2014).
3. Adler, S. B., Lane, J. A. & Steele, B. C. H. Electrode Kinetics of Porous Mixed - Conducting Oxygen Electrodes. *Journal of the Electrochemical Society* **143**, 3554–3564 (1996).
4. Tarancon, A., Burriel, M., Santiso, J., Skinner, S. J. & Kilner, J. A. Advances in layered oxide cathodes for intermediate temperature solid oxide fuel cells. *J. Mater. Chem.* **20**, 3799–3813 (2010).
5. Gorte, R. & Vohs, J. Catalysis in Solid Oxide Fuel Cells. *Annual Review of Chemical and Biomolecular Engineering* **2**, 9–30 (2011).
6. Graves, C., Ebbesen, S. D., Jensen, S. H., Simonsen, S. B. & Mogenssen, M. B. Eliminating degradation in solid oxide electrochemical cells by reversible operation. *Nature Materials* **14**, 239–244 (2014).
7. McDaniel, A. H., Miller, E. C., Arifin, D., Ambrosini, A., Coker, E. N., O'Hayre, R., Chueh, W. C. & Tong, J. Sr- and Mn-doped  $\text{LaAlO}_{3-\delta}$  for solar thermochemical  $\text{H}_2$  and  $\text{CO}$  production. *Energy Environ. Sci.* **6**, 2424–2428 (2013).
8. Suntivich, J., May, K. J., Gasteiger, H. A., Goodenough, J. B. & Shao-Horn, Y. A Perovskite Oxide Optimized for Oxygen Evolution Catalysis from Molecular Orbital Principles. *Science* **334**, 1383–1385 (2011).
9. Vojvodic, A. & Nørskov, J. K. Optimizing Perovskites for the Water-Splitting Reaction. *Science* **334**, 1355–1356 (2011).
10. Hayyan, M., Hashim, M. A. & Alnashef, I. M. Superoxide Ion: Generation and Chemical Implications. *Chemical Reviews* **116**, 3029–3085 (2016).

11. Rossmeisl, J., Qu, Z. W., Zhu, H., Kroes, G. J. & Nørskov, J. K. Electrolysis of water on oxide surfaces. *Journal of Electroanalytical Chemistry* **607**, 83–89 (2007).
12. Rupp, G. M., Opitz, A. K., Nenning, A., Limbeck, A. & Fleig, J. Real-time impedance monitoring of oxygen reduction during surface modification of thin film cathodes. *Nature Materials* **16**, 640–645 (2017).
13. Stöger, B. *Surface defects and adsorption on strontium ruthenates* PhD thesis (2014).
14. Benedek, N. A. & Fennie, C. J. Hybrid improper ferroelectricity: A mechanism for controllable polarization-magnetization coupling. *Physical Review Letters* **106**, 3–6 (2011).
15. Kimura, T., Ishihara, S., Shintani, H., Arima, T., Takahashi, K. T., Ishizaka, K. & Tokura, Y. Distorted perovskite with  $e_g^1$  configuration as a frustrated spin system. *Physical Review B* **68**, 060403 (2003).
16. Rini, M., Tobey, R., Dean, N., Itatani, J., Tomioka, Y., Tokura, Y., Schoenlein, R. W. & Cavalleri, A. Control of the electronic phase of a manganite by mode-selective vibrational excitation. *Nature* **449**, 72–74 (2007).
17. Kim, B. J., Yu, J., Koh, H., Nagai, I., Ikeda, S. I., Oh, S. J. & Kim, C. Missing xy-band fermi surface in 4d transition-metal oxide  $\text{Sr}_2\text{RhO}_4$ : Effect of the octahedra rotation on the electronic structure. *Physical Review Letters* **97**, 1–4 (2006).
18. Gomez, M. A., Griffin, M. A., Jindal, S., Rule, K. D. & Cooper, V. R. The effect of octahedral tilting on proton binding sites and transition states in pseudo-cubic perovskite oxides. *The Journal of Chemical Physics* **123**, 094703 (2005).
19. Han, J. W. & Yildiz, B. Enhanced one dimensional mobility of oxygen on strained  $\text{LaCo}_3(001)$  surface. *J. Mater. Chem.* **21**, 18983–18990 (2011).
20. Bhalla, A. S., Guo, R. Y. & Roy, R. The perovskite structure - a review of its role in ceramic science and technology. *Materials Research Innovations* **4**, 3–26 (2000).
21. Goldschmidt, V. M. Die Gesetze der Krystallochemie. *Naturwissenschaften* **14**, 477–485 (1926).

22. Halpern, J., Sinex, S. & Johnson, S. *3D Representation of Orbitals from LibreTexts Chemistry* Last visited on 25/4/2018. [https://chem.libretexts.org/Textbook\\_Maps/General\\_Chemistry\\_Textbook\\_Maps/Map%3A\\_Chemistry%3A\\_The\\_Central\\_Science\\_\(Brown\\_et\\_al.\)/06.\\_Electronic\\_Structure\\_of\\_Atoms/6.6%3A\\_3D\\_Representation\\_of\\_Orbitals](https://chem.libretexts.org/Textbook_Maps/General_Chemistry_Textbook_Maps/Map%3A_Chemistry%3A_The_Central_Science_(Brown_et_al.)/06._Electronic_Structure_of_Atoms/6.6%3A_3D_Representation_of_Orbitals).
23. Tokura, Y. & Nagaosa, N. Orbital Physics in Transition-Metal Oxides. *Science* **288**, 462–468 (2000).
24. Goodenough, J. B. Jahn-Teller phenomena in solids. *Annual Review of Materials Science* **28**, 1–27 (1998).
25. Imada, M., Fujimori, A. & Tokura, Y. Metal-insulator transitions. *Reviews of Modern Physics* **70**, 1039–1263 (1998).
26. Gerhold, S., Wang, Z., Schmid, M. & Diebold, U. Stoichiometry-driven switching between surface reconstructions on SrTiO<sub>3</sub>(001). *Surface science* **621**, L1–L4 (2014).
27. Chien, T. Y., Chakhalian, J., Freeland, J. W. & Guisinger, N. P. Cross-sectional scanning tunneling microscopy applied to complex oxide interfaces. *Advanced Functional Materials* **23**, 2565–2575 (2013).
28. Setvin, M., Reticcioli, M., Poelzleitner, F., Hulva, J., Schmid, M., Boatner, L. A., Franchini, C. & Diebold, U. Polarity compensation mechanisms on the perovskite surface KTaO<sub>3</sub>(001). *Science* **359**, 572–575 (2018).
29. Setvin, M. *et al.* in preparation. (2018).
30. Stöger, B., Hieckel, M., Mittendorfer, F., Wang, Z., Schmid, M., Parkinson, G. S., Fobes, D., Peng, J., Ortmann, J. E., Limbeck, A., Mao, Z., Redinger, J. & Diebold, U. Point defects at cleaved Sr<sub>n+1</sub>Ru<sub>n</sub>O<sub>3n+1</sub>(001) surfaces. *Physical Review B* **90**, 165438 (2014).
31. Ruddlesden, S. N. & Popper, P. New compounds of the K<sub>2</sub>NiF<sub>4</sub> type. *Acta Crystallographica* **10**, 538–539 (1957).
32. Beznosikov, B. V. & Aleksandrov, K. S. Perovskite-like crystals of the Ruddlesden-Popper series. *Crystallography Reports* **45**, 792–798 (2000).
33. Yoshida, Y., Ikeda, S.-I., Matsuhata, H., Shirakawa, N., Lee, C. & Katano, S. Crystal and magnetic structure of Ca<sub>3</sub>Ru<sub>2</sub>O<sub>7</sub>. *Physical Review B* **72**, 054412 (2005).

34. Cao, G., Abboud, K., McCall, S., Crow, J. E. & Guertin, R. P. Spin-charge coupling for dilute La-doped  $\text{Ca}_3\text{Ru}_2\text{O}_7$ . *Physical Review B* **62**, 998–1003 (2000).
35. Cao, G., DeLong, L. E. & Schlottmann, P. in *Frontiers of 4d- and 5d-Transition Metal Oxides* 179–214 (World Scientific Publishing Co. Pte. Ltd., 2013).
36. Cao, G., McCall, S., Crow, J. E. & Guertin, R. P. Observation of a Metallic Antiferromagnetic Phase and Metal to Nonmetal Transition in  $\text{Ca}_3\text{Ru}_2\text{O}_7$ . *Physical Review Letters* **78**, 1751–1754 (1997).
37. McCall, S., Cao, G., Crow, J. E., Harrison, N., Mielke, C. H., Lacerda, A. H. & Guertin, R. P. Metamagnetism of single crystal  $\text{Ca}_3\text{Ru}_2\text{O}_7$  in high magnetic fields. *Physica B* **246-247**, 144–148 (1998).
38. Bao, W., Mao, Z. Q., Qu, Z. & Lynn, J. W. Spin Valve Effect and Magnetoresistivity in Single Crystalline  $\text{Ca}_3\text{Ru}_2\text{O}_7$ . *Physical Review Letters* **100**, 247203 (2008).
39. Cao, G., Balicas, L., Xin, Y., Crow, J. E. & Nelson, C. S. Quantum oscillations, colossal magnetoresistance, and the magnetoelastic interaction in bilayered  $\text{Ca}_3\text{Ru}_2\text{O}_7$ . *Phys. Rev. B* **67**, 184405 (2003).
40. Yoshida, Y., Nagai, I., Ikeda, S.-I., Shirakawa, N., Kosaka, M. & Mōri, N. Quasi-two-dimensional metallic ground state of  $\text{Ca}_3\text{Ru}_2\text{O}_7$ . *Physical Review B* **69**, 220411 (2004).
41. Karpus, J. F., Gupta, R., Barath, H., Cooper, S. L. & Cao, G. Field-Induced Orbital and Magnetic Phases in  $\text{Ca}_3\text{Ru}_2\text{O}_7$ . *Physical Review Letters* **93**, 167205 (2004).
42. Liu, H., Yoon, S., Cooper, S., Cao, G. & Crow, J. Raman-scattering study of the charge and spin dynamics of the layered ruthenium oxide  $\text{Ca}_3\text{Ru}_2\text{O}_7$ . *Physical Review B* **60**, R6980–R6983 (1999).
43. Iliev, M. N., Jandl, S., Popov, V. N., Litvinchuk, A. P., Cmaidalka, J., Meng, R. L. & Meen, J. Raman spectroscopy of  $\text{Ca}_3\text{Ru}_2\text{O}_7$  : line assignment and electron scattering. *Physical Review B* **71**, 214305 (2005).
44. Bautista, A., Durairaj, V., Chikara, S., Cao, G., Ng, K.-W. & Gupta, A. A study of the Mott transition in  $\text{Ca}_3\text{Ru}_2\text{O}_7$  by tunneling spectroscopy. *Solid State Communications* **148**, 240–242 (2008).

- 
45. Liu, G.-Q. Mott transition and magnetic anisotropy in  $\text{Ca}_3\text{Ru}_2\text{O}_7$ . *Physical Review B* **84**, 235137 (2011).
  46. Ke, X., Peng, J., Singh, D. J., Hong, T., Tian, W., Dela Cruz, C. R. & Mao, Z. Q. Emergent electronic and magnetic state in  $\text{Ca}_3\text{Ru}_2\text{O}_7$  induced by Ti doping. *Physical Review B* **84**, 201102 (2011).
  47. Peng, J., Liu, J. Y., Gu, X., Zhou, G., Wang, W., Hu, J., Zhang, F. M. & Wu, X. S. Extremely large anisotropic transport caused by electronic phase separation in Ti-doped  $\text{Ca}_3\text{Ru}_2\text{O}_7$ . *Journal of Physics D: Applied Physics* **49**, 245004 (2016).
  48. Peng, J., Ke, X., Wang, G., Ortmann, J. E., Fobes, D., Hong, T., Tian, W., Wu, X. & Mao, Z. Q. From quasi-two-dimensional metal with ferromagnetic bilayers to Mott insulator with G-type antiferromagnetic order in  $\text{Ca}_3(\text{Ru}_{1-x}\text{Ti}_x)_2\text{O}_7$ . *Physical Review B* **87**, 085125 (2013).
  49. Lide, D. R., Data, S. R., Board, E. A., Baysinger, G., Chemistry, S., Library, C. E., Berger, L. I., Goldberg, R. N., Division, B., Kehiaian, H. V., Kuchitsu, K., Rosenblatt, G., Roth, D. L. & Zwillinger, D. CRC Handbook of Chemistry and Physics.
  50. Di Valentin, C., Ferullo, R., Binda, R. & Pacchioni, G. Oxygen vacancies and peroxo groups on regular and low-coordinated sites of MgO, CaO, SrO, and BaO surfaces. *Surface Science* **600**, 1147–1154 (2006).
  51. Hu, X. L., Carrasco, J., Klimeš, J. & Michaelides, A. Trends in water monomer adsorption and dissociation on flat insulating surfaces. *Physical chemistry chemical physics : PCCP* **13**, 12447–53 (2011).
  52. Carrasco, J., Illas, F. & Lopez, N. Dynamic Ion Pairs in the Adsorption of Isolated Water Molecules on Alkaline-Earth Oxide (001) Surfaces. *Physical Review Letters* **100**, 016101 (2008).
  53. Liu, P., Kendelewicz, T., Brown, G. E., Parks, G. A. & Pianetta, P. Reaction of water with vacuum-cleaved CaO(100) surfaces: an X-ray photoemission spectroscopy study. *Surface Science* **416**, 326–340 (1998).
  54. Zhao, X., Shao, X., Fujimori, Y., Bhattacharya, S., Ghiringhelli, L. M., Freund, H. J., Sterrer, M., Nilius, N. & Levchenko, S. V. Formation of water chains on CaO(001): What drives the 1D growth? *Journal of Physical Chemistry Letters* **6**, 1204–1208 (2015).

55. Fujimori, Y., Zhao, X., Shao, X., Levchenko, S. V., Nilius, N., Sterrer, M. & Freund, H. J. Interaction of Water with the CaO(001) Surface. *Journal of Physical Chemistry C* **120**, 5565–5576 (2016).
56. Oncáák, M., Włodarczyk, R. & Sauer, J. Hydration structures of MgO, CaO, and SrO (001) surfaces. *Journal of Physical Chemistry C* **120**, 24762–24769 (2016).
57. Kantorovich, L. & Gillan, M. Adsorption of atomic and molecular oxygen on the MgO(001) surface. *Surface Science* **374**, 373–386 (1997).
58. Che, M. & Tench, A. Characterization and Reactivity of Molecular Oxygen Species on Oxide Surfaces. *Advances in Catalysis* **32**, 1–148 (1983).
59. Yi, C., Xiang, S., Matthias, B., Joachim, S., Niklas, N. & Hans-Joachim, F. Adsorption, Activation, and Dissociation of Oxygen on Doped Oxides. *Angewandte Chemie International Edition* **52**, 11385–11387.
60. Solis, B. H., Cui, Y., Weng, X., Seifert, J., Schauer mann, S., Sauer, J., Shaikhutdinov, S. & Freund, H.-J. Initial stages of CO<sub>2</sub> adsorption on CaO: a combined experimental and computational study. *Phys. Chem. Chem. Phys.* **19**, 4231–4242 (2017).
61. Voigts, F., Bebensee, F., Dahle, S., Volgmann, K. & Maus-Friedrichs, W. The adsorption of CO<sub>2</sub> and CO on Ca and CaO films studied with MIES, UPS and XPS. *Surface Science* **603**, 40–49 (2009).
62. Giessibl, F. J. *Sensor for noncontact profiling of a surface* 2012. <https://www.google.com/patents/US20120131704>.
63. Majzik, Z., Setvín, M., Bettac, A., Feltz, A., Cháb, V. & Jelínek, P. Simultaneous current, force and dissipation measurements on the Si(111) 7 × 7 surface with an optimized qPlus AFM/STM technique. *Beilstein Journal of Nanotechnology* **3**, 249–259 (2012).
64. Setvín, M., Javorský, J., Turčinková, D., Matolínová, I., Sobotík, P., Kocán, P. & Ošťádal, I. Ultrasharp tungsten tips - characterization and nondestructive cleaning. *Ultramicroscopy* **113**, 152–157 (2012).



- 
65. Pavelec, J., Hulva, J., Halwidl, D., Bliem, R., Gamba, O., Jakub, Z., Brunbauer, F., Schmid, M., Diebold, U. & Parkinson, G. S. A multi-technique study of CO<sub>2</sub> adsorption on Fe<sub>3</sub>O<sub>4</sub> magnetite. *The Journal of Chemical Physics* **146**, 014701 (2017).
  66. Mao, Z., Maenoab, Y. & Fukazawa, H. Crystal growth of Sr<sub>2</sub>RuO<sub>4</sub>. *Materials Research Bulletin* **35**, 1813–1824 (2000).
  67. Binnig, G. & Rohrer, H. Scanning tunneling microscopy. *Surface Science* **126**, 236–244 (1982).
  68. Schmid, M. *Experimentelle Methoden der Oberflächenphysik* (Institute of Applied Physics, TU Wien, 2018).
  69. Tersoff, J. & Hamann, D. Theory and application for the scanning tunneling microscope. *Physical Review Letters* **50**, 1998 (1983).
  70. Tersoff, J. & Hamann, D. R. Theory of the scanning tunneling microscope. *Physical Review B* **31**, 805–813 (1985).
  71. Bardeen, J. Tunnelling from a Many-Particle Point of View. *Physical Review Letters* **6**, 57–59 (1961).
  72. Binnig, G., Quate, C. F. & Gerber, C. Atomic Force Microscope. *Physical Review Letters* **56**, 930–933 (1986).
  73. *Noncontact Atomic Force Microscopy* (eds Morita, S., Giessibl, F. J., Meyer, E. & Wiesendanger, R.) (Springer International Publishing, 2015).
  74. Giessibl, F. J. Forces and frequency shifts in atomic-resolution dynamic-force microscopy. *Physical Review B - Condensed Matter and Materials Physics* **56**, 16010–16015 (1997).
  75. Moll, N., Gross, L., Mohn, F., Curioni, A. & Meyer, G. The mechanisms underlying the enhanced resolution of atomic force microscopy with functionalized tips. *New Journal of Physics* **12**, 125020 (2010).
  76. Weymouth, A. J., Hofmann, T. & Giessibl, F. J. Quantifying molecular stiffness and interaction with lateral force microscopy. *Science* **343**, 1120–1122 (2014).
  77. Sader, J. E. & Jarvis, S. P. Accurate formulas for interaction force and energy in frequency modulation force spectroscopy. *Applied Physics Letters* **84**, 1801–1803 (2004).

78. Albrecht, T. R., Grütter, P., Horne, D. & Rugar, D. Frequency modulation detection using high-Q cantilevers for enhanced force microscope sensitivity. *Journal of Applied Physics* **69**, 668–673 (1991).
79. *Noncontact Atomic Force Microscopy* (eds Morita, S., Giessibl, F. J. & Wiesendanger, R.) (Springer Berlin Heidelberg, Berlin, Heidelberg, 2009).
80. Huber, F. & Giessibl, F. J. Low noise current preamplifier for qPlus sensor deflection signal detection in atomic force microscopy at room and low temperatures. *Review of Scientific Instruments* **88**, 073702 (2017).
81. Yurtsever, A., Fernández-Torre, D., González, C., Jelínek, P., Pou, P., Sugimoto, Y., Abe, M., Pérez, R. & Morita, S. Understanding image contrast formation in TiO<sub>2</sub> with force spectroscopy. *Physical Review B - Condensed Matter and Materials Physics* **85**, 1–9 (2012).
82. Bechstein, R., González, C., Schütte, J., Jelínek, P., Perez, R. & Kühnle, A. 'All-inclusive' imaging of the rutile TiO<sub>2</sub>(110) surface using NC-AFM. *Nanotechnology* **20**, 505703 (2009).
83. Giessibl, F. J. High-speed force sensor for force microscopy and profilometry utilizing a quartz tuning fork. *Applied Physics Letters* **73**, 3956–3958 (1998).
84. Giessibl, F. J. Atomic resolution on Si(111)-(7 × 7) by noncontact atomic force microscopy with a force sensor based on a quartz tuning fork. *Applied Physics Letters* **76**, 1470–1472 (2000).
85. Pielmeier, F., Meuer, D., Schmid, D., Strunk, C. & Giessibl, F. J. Impact of thermal frequency drift on highest precision force microscopy using quartz-based force sensors at low temperatures. *Beilstein Journal of Nanotechnology* **5**, 407–412 (2014).
86. Gross, L., Mohn, F., Liljeroth, P., Repp, J., Giessibl, F. J. & Meyer, G. Measuring the charge state of an adatom with noncontact atomic force microscopy. *Science (New York, N.Y.)* **324**, 1428–31 (2009).
87. Mayr-Schmölzer, W., Mittendorfer, F. & Redinger, J. All DFT calculations were performed by our collaborators at the Center for Computational Materials Science, TU Wien.

- 
88. Mayr-Schmölzer, W. *Adsorption of Small Molecules and Metal Adatoms on Complex Oxide Surfaces: a Density Functional Theory Study* PhD thesis (Technische Universität Wien, 2018).
  89. Halwidl, D., Stöger, B., Mayr-Schmölzer, W., Pavelec, J., Fobes, D., Peng, J., Mao, Z., Parkinson, G. S., Schmid, M., Mittendorfer, F., Redinger, J. & Diebold, U. Adsorption of water at the SrO surface of ruthenates. *Nature Materials* **15**, 450–455 (2015).
  90. Halwidl, D., Mayr-Schmölzer, W., Fobes, D., Peng, J., Mao, Z., Schmid, M., Mittendorfer, F., Redinger, J. & Diebold, U. Ordered hydroxyls on  $\text{Ca}_3\text{Ru}_2\text{O}_7(001)$ . *Nature Communications* **8**, 23 (2017).
  91. Halwidl, D., Mayr-Schmölzer, W., Setvin, M., Fobes, D., Peng, J., Mao, Z., Schmid, M., Mittendorfer, F., Redinger, J. & Diebold, U. A Full Monolayer of Superoxide: Oxygen Activation on the Unmodified  $\text{Ca}_3\text{Ru}_2\text{O}_7(001)$  Surface. *J. Mater. Chem. A* **6**, 5703–5713 (14 2018).
  92. Okada, Y., Walkup, D., Lin, H., Dhital, C., Chang, T. R., Khadka, S., Zhou, W., Jeng, H. T., Paranjape, M., Bansil, A., Wang, Z., Wilson, S. D. & Madhavan, V. Imaging the evolution of metallic states in a correlated iridate. *Nature Materials* **12**, 707–713 (2013).
  93. Loviat, F., Rønnow, H. M., Renner, C., Aeppli, G., Kimura, T. & Tokura, Y. The surface layer of cleaved bilayer manganites. *Nanotechnology* **18**, 044020 (2007).
  94. Thiel, P. A. & Madey, T. E. The interaction of water with solid surfaces: Fundamental aspects. *Surface Science Reports* **7**, 211–385 (1987).
  95. Henderson, M. The interaction of water with solid surfaces: fundamental aspects revisited. *Surface Science Reports* **46**, 1–308 (2002).
  96. Herman, G. S., Dohnalek, Z., Ruzycki, N. & Diebold, U. Experimental investigation of the interaction of water and methanol with anatase- $\text{TiO}_2(101)$ . *Journal of Physical Chemistry B* **107**, 2788–2795 (2003).
  97. Vittadini, A., Selloni, A., Rotzinger, F. P. & Grätzel, M. Structure and Energetics of Water Adsorbed at  $\text{TiO}_2$  Anatase (101) and (001) Surfaces. *Physical Review Letters* **81**, 2954–2957 (1998).

98. Daschbach, J. L., Dohnálek, Z., Liu, S.-r., Smith, R. S. & Kay, B. D. Water Adsorption, Desorption, and Clustering on FeO(111). *The Journal of Physical Chemistry B* **109**, 10362–10370 (2005).
99. Wendt, S., Matthiesen, J., Schaub, R., Vestergaard, E. K., Lægsgaard, E., Besenbacher, F. & Hammer, B. Formation and splitting of paired hydroxyl groups on reduced TiO<sub>2</sub>(110). *Physical Review Letters* **96**, 1–4 (2006).
100. Brookes, I. M., Murny, C. A. & Thornton, G. Imaging Water Dissociation on TiO<sub>2</sub>(110). *Physical Review Letters* **87**, 266103 (2001).
101. Lobo, A. & Conrad, H. Interaction of H<sub>2</sub>O with the RuO<sub>2</sub>(110) surface studied by HREELS and TDS. *Surface Science* **523**, 279–286 (2003).
102. Mu, R., Cantu, D. C., Lin, X., Glezakou, V. A., Wang, Z., Lyubinetsky, I., Rousseau, R. & Dohnálek, Z. Dimerization induced deprotonation of water on RuO<sub>2</sub>(110). *Journal of Physical Chemistry Letters* **5**, 3445–3450 (2014).
103. Parkinson, G. S. Iron oxide surfaces. *Surface Science Reports* **71**, 272–365 (2016).
104. Meyer, B., Marx, D., Dulub, O., Diebold, U., Kunat, M., Langenberg, D. & Wöll, C. Partial dissociation of water leads to stable superstructures on the surface of zinc oxide. *Angewandte Chemie (International ed. in English)* **43**, 6642–5 (2004).
105. Henderson, M. A., Joyce, S. A. & Rustad, J. R. Interaction of water with the (1×1) and (2×1) surfaces of  $\alpha$ -Fe<sub>2</sub>O<sub>3</sub>(012). *Surface Science* **417**, 66–81 (1998).
106. Wagner, M., Lackner, P., Seiler, S., Brunsch, A., Bliem, R., Gerhold, S., Wang, Z., Osiecki, J., Schulte, K., Boatner, L., Schmid, M., Meyer, B. & Diebold, U. Resolving the Structure of a Well-Ordered Hydroxyl Overlayer on In<sub>2</sub>O<sub>3</sub>(111): Nanomanipulation and Theory. *ACS Nano* **11**, 11531–11541 (2017).
107. Włodarczyk, R., Sierka, M., Kwapien, K., Sauer, J., Carrasco, E., Aumer, A., Gomes, J. F., Sterrer, M. & Freund, H.-J. Structures of the Ordered Water Monolayer on MgO(001). *The Journal of Physical Chemistry C* **115**, 6764–6774 (2011).
108. Dulub, O., Batzilln, M., Solovev, S., Loginova, E., Alchagirov, A., Madey, T. E. & Diebold, U. Electron-Induced Oxygen Desorption from the TiO<sub>2</sub>(011)-2×1 Surface Leads to Self-Organized Vacancies. *Science* **317**, 1052–1056 (2007).

- 
109. Setvin, M., Daniel, B., Aschauer, U., Hou, W., Li, Y.-F., Schmid, M., Selloni, A. & Diebold, U. Identification of adsorbed molecules via STM tip manipulation: CO, H<sub>2</sub>O, and O<sub>2</sub> on TiO<sub>2</sub> anatase (101). *Phys. Chem. Chem. Phys.* **16**, 21524–21530 (2014).
  110. Grönbeck, H. & Panas, I. *Ab initio* molecular dynamics calculations of H<sub>2</sub>O on BaO(001). *Physical Review B* **77**, 245419 (2008).
  111. Schmidt, P. C., Weiss, A. & Das, T. P. Effect of crystal fields and self-consistency on dipole and quadrupole polarizabilities of closed-shell ions. *Physical Review B* **19**, 5525–5534 (1979).
  112. Shannon, R. D. Revised effective ionic radii and systematic studies of interatomic distances in halides and chalcogenides. *Acta Crystallographica Section A* **32**, 751–767 (1976).
  113. Wrigley, J. D., Twigg, M. E. & Ehrlich, G. Lattice walks by long jumps. *The Journal of Chemical Physics* **93**, 2885 (1990).
  114. Singh, D. J. Relationship of Sr<sub>2</sub>RuO<sub>4</sub> to the superconducting layered cuprates. *Phys. Rev. B* **52**, 1358–1361 (1995).
  115. Iwahori, K., Watanabe, S., Kawai, M., Mizuno, K., Sasaki, K. & Yoshimoto, M. Nanoscale composition analysis of atomically flat SrTiO<sub>3</sub>(001) by friction force microscopy. *Journal of Applied Physics* **88**, 7099–7103 (2000).
  116. Stoerzinger, K. A., Hong, W. T., Crumlin, E. J., Bluhm, H., Biegalski, M. D. & Shao-Horn, Y. Water Reactivity on the LaCoO<sub>3</sub>(001) Surface: An Ambient Pressure X-ray Photoelectron Spectroscopy Study. *The Journal of Physical Chemistry C* **118**, 19733–19741 (2014).
  117. Stöger, B., Hieckel, M., Mittendorfer, F., Wang, Z., Fobes, D., Peng, J., Mao, Z., Schmid, M., Redinger, J. & Diebold, U. High Chemical Activity of a Perovskite Surface: Reaction of CO with Sr<sub>3</sub>Ru<sub>2</sub>O<sub>7</sub>. *Physical Review Letters* **113**, 116101 (2014).
  118. Schweitzer, C. & Schmidt, R. Physical mechanisms of generation and deactivation of singlet oxygen. *Chemical reviews* **103**, 1685–1757 (2003).
  119. Anpo, M., Che, M., Fubini, B. & Garrone, E. Generation of Superoxide Ions at Oxide Surfaces. *Topics in Catalysis* **8**, 189–198 (1999).

120. Setvin, M., Hulva, J., Parkinson, G. S., Schmid, M. & Diebold, U. Electron transfer between anatase TiO<sub>2</sub> and an O<sub>2</sub> molecule directly observed by atomic force microscopy. *Proceedings of the National Academy of Sciences* **114**, E2556–E2562 (2017).
121. Zhao, Y., Teng, B. T., Wen, X. D., Zhao, Y., Chen, Q. P., Zhao, L. H. & Luo, M. F. Superoxide and peroxide species on CeO<sub>2</sub>(111), and their oxidation roles. *Journal of Physical Chemistry C* **116**, 15986–15991 (2012).
122. Nolan, M. Healing of oxygen vacancies on reduced surfaces of gold-doped ceria. *The Journal of Chemical Physics* **130**, 144702 (2009).
123. Choi, Y. M., Abernathy, H., Chen, H. T., Lin, M. C. & Liu, M. Characterization of O<sub>2</sub>-CeO<sub>2</sub> interactions using in situ Raman spectroscopy and first-principle calculations. *ChemPhysChem* **7**, 1957–1963 (2006).
124. Pushkarev, V. V., Kovalchuk, V. I. & D'Itri, J. L. Probing Defect Sites on the CeO<sub>2</sub> Surface with Dioxygen. *The Journal of Physical Chemistry B* **108**, 5341–5348 (2004).
125. Xia, X., Oldman, R. J. & Catlow, C. R. A. Oxygen adsorption and dissociation on yttria stabilized zirconia surfaces. *Journal of Materials Chemistry* **22**, 8594 (2012).
126. Yan, Y., Al-Jassim, M. M. & Wei, S.-H. Oxygen-vacancy mediated adsorption and reactions of molecular oxygen on the ZnO(10 $\bar{1}$ 0) surface. *Physical Review B* **72**, 161307 (2005).
127. Ma, D., Wang, Z., Cui, H., Zeng, J., He, C. & Lu, Z. First-principles study of O<sub>2</sub> adsorption on Al-doped ZnO(10 $\bar{1}$ 0) surface. *Sensors and Actuators, B: Chemical* **224**, 372–380 (2016).
128. Gurlo, A. Interplay between O<sub>2</sub> and SnO<sub>2</sub>: Oxygen ionosorption and spectroscopic evidence for adsorbed oxygen. *ChemPhysChem* **7**, 2041–2052 (2006).
129. Frondelius, P., Häkkinen, H. & Honkala, K. Adsorption and activation of O<sub>2</sub> at Au chains on MgO/Mo thin films. *Physical chemistry chemical physics : PCCP* **12**, 1483–1492 (2010).

- 
130. Hellman, A., Klacar, S. & Grönbeck, H. Low Temperature CO Oxidation over Supported Ultrathin MgO Films. *Journal of the American Chemical Society* **131**, 16636–16637 (2009).
  131. Gonchar, A., Risse, T., Freund, H. J., Giordano, L., Valentin, C. D. & Pacchioni, G. Activation of oxygen on MgO: O<sub>2</sub>- radical ion formation on thin, metal-supported MgO(001) films. *Angewandte Chemie - International Edition* **50**, 2635–2638 (2011).
  132. Merkle, R. & Maier, J. How is oxygen incorporated into oxides? A comprehensive kinetic study of a simple solid-state reaction with SrTiO<sub>3</sub> as a model material. *Angewandte Chemie - International Edition* **47**, 3874–3894 (2008).
  133. Staykov, A., Téllez, H., Akbay, T., Druce, J., Ishihara, T. & Kilner, J. Oxygen Activation and Dissociation on Transition Metal Free Perovskite Surfaces. *Chemistry of Materials* **27**, 8273–8281 (2015).
  134. Akbay, T., Staykov, A., Druce, J., Téllez, H., Ishihara, T. & Kilner, J. A. The interaction of molecular oxygen on LaO terminated surfaces of La<sub>2</sub>NiO<sub>4</sub>. *J. Mater. Chem. A* **4**, 13113–13124 (2016).
  135. Sadewasser, S. & Glatzel, T. *Kelvin Probe Force Microscopy* <http://link.springer.com/10.1007/978-3-642-22566-6> (Springer Berlin Heidelberg, Berlin, Heidelberg, 2012).
  136. Gartland, P. O., Berge, S. & Slagsvold, B. J. Photoelectric work function of a copper single crystal for the (100), (110), (111), and (112) faces. *Physical Review Letters* **28**, 738–739 (1972).
  137. Puglia, C., Nilsson, A., Hernnäs, B., Karis, O., Bennich, P. & Mårtensson, N. Physisorbed, chemisorbed and dissociated O<sub>2</sub> on Pt(111) studied by different core level spectroscopy methods. *Surface Science* **342**, 119–133 (1995).
  138. Giordano, L., Cinquini, F. & Pacchioni, G. Tuning the surface metal work function by deposition of ultrathin oxide films: Density functional calculations. *Physical Review B - Condensed Matter and Materials Physics* **73**, 1–6 (2006).
  139. Lee, H. J. & Ho, W. Single-Bond Formation and Characterization with a Scanning Tunneling Microscope. *Science* **286**, 1719–1722 (1999).

140. Kim, Y., Motobayashi, K., Frederiksen, T., Ueba, H. & Kawai, M. Action spectroscopy for single-molecule reactions - Experiments and theory. *Progress in Surface Science* **90**, 85–143 (2015).
141. Alexander, C., Cao, G., Dobrosavljevic, V., McCall, S., Crow, J., Lochner, E. & Guertin, R. Destruction of the Mott insulating ground state of  $\text{Ca}_2\text{RuO}_4$  by a structural transition. *Physical Review B* **60**, R8422–R8425 (1999).
142. Wang, Z., Loon, A., Subramanian, A., Gerhold, S., McDermott, E., Enterkin, J. A., Hieckel, M., Russell, B. C., Green, R. J., Moewes, A., Guo, J., Blaha, P., Castell, M. R., Diebold, U. & Marks, L. D. Transition from reconstruction toward thin film on the (110) surface of strontium titanate. *Nano Letters* **16**, 2407–2412 (2016).
143. Druce, J., Téllez, H., Burriel, M., Sharp, M. D., Fawcett, L. J., Cook, S. N., McPhail, D. S., Ishihara, T., Brongersma, H. H. & Kilner, J. A. Surface termination and subsurface restructuring of perovskite-based solid oxide electrode materials. *Energy Environ. Sci.* **7**, 3593–3599 (2014).
144. Grasser, T. Stochastic charge trapping in oxides: From random telegraph noise to bias temperature instabilities. *Microelectronics Reliability* **52**, 39–70 (2012).
145. Grill, A. & Grasser, T. The software for analyzing the RTN signals was kindly provided by the Institute for Microelectronics, TU Wien.
146. Hasegawa, Y. & Avouris, P. Direct observation of standing wave formation at surface steps using scanning tunneling spectroscopy. *Physical Review Letters* **71**, 1071–1074 (1993).
147. Crommie, M. F., Lutz, C. P. & Eigler, D. M. Imaging standing waves in a two-dimensional electron gas. *Nature* **363**, 524 (1993).
148. Teichmann, K., Wenderoth, M., Loth, S., Ulbrich, R. G., Garleff, J. K., Wijnheijmer, A. P. & Koenraad, P. M. Controlled Charge Switching on a Single Donor with a Scanning Tunneling Microscope. *Physical Review Letters* **101**, 076103 (2008).
149. Marczinowski, F., Wiebe, J., Meier, F., Hashimoto, K. & Wiesendanger, R. Effect of charge manipulation on scanning tunneling spectra of single Mn acceptors in InAs. *Physical Review B - Condensed Matter and Materials Physics* **77**, 1–7 (2008).



- 
150. Cui, Y., Nilius, N., Freund, H.-J., Prada, S., Giordano, L. & Pacchioni, G. Controlling the charge state of single Mo dopants in a CaO film. *Physical Review B* **88**, 205421 (2013).
  151. Morgenstern, M., Haude, D., Gudmundsson, V., Wittneven, C., Dombrowski, R., Steinebach, C. & Wiesendanger, R. Low temperature scanning tunneling spectroscopy on InAs(110). *Journal of Electron Spectroscopy and Related Phenomena* **109**, 127–145 (2000).
  152. Haude, D., Morgenstern, M., Meinel, I. & Wiesendanger, R. Local density of states of a three-dimensional conductor in the extreme quantum limit. *Physical Review Letters* **86**, 1582–1585 (2001).
  153. Morgenstern, M., Georgi, A., Straßer, C., Ast, C. R., Becker, S. & Liebmann, M. Scanning tunneling microscopy of two-dimensional semiconductors: Spin properties and disorder. *Physica E: Low-Dimensional Systems and Nanostructures* **44**, 1795–1814 (2012).
  154. Kirton, M. J. & Uren, M. J. Noise in solid-state microstructures: A new perspective on individual defects, interface states and low-frequency ( $1/f$ ) noise. *Advances in Physics* **38**, 367–468 (1989).
  155. Najam, F., Tan, M. L. P., Ismail, R. & Seop Yu, Y. Two-dimensional (2D) transition metal dichalcogenide semiconductor field-effect transistors: The interface trap density extraction and compact model. *Semiconductor Science and Technology* **30**, 75010 (2015).
  156. Dudarev, S. L., Botton, G. A., Savrasov, S. Y., Humphreys, C. J. & Sutton, A. P. Electron-energy-loss spectra and the structural stability of nickel oxide: An LSDA+U study. *Physical Review B* **57**, 1505–1509 (1998).



# Daniel Halwidl

✉ [danielhalwidl@aim.com](mailto:danielhalwidl@aim.com)

---

## Personal Information

Date of Birth 16.06.1987

Citizenship Austria

---

## Education

2014 - 2018 **Doctoral Programme in Technical Sciences.**

Institute of Applied Physics, TU Wien, Austria

### PhD Thesis

*Surface Science Investigations on Single-Crystalline Ruthenates*

Supervisor: Univ.Prof. Dipl.-Ing. Dr.techn. Ulrike Diebold

2011 - 2014 **Master Programme Technical Physics.**

Institute of Applied Physics, TU Wien, Austria

### Master Thesis

*Development of an Effusive Molecular Beam Apparatus*

Supervisor: Univ.Prof. Dipl.-Ing. Dr.techn. Ulrike Diebold

2007 - 2011 **Bachelor Programme Technical Physics.**

TU Wien, Austria

2001 - 2006 **HTL für Elektronik.**

Secondary School

TGM Wien, Austria

---

## Publications

### As first author

*A full monolayer of superoxide: oxygen activation on the unmodified  $\text{Ca}_3\text{Ru}_2\text{O}_7(001)$  surface*, Journal of Materials Chemistry A **6**, 5703–5713 (2018)

*Ordered hydroxyls on  $\text{Ca}_3\text{Ru}_2\text{O}_7(001)$* ,  
Nature Communications **8**, 23 (2017)

*Adsorption of water at the SrO surface of ruthenates*,  
Nature Materials **15**, 450–455 (2016)

*Development of an effusive molecular beam apparatus*,  
Springer Fachmedien Wiesbaden, ISBN: 978-3-658-13535-5 (2016)

### As co-author

J. Pavelec *et al.*, *A multi-technique study of  $\text{CO}_2$  adsorption on  $\text{Fe}_3\text{O}_4$  magnetite*,  
Journal of Chemical Physics **146**, 14701 (2017)

Vienna, June 2018